2016

Development of single microdroplet techniques for fundamental chemical measurements

Bartholomew S. Vaughn
University of Wollongong

Development of single microdroplet techniques for fundamental chemical measurements

Bartholomew S. Vaughn

Supervisor:
Assoc. Prof. Adam J. Trevitt

This thesis is presented as required for the conferral of the degree:

Doctor of Philosophy

The University of Wollongong
School of Chemistry

November 15, 2016

Declaration

I, Bartholomew S. Vaughn, declare that this thesis submitted in fulfilment of the requirements for the conferral of the degree Doctor of Philosophy, from the University of Wollongong, is wholly my own work unless otherwise referenced or acknowledged. This document has not been submitted for qualifications at any other academic institution.

Bartholomew S. Vaughn
November 15, 2016

Abstract

A significant number of current techniques that probe chemical and physical processes in single microdroplets focus on the measurement of long timescale processes. Probing short timescale processes (<100 μs) in single microdroplet domains has been largely prohibitive. Therefore, new experimental techniques are required to probe short timescale chemical transformations in microdroplets. In this thesis, experiments on single free-falling microdroplets that probe chemistry and physics of photoactivated reactions are reported. Single microdroplets are generated using drop-on-demand droplet generation and subsequently interrogated using various pulsed laser systems. The principal advantage of single microdroplet techniques is that each microdroplet is a chemically isolated and self-contained reaction vessel. This allows chemical and physical transformations to be probed with no cross-contamination between microdroplets.

Microdroplet generators are characterised by determining droplet size using cavity-enhanced fluorescence spectroscopy from single aqueous microdroplets, doped with a fluorescent dye. The size of individual microdroplets is determined with nanometer precision using Mie theory. Driven by a square-wave potential, droplet size is measured for thousands of consecutive microdroplets to determine the droplet size reproducibility. Using this standard waveform, droplet size variation is less than 1%. The effect of more complex waveforms on microdroplet size is investigated, finding that microdroplets with radii spanning 10 to 30 μm (1 to 110 pL) are produced from the same droplet generator (with an internal diameter of 50 μm). Droplet size stability for each complex waveforms is highly reproducible with <1% size variation. Effects of systematic changes to the standard square-wave driving waveform is investigated and predictable size changes, with steps on the order of tens of nanometers, are realised. Finer adjustments to the driving waveform (on the nanosecond timescale) allow the microdroplet size to be tuned by nanometers. The results confirm the extremely high stability and reproducibility of the on-demand microdroplet generator and that it is suitable platform for single microdroplet chemical measurements.

Photoinitiated iodine radical recombination is investigated in single free-falling microdroplets of iodododecane using a precisely timed two pulsed-laser experiment

coupled with cavity-enhanced Raman spectroscopy. Stimulated Raman spectra, pumped with 532 nm pulsed laser, are collected from single microdroplets as a UV pulsed laser (λ = 266 nm) irradiates each microdroplet at controlled time delays. Photolysis of the C–I bond of 1-iodododecane generates I radicals within the microdroplet that rapidly recombine to form molecular iodine (I_2), which efficiently absorbs visible photon wavelengths. Varying the time delay between the photolysis and Raman probe laser allows the quenching process to be followed over ∼10 ns, which is approximately the time resolution of the two-laser experiment. When the photolysis laser energy is reduced, incomplete quenching of the Raman signal is observed on the same timescale confirming that the recombination kinetics are too rapid to be measured using nanosecond lasers.

Chemical transformations of photoinitiated radical hydroxylation are investigated in single free-falling aqueous microdroplets containing the profluorescent hydroxyl radical scavenger terephthalate (TA) and a hydroxyl radical precursor, H_2O_2. A two-laser setup is used to monitor the fluorescence growth from the reaction product, hydroxyterephthalate (TAOH). A UV pulsed laser (λ = 266 nm) irradiates the free-falling microdroplets at controlled delay times, while the 310 nm emission from a pulsed dye laser is used to probe the fluorescent product. Exponential growth curves are measured over a range of TA concentrations. Extracted pseudo-first order rate constants appear to follow a linear trend at low concentrations, but exhibit a roll-over at higher concentrations. This suggests a process is inhibiting the formation of TAOH at high TA concentrations. Single droplet desorption mass spectrometry is used to further probe the radical chemistry within the microdroplet and found that the resulting chemistry is highly complex. Despite the exact process leading to the formation of TAOH remaining unknown, this study presents the first use of a profluorescent strategy to probe radical chemistry in single microdroplets.

A known photoinitiated single electron transfer reaction is observed in single free-falling microdroplets using the single droplet desorption mass spectrometry technique. Droplets are generated from a methanol solution containing berberine, a native cation and iminium salt, which is known to undergo a single electron transfer (SET) with electron donating solvents, in this case methanol, when photoexcited. Free-falling microdroplets are irradiated with a UV pulsed laser (λ = 266 and 355 nm) prior to desorption. The desorbed microdroplet is sampled by the mass spectrometers inlet and a full mass spectrum is collected. The initial SET photoproduct, addition of the methanol solvent, is observed as the major photoproduct. Additional photoproducts resulting from further radical chemistry are also observed. Three successions of solvent addition is measured when irradiated with 355 nm, while 266 nm irradiated produces up to five orders due to an additional photoionisation process available to the higher energy photon. Wavelength dependence of the photoproduct

yield is investigated showing the onset of the photoionisation process at ∼300 nm. This study demonstrates the unique insights into liquid-phase photochemistry available to single droplet desorption mass spectrometry that is are not achievable using bulk or gas-phase photolysis measurements.

Acknowledgments

Firstly, I would like to acknowledge my supervisor Associate Professor Adam Trevitt. His assistance and guidance throughout my PhD candidature was a crucial in the completion of this doctoral work. His attention to detail and drive for accurate scientific results have shaped my own work ethic and I will always be thankful for that.

Secondly, I would like to acknowledge Phil Tracey for all the friendship, support and assistance throughout my candidature. He always made any time spent working in the lab enjoyable and his work ethic and determination for success inspired me.

I would like to acknowledge Christopher Hansen for his friendship, advice and assistance working in the lab. His knowledge and skills, both scientific and general, were key to overcoming any difficult problems. Whether it was a sneaky six-pack, a coffee break or hanging out throwing the football his presence always made for a great day of science and made my PhD candidature highly enjoyable.

I would like to acknowledge the past and present members of the Laser Chemistry Laboratory. Their helpful insights at group meetings, in the lab and in the office were extremely useful. I would like to thank James Bezzina for his friendship and limitless entertainment over the years. I would like to thank Dr Berwyck Poad for his technical expertise and scientific advice. I would to thank Matthew Prendergast for his assistance in reading thesis chapters and unusual but entertaining office banter.

My family for not asking too many questions about what I do and providing unlimited support throughout my candidature. Their constant support at home was especially crucial when finalising this thesis.

Finally, I would like to thank my partner Hayley Moffat for her unwavering support. Her constant motivation throughout my candidature was indispensable. Her excellent proof-reading skills were extremely helpful. She has kept me motivated and focused when it was required most. Most importantly, she always made me smile on a bad day.

Publications

The work presented in Chapter 2 of this thesis resulted in the following publication:
Drop-on-Demand microdroplet generation: a very stable platform for single-droplet experimentation
B. S. Vaughn, P. J. Tracey and A. J. Trevitt, *RSC Advances*, **6**, 60215-60222 (2016).

The work presented in Chapter 3 of this thesis resulted in the following publication:
Laser-initiated iodine radical chemistry in single microdroplets
B. S. Vaughn, P. J. Tracey and A. J. Trevitt, *Chemical Physics Letters*, **551**, 134-138 (2012).

The single microdroplet mass spectrometry studies, presented in Chapter 5, as well as other experimental work in this thesis contributed directly to the following publication:
Rapid Profiling of Laser-Induced Photochemistry in Single Microdroplets Using Mass Spectrometry
P. J. Tracey, B. S. Vaughn, B. J. Roberts, B. L. J. Poad, and A. J. Trevitt, *Analytical Chemistry*, **86**, 2895-2899 (2014)

Contents

Figures

Abbreviations

SRS ..... Stimulated Raman scattering
VOAG ..... Vibrating orifice aerosol generator
LILBID ..... Laser-induced liquid bead ion desorption
IR ..... Infrared
FIDI ..... Field-induced droplet ionization
DoD ..... Drop-on-demand
UV ..... Ultraviolet
LED ..... Light emitting diode
MDR ..... Morphology dependent resonances
WGM ..... Whispering gallery mode
TE ..... Transverse electric
TM ..... Transverse magnetic
FWHM ..... Full-width half-maximum
TA ..... Terephthalate anion
SDDMS ..... Single droplet desorption mass spectrometry
ESI ..... Electrospray ionisation
PD ..... Photodissociation
CID ..... Collision induced dissociation

Chapter 1

Introduction

1.1 Single microdroplet experiments

Single particle chemical experiments have been reported since the early 1900's with increasing interest in recent times. Many of the studies in this field are currently focused on studying fundamental aerosol processes in a controlled environment [1–3]. By studying single particles in isolation the complexities introduced when studying aerosol ensembles are eliminated. Using such techniques the fundamentals of single particle processes can be studied and can be used to validate current and new atmospheric aerosol models [1, 3]. While these techniques are often driven by atmospheric systems, the techniques also have impacts in many other fields and industries such as drug delivery [4] and combustion [2].

Recent developments in single microparticle techniques tend to predominantly utilise acoustic, electrodynamic and optical levitation [1, 3]. These techniques allow chemical and physical processes to be followed over long timescales (seconds to hours) by deploying optical spectroscopy techniques such as laser induced fluorescence [1], elastic light scattering [5] and Raman scattering [3, 6]. The focus of these studies is the fundamental dynamics of single aerosol particles, including mass transfer and accommodation [7], mechanisms and kinetics of oxidation processes [8] and evaporation and growth rates [9, 10]. Using these isolation techniques, single particles can be monitored on the timescale of seconds to hours and, theoretically, indefinitely. While the use of isolation techniques allows a single particle to be probed for long time-scale measurements, short time scale measurements ($<$100 μs) can be difficult and time consuming, as each measurement requires a single "fresh" particle to be reloaded into the trap [1]. Investigation of short time-scale ($<$100 μs) chemical and physical processes, such as radical chemical kinetics and photoinitiated chemistry, require the development of new techniques.

Free-falling droplet experimental strategies have shown to be effective for

probing aerosol processes and properties such as evaporation rates [11–13], mixing rates [14, 15] and chemical composition [16, 17]. Additionally, single free-falling droplets have been utilised as vessels to introduce chemical species into mass spectrometers for analysis [18–21]. These studies have shown that short time-scale measurements are possible in single droplets (35 - 50 μm radius), but have also highlighted the requirement for high reproducibility of the droplet size [14, 22]. When this requirement is met, the advantages of free-falling microdroplets (constantly refreshed reaction vessels and high throughput) make for a desirable platform to perform short time-scale chemical kinetics (0.1 – 100 μs) and photochemical measurements [23]. The goal of this work is to address this need and develop new techniques that utilise stable streams of free-falling single microdroplets to probe chemical kinetics and photochemistry.

1.1.1 Key events in the history of single microdroplet experiments

A crucial event in the history of single microdroplet experiments was the development of solutions to Maxwell's equation for electromagnetic radiation interacting with a spherical particle, which was originally published by Ludvig Lorenz in 1890 [24], and later independently published by Gustav Mie in 1908 [25]. These solutions are known as Mie theory, which describe the scattering properties of electromagnetic radiation when interacting with a spherical particle. Mie theory is commonly utilised to interpret the absorption, scattering and extinction of particles – both ensembles and single particles. A brief summary of the background Mie theory used in this thesis is presented in Appendix A.

A seminal single droplet experiment is the Millikan oil droplet experiment designed to determine the value of the elementary charge (e) from a cloud of oil microdroplets. When stabilising a cloud of microdroplets it was found that single microdroplets could be isolated [27]. The experimental apparatus, known as a Millikan condenser is shown schematically in Figure 1.1. The apparatus pumps dry air into an atomiser (labeled A) filled with an oil producing an aerosol of oil droplets, which are dispersed in the condenser (labeled C). During the atomisation process, the droplets gain electric charge from friction. Once in the condenser, droplets can fall through an open pinhole at the bottom of the condenser which is closed after a single droplet has passed through. After the pinhole, two charged plates (labeled M and N) generate an electric field that interacts with the droplet. Using a switch, a positive potential is applied to the top plate to attract the oil droplet, if it holds a negative charge. By measuring the velocity of droplet as it moved towards the plate, the magnitude of the electrical charge was determined [26]. This style of instrument

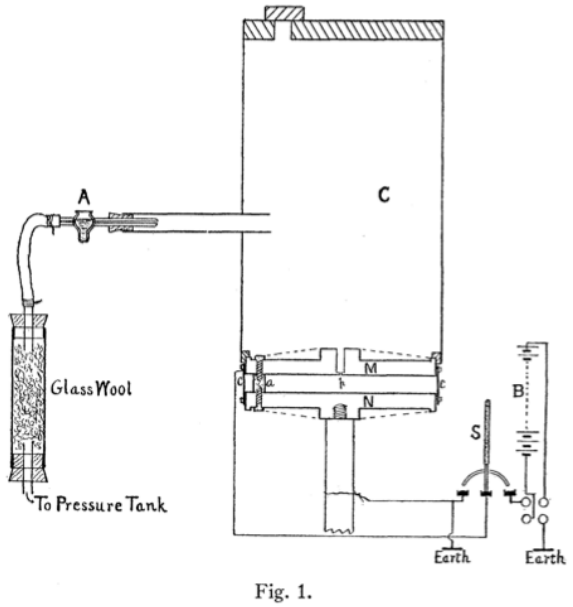

Figure 1.1: Schematic of a Millikan condenser. Reprinted figure with permission from R. A. Millikan, Physics Reviews (Series I), **32**, 349397, 1911. [26] Copyright (2016) by the American Physical Society.

was used subsequently to isolate single microdroplets [28, 29].

In 1960, Gucker and Rowell measured the angular dependence of light scattered from single liquid microdroplets of octyl phthalate [28] using a setup similar to the Millikan condenser with the addition of a monochromatic light source and photometer [29]. This study set out to validate Mie theory predictions of the angular scattering intensity from spherical microdroplets. Charged liquid microdroplets were nebulised into the modified Millikan condenser and isolated in the same manner. Measuring the rate at which the microdroplet moved between the charged plates allowed the calculation of the microdroplet radius [29]. The angular dependent scattering from microdroplets ranging from 0.75 to 1.5 μm radius was measured and was found to match Mie theory predictions [28, 29], an example of these measurements in shown in Figure 1.2.

Another seminal development in single droplet studies was the first report of optical levitation of a single microdroplet by Ashkin *et al.* in 1971. Initially in 1970, Ashkin published a letter proposing the use of a continuous wave argon laser to optically trap particles dispersed in water, which was further extended to nebulised water droplets suspended in gas [30]. As the nebulised water droplets were irradiated there was an observable acceleration in the droplets movement, due to the radiation pressure of the photons interacting with the droplets. This technique was expanded by Ashkin *et al.* in 1971 to successfully levitate 20 μm glass spheres [31]. These experiments were the genesis of optical tweezer techniques, which is now widely used in condensed phase studies of atmospheric and biological processes [1–3, 32].

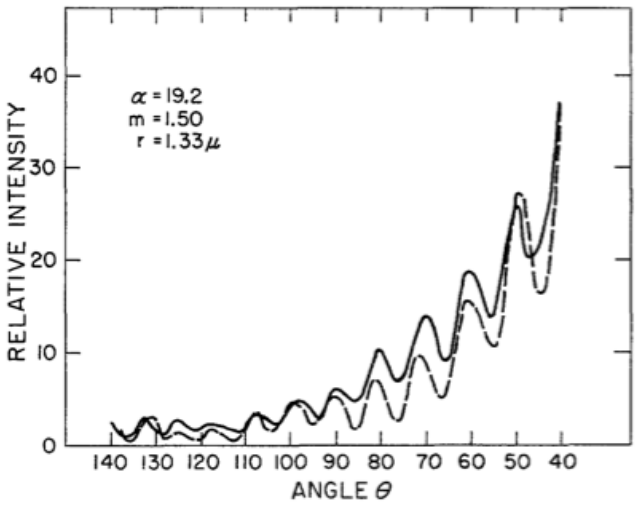

Figure 1.2: The measured angular dependent elastic light scattering from a single dioctyl phthalate droplet (radius = 1.33 μm) irradiated with unpolarised light. The solid line represents the experimental data, while the dashed line shows the Mie theory data. Reprinted from Journal of Colloid Science, **16**, F.T. Gucker and J.J Egan, Measurement of the angular variation of light scattered from single aerosol droplets, 68-84. [29], Copyright (2016), with permission from Elsevier.

In 1977, Ashkin and Dziedzic reported the first experimental observation of sharp optical resonances using an optical levitation arrangement with a tunable continuous dye-laser [33]. While levitating single water microdroplets, the laser power was dynamically controlled using optical feedbacks in order to maintain the levitated droplet at a fixed height. As the dye laser's output wavelength was scanned, it was found that at specific wavelengths there were sharp decreases in the required laser power to maintain the droplet at the set height. This was due to the laser tuning onto wavelengths that matched optical resonances of the droplet, resulting in an increase in radiation pressure imparted on the the droplet. These wavelengths that form optical resonances, manifest as peaks in Figure 1.3 (top), were found to be in good agreement with a Mie theory simulation (bottom). The minor discrepancies between the two spectra shown in Figure 1.3 arise from the Mie theory simulation calculated with a refractive index of 1.33, where the experimentally measured refractive index of the microdroplet was 1.40 [33].

The first report of sharp resonances within optical emission from a single particle was by Benner *et al.* (1980) where the measured fluorescence emission spectrum acquired from a single dye-doped polystyrene microsphere, dispersed in water, was found to contain resonances (see Appendix A) [34]. The apparatus used in this measurement, shown in Figure 1.4, consisted of a cell containing a dilute solution of microspheres irradiated by an argon laser operating at 457.9 nm. Perpendicular to the laser input, the fluorescence emission was measured. As Figure 1.5 shows, the spectra each contain sharp peaks throughout the fluorescence band owing to

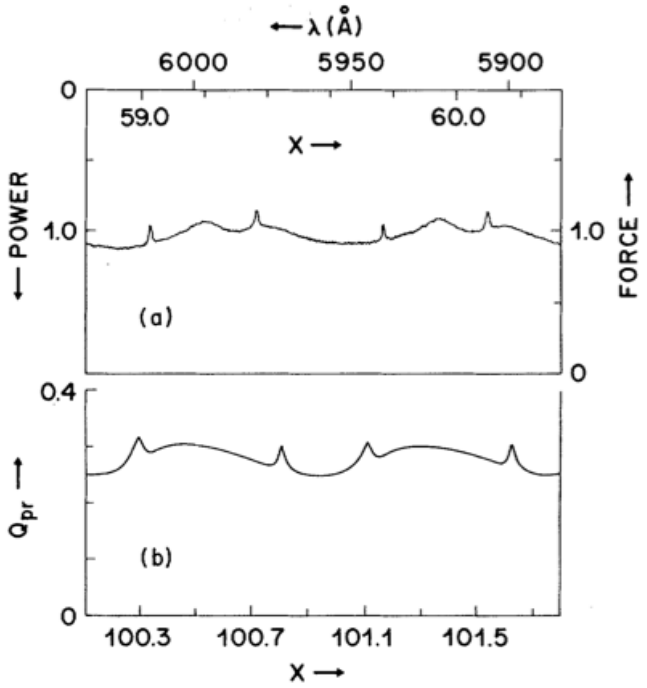

Figure 1.3: Measured laser power required to levitate a silicone oil microdroplet (11.3 μm diameter, 1.40 refractive index) at a fixed height and its dependence on laser wavelength (Top). Mie theory calculated for a particle of the same size with a fixed refractive index of 1.33. The peaks are optical resonances of the microdroplet, when the laser wavelength is resonant, a decrease in required laser power is observed. Reprinted figure with permission from A. Ashkin and J. M. Dziedzic, Physical Review Letters, **38**, 1351, 1977. [33] Copyright (2016) by the American Physical Society.

the presence of optical resonances within the cavity of the microsphere. The shifts in optical resonance locations between each spectrum are due to minor differences in microsphere size, as each spectrum is from an individual particle. This study showed that minor changes in particle size, on the scale of tens of nanometers, would measurably impact on the location of the optical resonances and was an important revelation, as these resonances had only been observed previously by external measurements, while the source of the fluorescence emission was internal to the dye-doped microspheres [34].

Simpson *et al.* published the first measurement of Raman scattering from single microdroplets in 1983 while developing a technique to measure reaction kinetics in coalescing microdroplets [14]. In this study two streams of microdroplets with different chemical compositions were aligned to collide at a shallow angle where, upon collision, each pair of droplets would coalesce forming a single microdroplet that was subsequently probed by Raman scattering with illumination from an argon laser. One stream of droplets was generated from a dilute Fe(II) solution, while the other was generated from a dilute solution containing the organic ligand

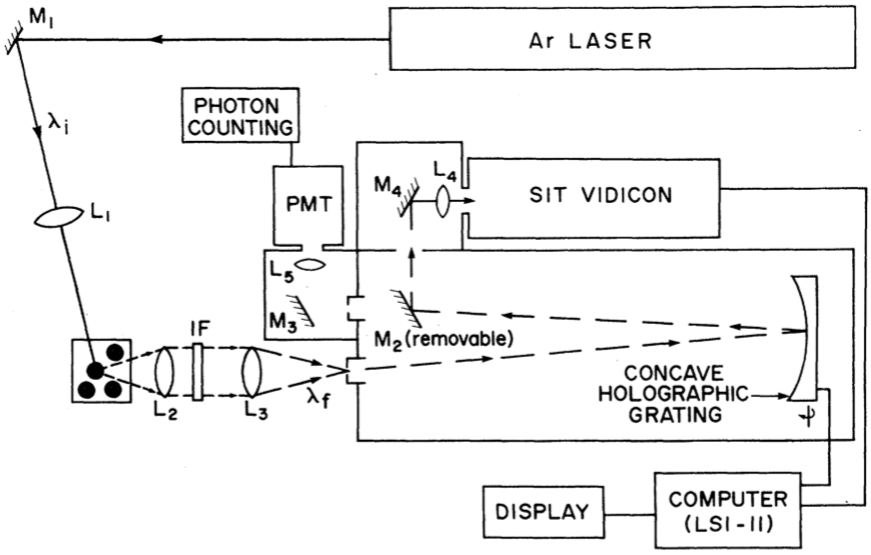

Figure 1.4: Schematic describing the setup used to measure the cavity-enhanced fluorescence emission from single microparticles in liquid. Reprinted figure with permission from R.E. Benner *et al.*, Physical Review Letters, **44**, 475, 1980. [34] Copyright (2016) by the American Physical Society

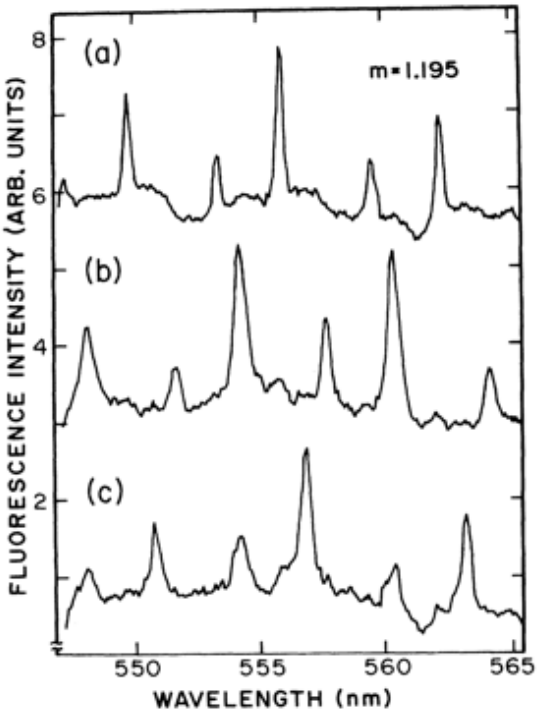

Figure 1.5: Fluorescence emission spectra from single dye-doped polystyrene microspheres (9.90 μm diameter) in water. The observed peaks arise from resonances within the microspheres cavities. Reprinted figure with permission from R.E. Benner *et al.*, Physical Review Letters, **44**, 475, 1980. [34] Copyright (2016) by the American Physical Society.

phenanthroline (phen). Once the pair of droplets combined, the ligand becomes bound to the Fe(II) to form $[Fe(phen)_3]^{2+}$.

In order to determine whether a Raman emission from $[Fe(phen)_3]^{2+}$ could be measured in single microdroplets, the experiment was performed using a single stream of microdroplets made from a stock solution of $[Fe(phen)_3]^{2+}$. The resulting Raman emission is shown in Figure 1.6 (A). Once it was determined that the Raman emission could be detected, the experiment with two droplet streams was performed with the resulting Raman spectrum collected from the coalesced microdroplet shown in Figure 1.6 (B).

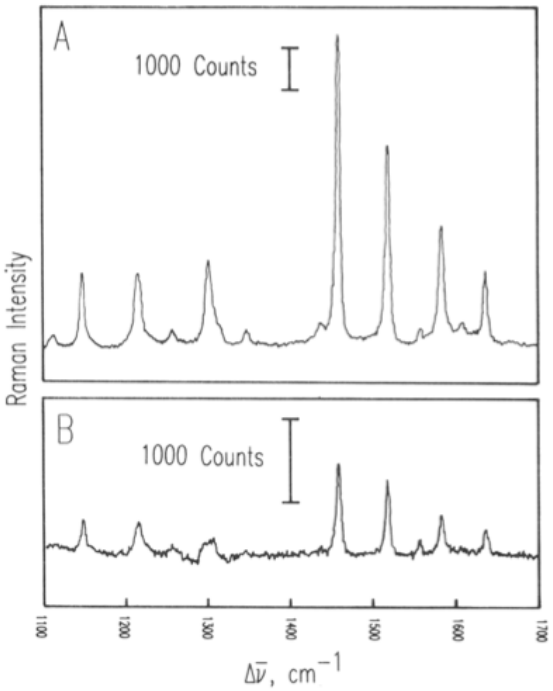

Figure 1.6: (A) Raman spectra from a single 100 μm water microdroplet containing $[Fe(phen)_3]^{2+}$. (B) Raman spectrum collected from a single microdroplet after coalescence. Reprinted figure with permission from S. F. Simpson, J. R. Kincaid and F. J. Holler, "Microdroplet mixing for rapid reaction-kinetics with Raman spectrometric detection", Analytical Chemistry, **55**, 14201422, 1983. [14] Copyright (2016) American Chemical Society.

This microdroplet mixing experiment was extended to time dependent studies on the reactions occurring after coalescence and was published by Simpson *et al.* (1986) [15]. The study showed that by fixing the argon laser position and translating the droplet generators along the axis of the coalesced droplet stream, as shown in Figure 1.7, the resulting microdroplets could be probed at varying times after coalescence. By monitoring the intensity of the Raman signal against the position of the droplet generator, the formation rate for the $[Fe(phen)_3]^{2+}$ was measured. It was found that 99% of the solution was mixed by 560 μs after coalescence, which was 2-5 times faster than measured mixing rate for the same reaction in stopped-flow techniques

[15]. This result demonstrated that kinetic measurements from single microdroplets are possible, but it was noted that the instabilities of the coalesced droplets shape, resulting in lower quality Raman spectra, limited the accuracy of the measurement [14, 15].

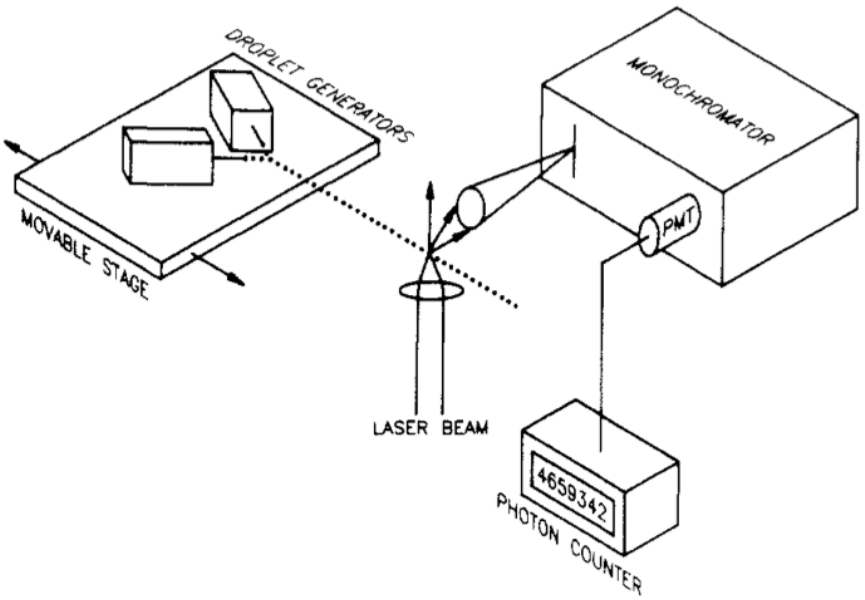

Figure 1.7: Schematic of the apparatus used by Simpson *et al.* to measure chemical kinetics by intersecting two streams of microdroplets. Reprinted figure with permission from S. F. Simpson, J. R. Kincaid and F. J. Holler, "Development of a micro droplet mixing technique for the study of rapid reactions by Raman spectroscopy", Analytical Chemistry, **58**, 31633166, 1986. [15] Copyright (2016) American Chemical Society.

A study published by Snow *et al.* (1985) investigated stimulated Raman scattering (SRS) from single free-falling microdroplets of water and ethanol, which was the first reported cavity-enhanced Raman scattering experiment utilising single free-falling microdroplets [35]. Previous studies reported Raman emission from glass microspheres [36] and microcapillaries [37] bearing optical resonances. Additionally, these studies reported that Raman emission, along with fluorescence emission, from single dye-doped microdroplets exhibited lasing and that the onset thresholds for lasing were much lower than those of optical cells [38].

The goal of the study by Snow *et al.* was to reveal if SRS in single microdroplets was observable and whether it too exhibited the decreased power thresholds required for lasing. Microdroplets were generated using a vibrating orifice aerosol generator (VOAG), an instrument that exploits a piezoelectric actuator operating at high frequencies to break a liquid beam into a stream of monodisperse microdroplets. The free-falling microdroplets of water and ethanol were probed using a pulsed Nd:YAG laser ($\lambda = 532$ nm) with the Raman emission collected by a spectrograph. The measured Raman emission from the water microdroplets contained a number

of sharp optical resonances over the range of the Raman band, as shown in Figure 1.8.

To determine whether these resonances were due to optical resonances within the droplets the operating frequency of the VOAG was tuned to produce droplets of different sizes, which were subsequently probed [35]. When the frequency of the VOAG decreased, the spacing between the optical resonances also decreased (Figure 1.9), as the size of the resulting droplet had increased due to longer intervals between breaks in the liquid beam. This result supported the notion that the SRS emission was due to optical resonances, as they are highly dependent on the size of the microdroplet.

1.1.2 Recent single microdroplet studies

This thesis is focused on the development of free-falling single microdroplet techniques. The most recent studies reported in the field are predominantly focused on incorporating single microdroplets into various analytical techniques, such as a transport vehicle for introduction into mass spectrometers [18, 20, 21, 39–41] and chemical identification using cavity-enhanced Raman spectroscopy [16, 17].

In 1996 Kleinekofort *et al.* reported a new technique, laser induced liquid beam ion desorption (LILBID), to introduce charged chemical species into the gas phase for analysis using mass spectrometry [20]. This technique uses a pulsed IR laser to desorb the charged chemical species within the liquid beam in a vacuum environment. The goal of this technique was to introduce biological molecules from solution into the gas phase in a "soft" manner (minimal fragmentation), this allowed weak non-covalent interactions to be preserved and investigated using mass spectrometry.

A liquid beam is established by applying pressure to a reservoir, containing the solvent, that passes through a sample loop before ultimately exiting a 10 μm nozzle to form the beam [21]. The liquid beam's laminar flow reduces the load required to maintain the vacuum environment. Samples are introduced into a solvent, either water or alcohol, using a sample loop prior to forming the liquid beam. The frequency of the IR laser is tuned to match the absorption band of the solvent. When the solvent is water the IR laser wavelength is typically between 2.5–3.5 μm to match the two O–H stretching bands, while alcoholic solvents are irradiated with 9.5–10.5 μm matching the C–O stretching band. The desorption process occurs when the liquid beam is irradiated by the IR laser. The liquid beam is directed at a liquid nitrogen cooled trap, shown in Figure 1.10 to freeze out the liquid to maintain the low pressure environment. Charged species liberated from the liquid beam are extracted perpendicular to the laser pulse, as shown in Figure

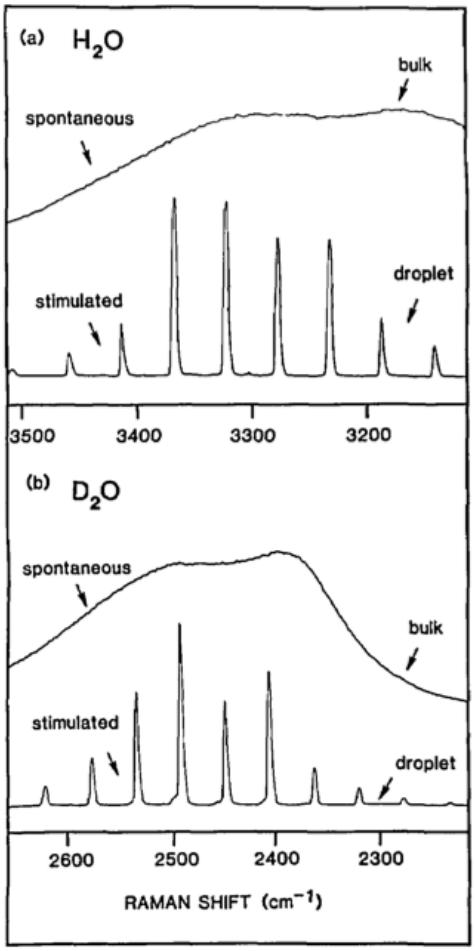

Figure 1.8: Raman spectra collected from both bulk-phase solutions and single microdroplets of water (a) and deuterated water (b). Figure reproduced with permission from J. Snow, S.-X. Qian and R. Chang, Stimulated Raman scattering from individual water and ethanol droplets at morphology-dependent resonances, Optics Letters, 1985, 10, 3739. [35].

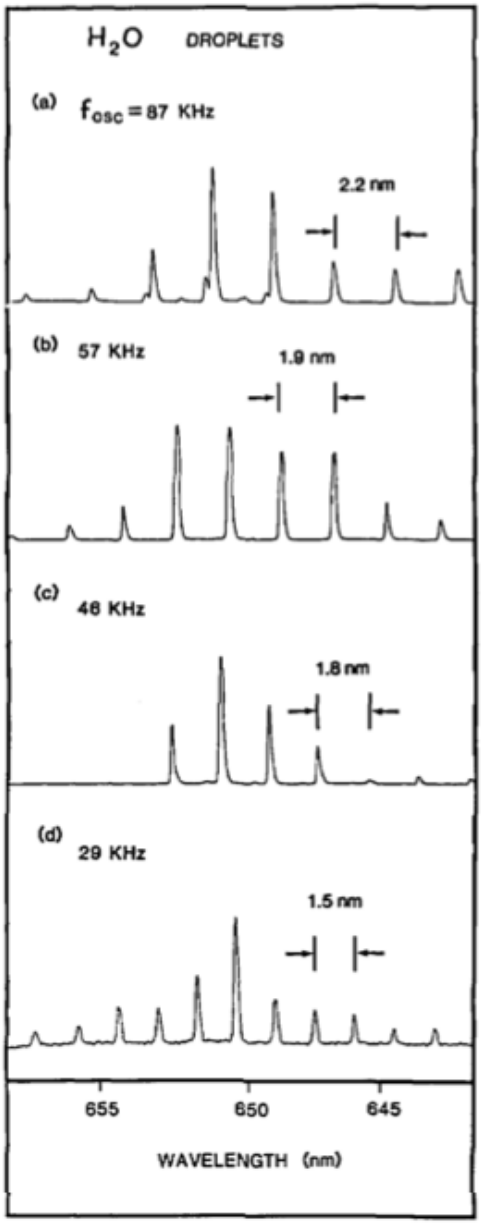

Figure 1.9: Cavity-enhanced Raman spectra collected from single microdroplets of water generated using different frequencies. As the frequency is reduced, going from (a) to (d) the spacing between the optical resonances decreases resulting from an increase in microdroplet size. Figure reproduced with permission from J. Snow, S.-X. Qian and R. Chang, Stimulated Raman scattering from individual water and ethanol droplets at morphology-dependent resonances, Optics Letters, 1985, 10, 3739. [35].

1.10, and ultimately sampled by time-of-flight mass spectrometry [21].

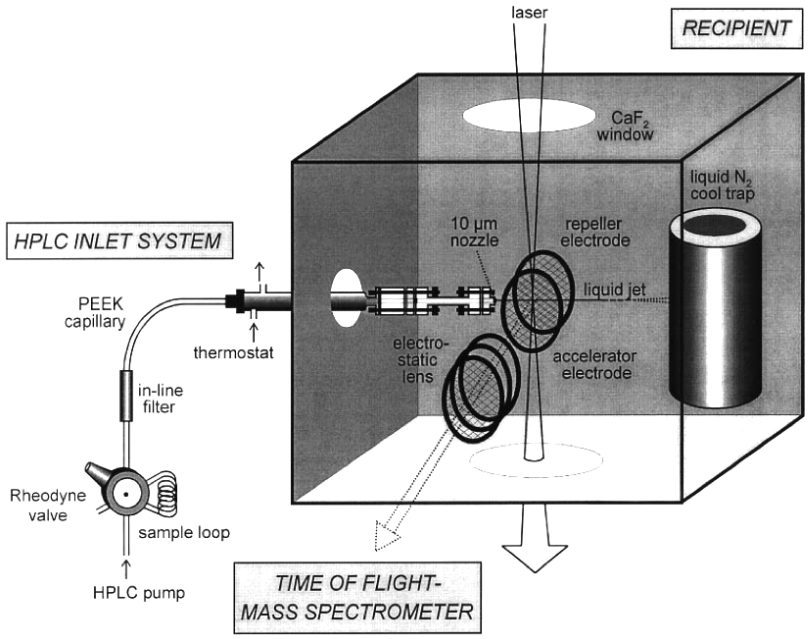

Figure 1.10: Schematic diagram of the LILBID experiment. The liquid beam is pulsed with an IR laser beam, tuned to match the absorption profile of the solvent, causing charged species to be desorbed that are collected and sampled by the time-of-flight mass spectrometer. Figure reproduced from Fresenius' Journal of Analytical Chemistry, "Laser desorption mass spectrometry on thin liquid jets", **360**, 1998, 745749, F. Sobott *et al.* [21], with permission of Springer.

This technique proved to be a "soft" desorption method being capable of transporting non-covalently bound species from liquid into the mass spectrometer. Although, it was found that running a continuous liquid beam, while the laser was limited to a frequency of 10 Hz, was inefficient for sample consumption and subjected the chamber to an unnecessary load [39]. To overcome this, the technique was improved by replacing the liquid beam with a drop-on-demand (DoD) droplet generator allowing single microdroplets to be introduced for each IR laser pulse. This greatly reduced the sample volume requirements, while still providing the soft desorption capabilities and chemical sensitivity [39, 42–44]. As this improvement removed the liquid beam, the technique was renamed laser induced liquid *bead* ion desorption.

Another notable single droplet mass spectrometry technique is field-induced droplet ionisation (FIDI) reported by Grimm *et al.* (2003). FIDI utilises the electrical breakdown of single microdroplets as a source to introduce chemical species into a mass spectrometer [40]. The droplets are generated using a VOAG with the resulting droplet stream passing between two plates, as shown in Figure 1.11, one plate is raised to a high voltage (±4 kV) while the other is held to ground. The electric field between the two plates causes the droplet, containing charged analytes,

to distort and breakdown along the field between the two plates (Figure 1.11) [40, 41]. Smaller charged droplets are generated from this breakdown and pass through a hole in the grounded plate to the mass spectrometer inlet. This method was found to be a soft ionisation technique that can be used to introduce complex biological molecules into the gas phase for analysis using mass spectrometry [40]. Additionally, this ionisation technique could be performed at ambient pressures. This technique can potentially detect both the positively and negatively charged species from a single microdroplet, as each species are attracted to the opposite plates. Since this publication, Grimm and workers have characterised the technique, looking into the fundamentals of the breakdown and have used FIDI to look at time-dependent ozone reactions on the droplet's surface [18, 19, 41].

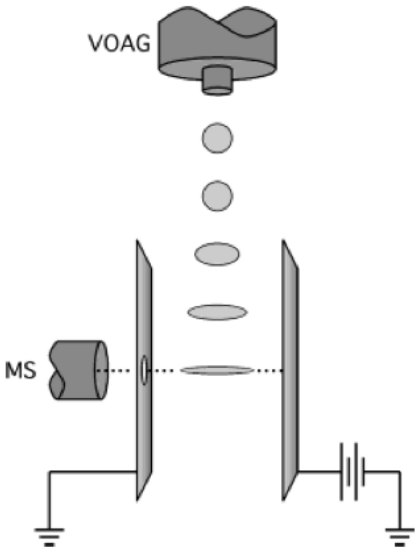

Figure 1.11: Schematic diagram outlining the field induced droplet ionization (FIDI) technique. Microdroplets are generated from a VOAG and free-fall between two charged metal plates. The electric field between these plates induces breakdown of the microdroplet, generating charged species that are subsequently sampled by the mass spectrometer through the hole in the grounded plate. Reprinted figure with permission from R. L. Grimm and J. L. Beauchamp, Field-induced droplet ionization mass spectrometry, Journal of Physical Chemistry B, **107**, 1416114163, 2003 [40]. Copyright (2016) American Chemical Society.

Aside from mass spectrometry, free-falling single microdroplets have been utilised for optical chemical identification using Raman spectroscopy [11, 16, 17]. In a study published in 2003, Hopkins *et al.* used cavity-enhanced Raman scattering to probe the size and composition of single water microdroplets containing ethanol. Microdroplets were generated using a VOAG and subsequently probed with a pulsed Nd:YAG laser, operating at the 2nd (λ = 532 nm) or 3rd harmonic (λ = 355 nm), with the Raman emission collected by a CCD equipped spectrograph [45]. By comparing the intensity of this signal relative to the O–H stretching Raman

band of the water, a calibration curve for ethanol concentration was generated. The study showed that over the concentration range of 7.5 – 19% the C-H stretch Raman band of the ethanol could be observed in single spectra [11].

This study went on to show that by probing microdroplets at different fall times, a time dependent decrease in ethanol concentration was observed thus providing insight into the evaporation dynamics [11]. Results coupled with established theoretical evaporation models revealed that the vapour pressure of the ethanol was found to be higher than literature by a factor of two [12]. A later study in 2006, expanded this study to investigate mass transfer in water microdroplets containing methanol, ethanol and 1-propanol. They found that when a scaling factor was included to account for the Raman probe volume, it was possible to measure the vapour pressure and activity coefficients of the droplet components [13].

In addition to these studies on evaporation, Reid and coworkers published studies using this technique for investigation into the chemical composition of single water microdroplets containing the nitrate and sulfate anions [17] as well as ethanol and methanol [16].

In 2005, Symes *et al.* investigated water microdroplets with varying concentrations of nitrate and sulfate. By comparing the intensity of the N–O and S–O stretching Raman bands of nitrate and sulfate, respectively, to the O–H stretching band of the water solvent, calibration curves for the concentration of both anions were generated [17]. From this study they found there was two major factors limiting the detection of SRS from single microdroplets. The first was that the target species had to be above a certain concentration threshold for the observation of Raman scattering. Secondly, the target chemical must have a broad enough Raman band, in this case the water-solvated N–O and S–O stretching bands, to envelope at least one cavity mode of the microdroplet, otherwise no cavity-enhanced Raman emission would be measured. This study found that this technique had a detection limit of 0.3 M for both sulfate and nitrate, which is much greater than typical atmospheric aerosol conditions [17].

In a following study published by Symes and Reid in 2006, the chemical composition of microdroplets containing ethanol and methanol was investigated using both narrow- and broadband light source [16]. The narrowband light source was a pulsed Nd:YAG laser, much like the previously studies, while the broadband light source was a Nd:YAG pumped dye laser. This study showed that by varying the linewidth of the probe light source, the detectable concentration range could be expanded. The results showed that while the narrowband laser light source could probe up to 60% and 50% v/v concentrations for ethanol and methanol respectively, broadband light sources expanded this range to 90% and 80% v/v, respectively [16]. Additionally, it was shown that calibration curves for any linewidth probe

source could be developed using a combination of data collected from a narrowband probe coupled with bulk-phase Raman studies and that the resulting calibration was independent of droplet size [16].

These studies have shown that while there has been large advances in single particle techniques, there is limited research focusing on chemistry within single microdroplets. There are almost no studies examining photochemistry in single microdroplets. In order to overcome this, the development of new techniques with the capability to probe fast chemical dynamics in single microparticles is required. With the use of highly reproducible streams of single droplets coupled with precisely timed optical spectroscopy this gap in technology can be bridged.

1.2 Drop-on-demand droplet generation

Many of the aforementioned microdroplet studies incorporated vibrating orifice aerosol generators (VOAG) as the single microdroplet production method [15, 35, 45]. The typical operating frequency of a VOAG is in the kilohertz range which generates droplets faster than they can be measured with low repetition rate pulsed lasers (1 - 100 Hz). This leads to poor sample efficiency and timing issues. However, Drop-on-demand (DoD) droplet generators have been used to provide single microdroplets with highly reproducible droplet sizes and excellent control of timing for droplet delivery [46, 47]. The timing of droplet generation is critical for successfully performing optical measurements on single free-falling microdroplets, as shown in this doctoral work. Piezoelectrically driven DoD droplet generators are used in each technique presented in this thesis.

A schematic diagram of the droplet generator used in this doctoral work is shown in Figure 1.12 (A). As the schematic shows, along the centre of the droplet generator is a glass capillary that is encased by a piezoelectric crystal. The capillary tapers at the bottom to provide an orifice $\sim$50 μm in diameter. This capillary is connected to the sample reservoir via Teflon tubing. Wires run through the top of the generator and directly attach to the piezoelectric crystal. In this work, custom electronics are used to drive the droplet generator, with a tunable square-wave pulse supplied from a signal generator that is subsequently amplified to drive the piezoelectric crystal (described in Chapter 2).

When an appropriate potential is applied to the piezoelectric crystal it expands, compressing the capillary [48–50], as shown in Figure 1.12 (B), forcing liquid from the tip of the capillary (Figure 1.13 B). As the liquid is ejected, the pressure within the capillary reduces to ambient. The liquid continues to flow until the electrical potential returns to zero, relaxing the piezoelectric crystal [49]. Once relaxed the flow of liquid ceases, drawing some liquid back within the capillary as shown by

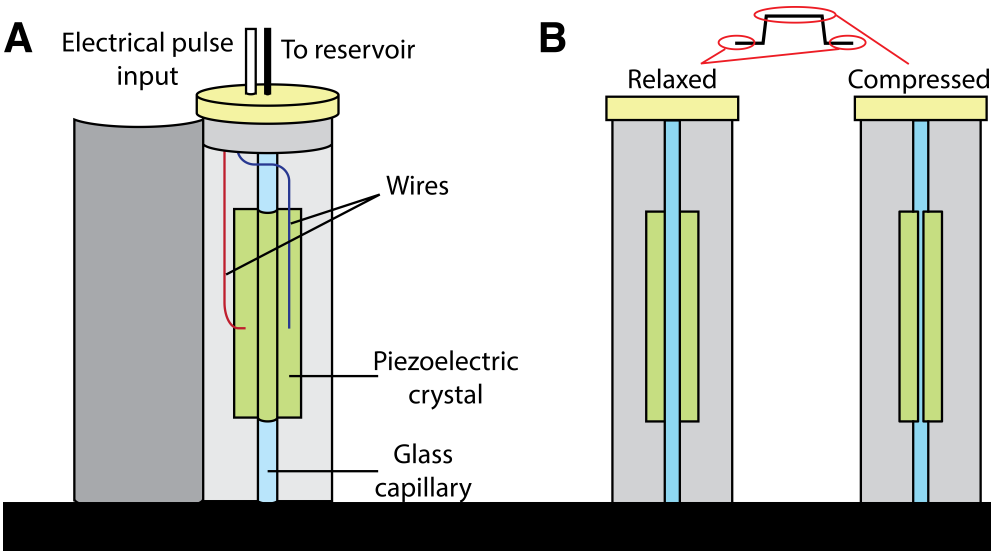

Figure 1.12: (A) Schematic of the DoD piezoactuated droplet generator used in this thesis. (B) Cross-section of droplet generator as an electrical pulse is applied. When a potential is applied the piezoelectric crystal compresses the capillary forcing liquid from the capillary forming a single droplet.

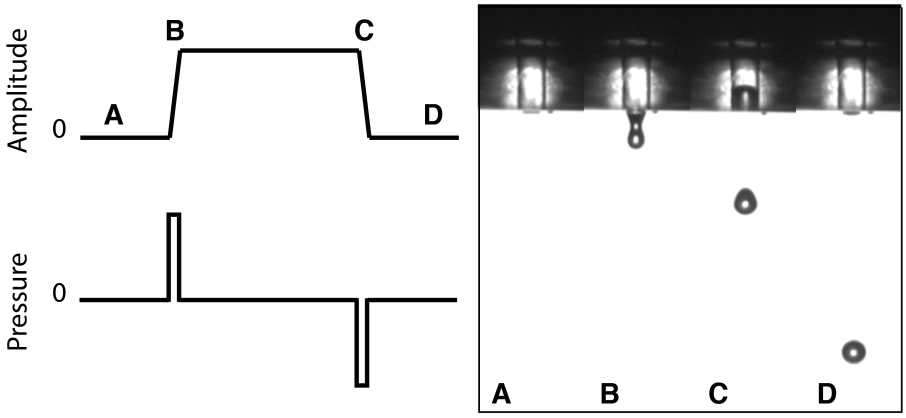

Figure 1.13: Standard square-wave voltage pulse that is applied to the DoD generator to force liquid from the tip. Letters A – D correspond to the bright-field images during droplet formation showing droplet formation visually.

the withdrawing meniscus visible in Figure 1.13 (C). The length and amplitude of the waveform play important roles in the droplet generation. If the pulse is too long, excess liquid will be forced from the tip causing additional satellite droplet formation. When too short, not enough liquid is ejected before the pressure is reduced causing no droplet to form. Similar effects occur when the driving waveform amplitude is too high/low, with either additional/no droplets forming. Waveform parameters required for generating single microdroplets change depending on the solvent properties. Effects of the driving waveform on droplet size and stability is explored in detail in Chapter 2.

1.3 Thesis Overview

This doctoral thesis describes the development and characterisation of two techniques to probe photoinitiated chemistry within single microdroplets. One technique uses optical spectroscopy to measure time-dependent chemical processes in single microdroplets. The second incorporates single microdroplets as an ionisation method for a commercial mass spectrometer, where the microdroplets act as reaction vessels to probe the photochemistry and photophysics of a condensed phase system. This thesis contains a further five chapters in the following order:

• Chapter 2 describes the characterisation of a Drop-on-Demand microdroplet generator for single microdroplet experiments that are reported in later chapters. This study investigates the potential of DoD microdroplet generators in regards to generating reproducible and stable streams of single microdroplets as well as controllability of microdroplet size.

• Chapter 3 reports a new experimental technique to observe radical iodine recombination kinetics in single microdroplets of iodododecane. Using a precisely timed two-laser setup, iodine radicals are generated by UV photolysis of the C-I bond in 1-iodododecane. The radical recombination is monitored temporally by a decrease in stimulated Raman scattering signal collected from the microdroplet. This study has been published in its current form as Vaughn *et al.*, Chem. Phys. Lett., 551, 134 - 138 (2012).

• Chapter 4 investigates hydroxyl radical chemistry using a known hydroxyl radical scavenger, terephthalate. Single microdroplets containing hydrogen peroxide, as a photoinitiated hydroxyl radical precursor, are irradiated with a UV laser pulse initiating the radical chemistry. As the hydroxyl radicals react with terephthalate a fluorescent product, hydroxyterephthalate, is formed. Using a second pulsed laser system, the fluorescence of this product is measured. By precisely controlling the timing of both laser systems the time dependent growth of the fluorescence product is measured.

• Chapter 5 outlines the single microdroplet desorption mass spectrometry technique published by Tracey *et al.* Analytical Chemistry, **86**, 2895-2899 (2014). This study investigates the photochemistry and photophysics of the berberine cation, a well-studied alkaloid containing an iminium salt, by probing the reaction products from the UV irradiation of single droplets prior to desorption. The photochemistry in single microdroplets is compared to bulk-phase and gas-phase

photochemical studies.

• Chapter 6 summarises the finding of this doctoral work and presents some future directions.

1.4 References for Chapter 1

(1) J. B. Wills, J. K. Knox and J. P. Reid, "Optical control and characterisation of aerosol", *Chemical Physics Letters*, 2009, **481**, 153–165.

(2) J. P. Reid and L. Mitchem, "Laser probing of single-aerosol droplet dynamics", *Annual Review of Physical Chemistry*, 2006, **57**, 245–271.

(3) U. K. Krieger, C. Marcolli and J. P. Reid, "Exploring the complexity of aerosol particle properties and processes using single particle techniques", *Chemical Society Reviews*, 2012, **41**, 6631–6662.

(4) J. P. Reid, H. Meresman, L. Mitchem and R. Symes, "Spectroscopic studies of the size and composition of single aerosol droplets", *International Reviews in Physical Chemistry*, 2007, **26**, 139–192.

(5) R. E. H. Miles, A. E. Carruthers and J. P. Reid, "Novel optical techniques for measurements of light extinction, scattering and absorption by single aerosol particles", *Laser & Photonics Reviews*, 2011, **5**, 534–552.

(6) J. R. Butler, J. B. Wills, L. Mitchem, D. R. Burnham, D. McGloin and J. P. Reid, "Spectroscopic characterisation and manipulation of arrays of sub-picolitre aerosol droplets", *Lab on a Chip*, 2009, **9**, 521–528.

(7) R. E. H. Miles, J. P. Reid and I. Riipinen, "Comparison of Approaches for Measuring the Mass Accommodation Coefficient for the Condensation of Water and Sensitivities to Uncertainties in Thermophysical Properties", *Journal of Physical Chemistry A*, 2012, **116**, 10810–10825.

(8) B. J. Dennis-Smither, R. E. H. Miles and J. P. Reid, "Oxidative aging of mixed oleic acid/sodium chloride aerosol particles", *Journal of Geophysical Research: Atmospheres*, 2012, **117**, D20204, 1–13.

(9) J. F. Davies, A. E. Haddrell and J. P. Reid, "Time-Resolved Measurements of the Evaporation of Volatile Components from Single Aerosol Droplets", *Aerosol Science and Technology*, 2012, **46**, 666–677.

(10) F. D. Pope, B. J. Dennis-Smither, P. T. Griffiths, S. L. Clegg and R. A. Cox, "Studies of Single Aerosol Particles Containing Malonic Acid, Glutaric Acid, and Their Mixtures with Sodium Chloride. I. Hygroscopic Growth", *The Journal of Physical Chemistry A*, 2010, **114**, 5335–5341.

(11) R. Hopkins, R. Symes, R. Sayer and J. Reid, "Determination of the size and composition of multicomponent ethanol/water droplets by cavity-enhanced Raman scattering", *Chemical Physics Letters*, 2003, **380**, 665–672.

(12) R. J. Hopkins and J. P. Reid, "Evaporation of ethanol/water droplets: Examining the temporal evolution of droplet size, composition and temperature", *The Journal of Physical Chemistry A*, 2005, **109**, 7923–7931.

(13) R. J. Hopkins and J. P. Reid, "A comparative study of the mass and heat transfer dynamics of evaporating ethanol/water, methanol/water, and 1-propanol/water aerosol droplets", *Journal of Physical Chemistry B*, 2006, **110**, 3239–3249.

(14) S. F. Simpson, J. R. Kincaid and F. J. Holler, "Microdroplet mixing for rapid reaction-kinetics with Raman spectrometric detection", *Analytical Chemistry*, 1983, **55**, 1420–1422.

(15) S. F. Simpson, J. R. Kincaid and F. J. Holler, "Development of a micro droplet mixing technique for the study of rapid reactions by Raman spectroscopy", *Analytical Chemistry*, 1986, **58**, 3163–3166.

(16) R. Symes and J. P. Reid, "Determining the composition of aqueous microdroplets with broad-band cavity enhanced Raman scattering", *Physical Chemistry Chemical Physics*, 2006, **8**, 293–302.

(17) R. Symes, R. J. J. Gilham, R. M. Sayer and J. P. Reid, "An investigation of the factors influencing the detection sensitivity of cavity enhanced Raman scattering for probing aqueous binary aerosol droplets", *Physical Chemistry Chemical Physics*, 2005, **7**, 1414–1422.

(18) R. L. Grimm and J. L. Beauchamp, "Evaporation and discharge dynamics of highly charged multicomponent droplets generated by electrospray ionization", *Journal of Physical Chemistry A*, 2010, **114**, 1411–9.

(19) H. I. Kim, H. Kim, Y. S. Shin, L. W. Beegle, W. A. Goddard, J. R. Heath, I. Kanik and J. L. Beauchamp, "Time resolved studies of interfacial reactions of ozone with pulmonary phospholipid surfactants using field induced droplet ionization mass spectrometry", *Journal of Physical Chemistry B*, 2010, **114**, 9496–503.

(20) W. Kleinekofort, J. Avdiev and B. Brutschy, "A new method of laser desorption mass spectrometry for the study of biological macromolecules", *International Journal of Mass Spectrometry and Ion Processes*, 1996, **152**, 135–142.

(21) F. Sobott, A. Wattenberg, W. Kleinekofort, A. Pfenninger and B. Brutschy, "Laser desorption mass spectrometry on thin liquid jets", *Fresenius' Journal of Analytical Chemistry*, 1998, **360**, 745–749.

(22) R. D. B. Gatherer, R. M. Sayer and J. P. Reid, "An optical method for determining size distributions of water droplets", *Chemical Physics Letters*, 2002, **366**, 34–41.

(23) B. S. Vaughn, P. J. Tracey and A. J. Trevitt, "Laser-initiated iodine radical chemistry in single microdroplets", *Chemical Physics Letters*, 2012, **551**, 134–138.

(24) L. Lorenz, "Lysbevaegelsen i og uden for en af plane Lysbolger belyst Kugle", *Det Kongelige Danske Videnskabernes Selskabs Skrifter*, 1890, **6**, 1–62.

(25) G. Mie, "Beitrage zur Optik truber Medien, speziell kolloidaler Metallosungen", *Annalen der Physik*, 1908, **330**, 377–445.

(26) R. A. Millikan, "The Isolation of an Ion, a Precision Measurement of its Charge, and the Correction of Stokes's Law", *Physics Reviews (Series I)*, 1911, **32**, 349–397.

(27) R. A. Millikan, "XXII. A new modification of the cloud method of determining the elementary electrical charge and the most probable value of that charge", *Philosophical Magazine Series 6*, 1910, **19**, 209–228.

(28) F. T. Gucker and R. L. Rowell, "The angular variation of light scattered by single dioctyl phthalate aerosol droplets", *Discussions of the Faraday Society*, 1960, **30**, 185.

(29) F. T. Gucker and J. J. Egan, "Measurement of the angular variation of light scattered from single aerosol droplets", *Journal of Colloid Science*, 1961, **16**, 68–84.

(30) A. Ashkin, "Acceleration and trapping of particles by radiation pressure", *Physical Review Letters*, 1970, **24**, 156–159.

(31) A. Ashkin and J. M. Dziedzic, "Optical levitation by radiation pressure", *Applied Physics Letters*, 1971, **19**, 283–285.

(32) D. McGloin and J. P. Reid, "Forty Years of Optical Manipulation", *Optics & Photonics News*, 2010, **21**, 20–26.

(33) A. Ashkin and J. M. Dziedzic, "Observation of resonances in radiation pressure on dielectric spheres", *Physical Review Letters*, 1977, **38**, 1351–1354.

(34) R. E. Benner, P. W. Barber, J. F. Owen and R. K. Chang, "Observation of structure resonances in the fluorescence-spectra from microspheres", *Physical Review Letters*, 1980, **44**, 475–478.

(35) J. B. Snow, S. .-.-X. Qian and R. K. Chang, "Stimulated Raman scattering from individual water and ethanol droplets at morphology-dependent resonances", *Optics Letters*, 1985, **10**, 37–39.

(36) R. Thurn and W. Kiefer, "Raman-Microsampling Technique Applying Optical Levitation by Radiation Pressure", *Applied Spectroscopy*, 1984, **38**, 78–83.

(37) J. F. Owen, R. K. Chang and P. W. Barber, "Morphology-dependent Resonances in Raman-scattering, fluorescence emission, and elastic-scattering from microparticles", *Aerosol Science and Technology*, 1982, **1**, 293–302.

(38) H. M. Tzeng, K. F. Wall, M. B. Long and R. K. Chang, "Laser emission from individual droplets at wavelengths corresponding to morphology-dependent resonances", *Optics Letters*, 1984, **9**, 499–501.

(39) N. Morgner, H. D. Barth and B. Brutschy, "A new way to detect noncovalently bonded complexes of biomolecules from liquid micro-droplets by laser mass spectrometry", *Australian Journal of Chemistry*, 2006, **59**, 109–114.

(40) R. L. Grimm and J. L. Beauchamp, "Field-induced droplet ionization mass spectrometry", *Journal of Physical Chemistry B*, 2003, **107**, 14161–14163.

(41) R. L. Grimm and J. L. Beauchamp, "Dynamics of field-induced droplet ionization: time-resolved studies of distortion, jetting, and progeny formation from charged and neutral methanol droplets exposed to strong electric fields", *Journal of Physical Chemistry B*, 2005, **109**, 8244–50.

(42) J. Hoffmann, T. L. Schmidt, A. Heckel and B. Brutschy, "Probing the limits of liquid droplet laser desorption mass spectrometry in the analysis of oligonucleotides and nucleic acids", *Rapid Communications in Mass Spectrometry*, 2009, **23**, 2176–80.

(43) L. Sokolova, I. Wittig, H. D. Barth, H. Schagger, B. Brutschy and U. Brandt, "Laser-induced liquid bead ion desorption-MS of protein complexes from blue-native gels, a sensitive top-down proteomic approach", *Proteomics*, 2010, **10**, 1401–7.

(44) M. Cernescu, T. Stark, E. Kalden, C. Kurz, K. Leuner, T. Deller, M. Gobel, G. P. Eckert and B. Brutschy, "Laser-induced liquid bead ion desorption mass spectrometry: an approach to precisely monitor the oligomerization of the beta-amyloid peptide", *Analytical Chemistry*, 2012, **84**, 5276–84.

(45) R. D. B. Gatherer, R. M. Sayer and J. P. Reid, "An optical method for determining size distributions of water droplets", *Chemical Physics Letters*, 2002, **366**, 34–41.

(46) B. Derby, "Inkjet Printing of Functional and Structural Materials: Fluid Property Requirements, Feature Stability, and Resolution", *Annual Review of Materials Research*, 2010, **40**, 395–414.

(47) G. D. Martin, S. D. Hoath and I. M. Hutchings, "Inkjet printing - the physics of manipulating liquid jets and drops", *Journal of Physics: Conference Series*, 2008, **105**, 012001.

(48) A. A. Castrejón-Pita, J. R. Castrejón-Pita and G. D. Martin, "A novel method to produce small droplets from large nozzles", *Reviews of Scientific Instruments*, 2012, **83**, 115105.

(49) A. U. Chen and O. A. Basaran, "A new method for significantly reducing drop radius without reducing nozzle radius in drop-on-demand drop production", *Physics of Fluids*, 2002, **14**, L1–L4.

(50) H. Y. Gan, X. C. Shan, T. Eriksson, B. K. Lok and Y. C. Lam, "Reduction of droplet volume by controlling actuating waveforms in inkjet printing for micro-pattern formation", *Journal of Micromechanics and Microengineering*, 2009, **19**, 8.

Chapter 2

Microdroplet generator characterisation

This chapter describes the process of characterising a Drop-on-Demand microdroplet generator. The work shown in Section 2.1 has been published in its current form as the following peer-reviewed publication:

Bartholomew S. Vaughn, Phillip J. Tracey and Adam J. Trevitt, Drop-on-Demand microdroplet generation: a very stable platform for single-particle experimentation, *RSC Advances* **6**, 60215-60222 (2016).

Reproduced in Appendix B

Author contributions
Bartholomew S. Vaughn performed all the experiments with the assistance of Phillip J. Tracey. Bartholomew S. Vaughn prepared the manuscript which was edited by Adam J. Trevitt. Adam J. Trevitt is the corresponding author.

Certification
I, Assoc. Prof. Adam J. Trevitt, as Bartholomew S. Vaughn's supervisor and the principal investigator on this project, agree with and certify the author contributions described above.

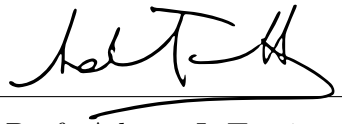

Assoc. Prof. Adam. J. Trevitt

16/11/16

Date

2.1 Drop-on-Demand microdroplet generation: a very stable platform for single-droplet experimentation

2.1.1 Abstract

This chapter reports the performance of drop-on-demand piezo-activated microdroplet generation, investigated using microdroplet cavity-enhanced fluorescence spectroscopy. Aqueous microdroplets, doped with a fluorescent dye, exhibit fluorescence spectra that are dominated by cavity resonances (termed whispering gallery modes) that, when analysed using Mie theory, allow for the determination of the radius of each microdroplet. The effect of controlled changes in the square-wave droplet generator voltage waveform on droplet size is investigated as well as the size reproducibility of successive microdroplets. Furthermore, using custom square-wave waveforms, microdroplet radii spanning ∼10 to 30 μm are produced from the same droplet dispenser. These non-standard waveforms do not sacrifice the reproducibility of microdroplet generation with <1% size variation. Tuning the single square-wave pulsewidths induces predictable changes in the microdroplet radius with steps on the order of tens of nanometers detectable. With finer voltage adjustments the microdroplet size is essentially tunable. These results confirm the extremely high stability and reproducibility of on-demand microdroplet generation and that precise size control is possible, rendering them suitable platforms for many applications in fundamental and applied research in areas including mass spectrometry, aerosol investigations and liquid-phase chemistry.

2.1.2 Introduction

Free liquid microdroplets are present in many environments including clouds, ocean sprays, fuel sprays and medical nebulizers. As the surface-to-volume ratio of a microdroplet is relatively large, while still comprising a significant liquid volume, the chemistry and physical properties of microdroplet ensembles are intriguing but challenging to study. In the laboratory, the controlled production of single microdroplets allows for convenient study of liquid-phase processes and provides a useful means of transporting small portions of liquid in a reproducible manner. The focus of this chapter is drop-on-demand generation (DoD) of free liquid microdroplets. DoD techniques are distinguished here from sprays and vibrating orifice generators that produce higher numbers of droplets per second which, while having their own virtues, are generally not suited for the precise delivery of microdroplets one at a time at low repetition rates. One advantage of precision

DoD generation is that every newly arriving microdroplet is a fresh chemical system, allowing chemical and physical changes to be studied with no cross-contamination between microdroplets [1].

The DoD dispensers typically operate when a potential is applied in a short pulse ($\sim$30 μs) to a piezoelectric crystal that surrounds a liquid filled capillary. This pulse briefly compresses the capillary and causes a small portion of liquid to exit the nearby capillary orifice [2–4]. The size of the resulting liquid droplet is generally determined by the capillary inner diameter, the characteristics of the applied potential pulse (including pulsewidth and amplitude), in addition to the physical properties of the liquid (e.g. viscosity and surface tension). Employing a more complex voltage pulse waveform can markedly change the droplet size [3–6]. Tuning droplet size by controlling the fluid pressure has been demonstrated [7].

DoD droplet dispensers most are commonly deployed in inkjet printing platforms as they offer great control over droplet delivery timing and liquid volume [8, 9]. Inkjet printing exploits the droplet stream generated from the dispenser to deposit a thin layer of liquid onto a substrate and is commonly implemented, for example, in the generation of graphics [10], deposition of biomaterials [11, 12] and fabrication of electronic circuits [13]. In order to achieve a clean and even thin-layer on the substrate the droplets must be highly reproducible and most commercial inkjet dispensers having droplet size reproducibility of $\sim$1%. [14] This suggests that DoD dispensers may be well-suited as platforms for fundamental physical and chemical single droplet studies.

A notable application of DoD microdroplet generation is in the coupling with mass spectrometry with several groups incorporating different desorption and ionization strategies. One groundbreaking example is the “soft” laser desorption of ions from single microdroplets delivered into vacuum environments [15–19]. In these experiments, single microdroplets are launched into the low pressure (10^{-4} – 10^{-5} Torr) source region of a mass spectrometer and ions are desorbed when a pulsed IR laser, tuned to a vibrational absorption band of the water solvent ($\sim$2.9 μm), irradiates the droplet. Using microdroplets in this case ensures that the vacuum chamber is not overloaded with unnecessary solvent and the laser pulse overlaps entirely with the liquid sample. The gentler laser desorption conditions enabled the detection of intact biological-relevant non-covalent complexes [16]. Furthermore, as the volume of each microdroplet is on the order of 50 pL, extremely small amounts of chemical sample are consumed. In other experiments, microdroplets have been used to introduce samples to mass spectrometers at atmospheric pressure using a needle-probe electrospray configuration [1] to investigate laser photochemistry in single microdroplets, one droplet at a time. Another example strategy injects single microdroplets into an inductively coupled plasma source for elemental analysis

[18, 20]. High-precision generation of microdroplets has also been exploited for calibration of water-vapor isotope spectrometry [21], ionic liquid deposition [22], the study of coalescence dynamics and mixing [23] and the isolation of single biological cells [24]. The production of metal droplet in an on-demand fashion is also well studied [25–27].

This chapter reports the performance of commercially available microdroplet generators using single-droplet cavity-enhanced fluorescence spectroscopy. This cavity-enhanced emission, collected from single droplets one at a time, provides highly-precise details of droplet radius. First, it is demonstrated that generation of droplets is highly reproducible, affording a very stable and predictable platform for experiments of microdroplet systems. Secondly, the size of droplets can be altered from a single droplet dispenser, without sacrificing the stability and performance of the droplet generation. And thirdly, that the droplet size is smoothly "tunable" over a narrow size-distribution.

2.1.3 Experimental

All measurements presented in this chapter were performed on the experimental setup shown schematically in Figure 2.1. A microdroplet dispenser was held centrally within a 6-way chamber by a *x,y,z* translatable mount. This chamber (LC6W, Thorlabs) facilitates the alignment of input lasers and optics. The commercially available microdroplet dispenser (MICRODROP – MD-K-140), with an orifice diameter of 50 μm, was supplied with a voltage pulse, typically square shaped, provided by a signal generator (HAMEG 2525) and amplifier (Krohn-Hite. Model #7602). The liquid sample reservoir was open to ambient pressure with no active pressure control. As will be detailed below, more complex waveforms are possible. Each pulse produces a single droplet with droplet generation frequency ranging from $\sim$1 Hz to $\sim$1 kHz. In this study, aqueous droplets were generated at a frequency of 10 Hz to match the optimum laser pulse repetition rate. Typically the square-wave pulsewidth ranges from 30 - 80 μs with an amplified potential ranging from 50 - 150 V (V_{0-P}). The rise and fall time of the voltage pulse is approximately 7 ns. Working operating parameters, particularly the voltage and the pulsewidth, are highly dependent on the properties of the dispensed liquid.

The exit region of the droplet generator was monitored using an imaging setup comprising a CMOS camera (DCC1645C, Thorlabs) and light-emitting diode (LED) (500 mcd, λ_{max} = 660 nm) with the dispenser positioned in between (shown in Figure 2.1). Driven by a voltage pulse (3 V amplitude, 4 μs pulse-length) from a digital delay generator (DG645, Stanford Research Systems), the LED illuminates the droplet dispenser tip region at a controllable delay. The LED was pulsed for

every droplet and the light was collected and collimated using a lens (f = 75 mm), then focused (f = 200 mm) onto the CMOS camera, producing bright-field images that were viewed on a computer at a rate of 10 frames per second, matching the droplet generation frequency. By controlling the LED emission pulse timing, the early moments of the droplet formation can be inspected ensuring that the droplet production was stable during measurements. A 532 nm (±10 nm) notch rejection filter was positioned in front of the CMOS camera to eliminate elastically scattered light from the pulsed laser (λ = 532 nm) while allowing for detection of fluorescence emission.

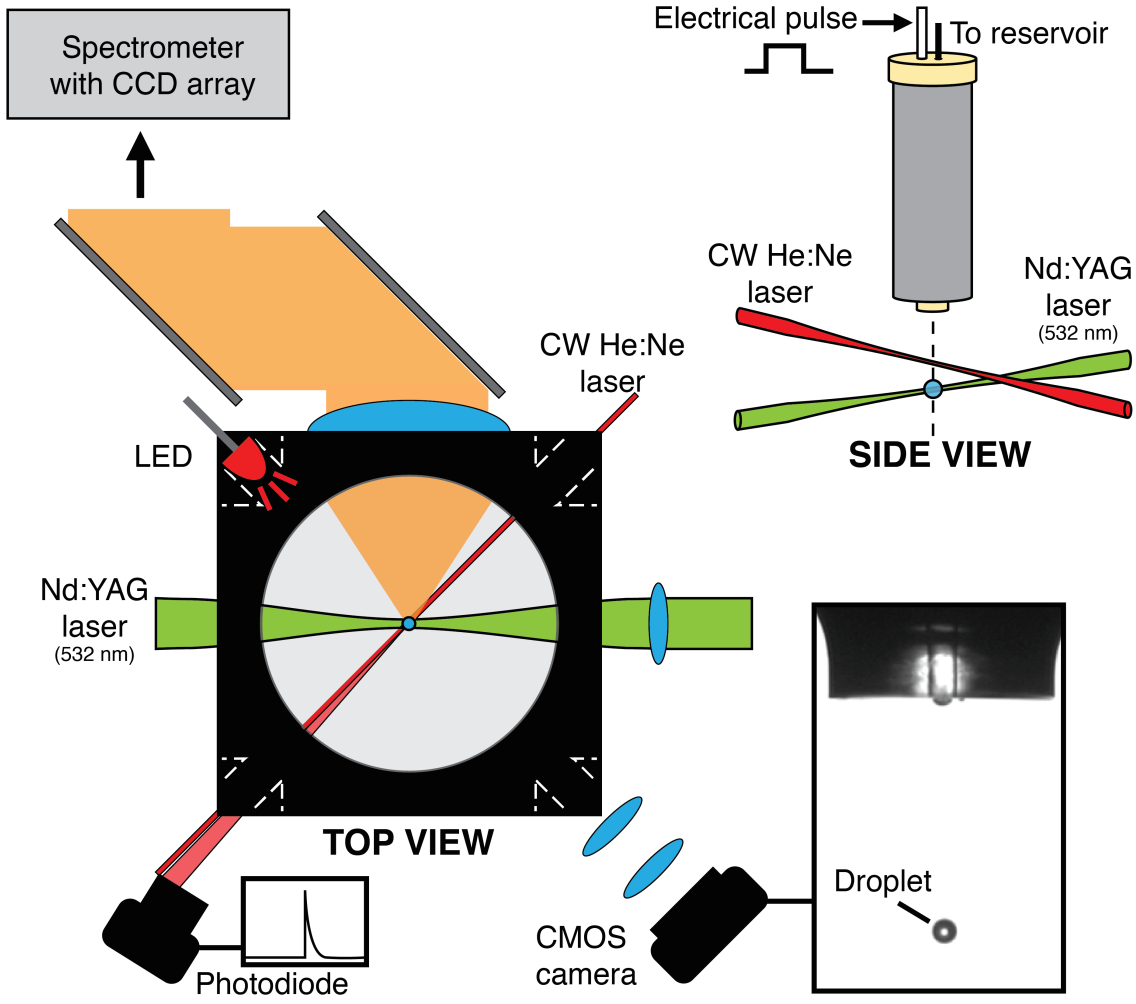

Figure 2.1: Experimental schematic showing the orientation of optics and laser inputs relative to the droplet location.

After formation, a microdroplet falls ~3 mm before passing through a continuous wave He:Ne laser beam (Thorlabs HRP020-1, 632.8 nm, 2 mW) that was focused by a lens (f = 100 mm, D = 1"). As the droplet traverses the He:Ne beam, elastically scattered light was collected by a lens (f = 75 mm, D = 1") and focused onto an amplified photodiode (Thorlabs, DET36A/M). A 632.8 nm line-pass filter ensures

only He:Ne scattered light was detected by the photodiode. This scattered light signal triggers the digital delay generator (DG645, Stanford Research Systems) that in turn, controls the timing of the spectrometer CCD exposure and read-out, the pulsing of a Nd:YAG laser (Minilite II, Continuum) and the aforementioned LED. After the triggering of the delay generator, at a controlled delay (typically 300 μs) the droplet was irradiated by a single pulse from a Nd:YAG laser operating on the second harmonic (λ = 532 nm) (Minilite II, Continuum) (*ca.* 1 kJ/cm^2 at focal point). Prior to irradiating the droplet, the Nd:YAG laser pulse passes through beam expansion optics. The expansion was performed using a Keplerian beam expander providing a 4x increase in beam waist. This expansion is used to reduce the final beam waist of the laser when ultimately focused at the droplet ($\sim$10^{-6} cm^2). To ensure each single droplet was irradiated at the same point in its fall time, this triggering and timing was crucial.

In these experiments, droplets were aqueous and contained a fluorescent dye, Rhodamine 6G (Sigma-Aldrich, 10 μM). After laser illumination, emitted light from the droplet was collected orthogonal to the excitation laser by a 2-inch lens (f = 60 mm) that collimates the collected light and directs it towards a spectrometer (Shamrock 500, Andor, 1200 lines/mm grating) via two broadband mirrors (D = 2") and then through a second 2-inch lens that was selected to best match the spectrometer's numerical aperture ($f/6$). Prior to entering the spectrometer the light is passed through a 532 nm notch rejection filter removing any elastically scattered laser light. The spectrometer is equipped with a TE-cooled (-70 C) open-electrode CCD detector (Newton, Andor). The CCD signal was processed using a custom LabView control program. Using this arrangement, single droplet laser emission spectra are collected one droplet at a time without fail.

Fluorescence and Raman spectra collected from single microdroplets are known to exhibit fine-structure peaks that correspond to microcavity resonances, often referred to as morphology dependent resonances (MDRs) or whispering gallery modes (WGMs) (see Appendix A), due to optical feedback within the microdroplet [28–32]. The WGM wavelengths depend on the droplet radius and refractive index. As is well known, fitting the measured WGM wavelengths using Mie theory allows for the extraction of droplet radius and refractive index with very good accuracy [28–35]. In the current experiments, to ascertain the radius of each droplet, the fluorescence spectrum was subjected to a peak picking routine to determine the location of the sharp peaks that correspond to WGMs. The WGMs are initially assigned guesses for polarity (TE or TM), mode order and mode number [28, 29, 35–38]. The radius and dispersion corrected refractive index were then fitted to best match the theoretical WGM positions to those observed experimentally. The reported uncertainties on these fitted quantities are reported as one standard deviation (1σ) as

determined from the least-squares fitting routine (Levenberg-Marquardt). The mode assignments are iterated to determine the overall best fit. The iterative procedure follows the general algorithm of Eversole *et al.* [28, 39]. A summary of the fitting routine used here is presented in Section 2.3. In this study, the droplets were rather large and this ultimately limits the accuracy of the analysis [40]. Notwithstanding this limitation, the intention here is to demonstrate the precision and reproducibility of the droplet generation technique and to monitor controllable changes in droplet size.

2.1.4 Results

Voltage-pulse waveform and droplet size

As a general guide, the size of the emitted microdroplet from the DOD dispenser is about the same as the dispenser's orifice diameter [3]. In practice, the droplet size depends on a range of variables including the physical properties of the solvent, the temperature and the characteristics of voltage waveform applied to the piezoelectric crystal. In the following section it will be shown that different droplet sizes are obtainable by changing the waveform applied to the dispenser and it is also demonstrated that these alternate waveforms provide excellent reproducibility and stability.

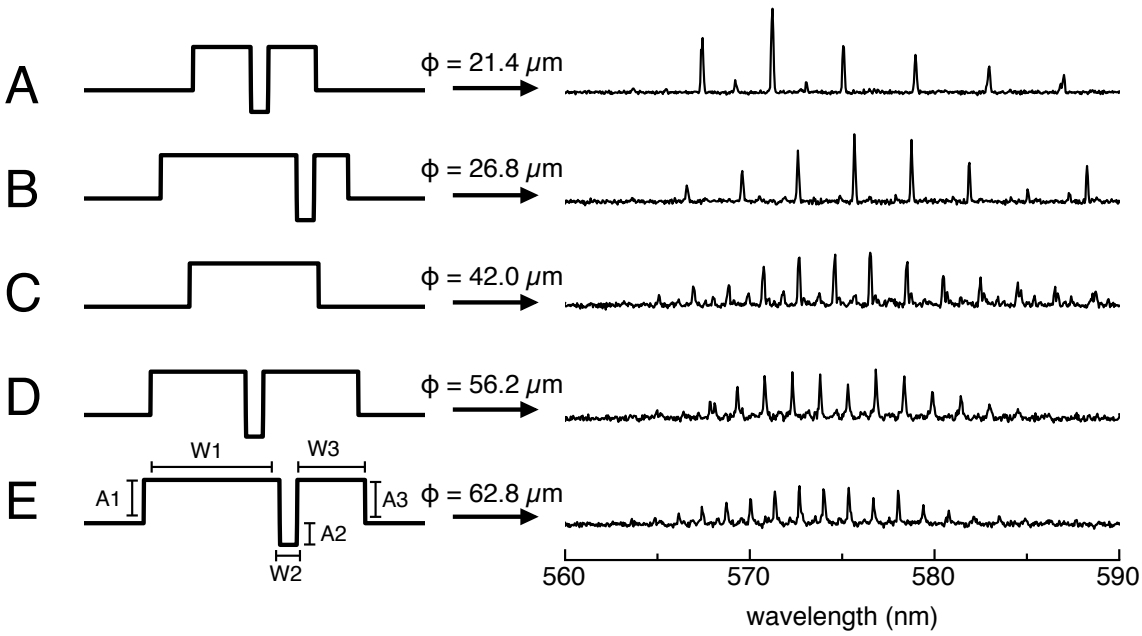

Figure 2.2: Voltage waveforms that are applied to the droplet dispenser, the corresponding single microdroplet diameters and fluorescence spectra are shown to the right. Waveform parameters are shown in Table B.1.

Figure 2.2 shows five voltage waveforms applied to the droplet dispenser and corresponding fluorescence spectrum from a single representative droplet. The size reproducibility of droplets generated from these corresponding waveforms will be examined below. The waveforms are ordered A–E from smallest to largest droplet diameter. The waveform parameters are provided in Table B.1 of the supplementary information. The waveform labeled C in Figure 2.2 is the standard square-wave pulse and the typical operating parameters for aqueous solutions range from 70 - 150 V_{0-P} amplitude and 35 – 80 μs pulse length. Waveforms A, B, D and E are examples of alternate pulse-shapes inspired by Chen and Basaran [4] and the fitted droplet diameter are shown alongside the corresponding waveform in Figure 2.2. As the droplets are labeled with the fluorescent dye Rhodamine 6G, fluorescence is collected over 560 - 590 nm. The spectra display sharp optical resonances – WGMs – that are used to calculate the droplet size and refractive index [28, 31, 33, 34, 36].

From A through E, the average spacing between the WGMs in the single-droplet fluorescence spectra decreases and is consistent with an increasing droplet size. For each case, A–E, the WGM assignments, fitted radii and refractive index terms are included in the supplementary information (Table B.2). As mentioned above, it is known for large droplets, and WGM measurements by standard CCD spectrometers, that there are limits to fitting the dispersion corrected refractive index terms and the radius as all unconstrained parameters [41]. Nevertheless, the fitted radii are in good accord with optical images that are also acquired (where the droplet diameter can be roughly measured in image "pixels").

The bright-field images shown in Figure B.1 (Supplementary information) depict shadow images of single microdroplets corresponding to each waveform (A–E) in Figure 2.2. In each image, the dispenser capillary tip, elastically scattered light from the He:Ne trigger laser and droplet fluorescence emission are all visible. The change in microdroplet size from A–E is clear from the images in Figure B.1 and the image pixel numbers provided in the supplementary information. All images are taken using the same optical arrangement and are therefore directly comparable.

It is not apparent to us that there is a clear overall systematic trend between the waveform and the ultimate droplet size but suffice to say that the pulsewidths tend to be overall longer for larger droplets.

In Figure 2.2, the fitted radii reveal that there is an appreciable range in droplet size. Thus, with a single droplet dispenser, with a fixed capillary orifice size, one can achieve a range of droplet radii, in this case from $\sim$10 to 30 μm. This corresponds to droplet volumes ranging from 4 to 113 pL; two orders of magnitude. It will be illustrated below that these alternate waveforms provide very stable droplet streams. Furthermore that reproducible size steps are achievable in addition to smooth "tuning" of the droplets' radii.

Stability and reproducibility

An important factor when altering the waveform applied to a DOD dispenser is the effect on stability – where stability is characterised here by the consistent success of droplet production, consistency in droplet size and reproducible droplet velocity/trajectory. These stability factors of droplet generation are vital for measurements where many single droplet experiments (1000+) are averaged together [1, 42]. The tracking of WGM positions can be used to detect and measure subtle changes in droplet sizes on the scale of nanometers [28, 32, 43]. Figure 2.3 shows an intensity plot of single fluorescence emission spectra measured for 1500 consecutive single droplets and is a portion of an overall set of 5000 consecutive droplets. These droplets are produced using the waveform labeled C in Figure 2.2. The two single spectra in Figure 2.3 (top) compare a single droplet emission spectrum to the average of all 1500 spectra. The FWHM peakwidth of the single droplet spectrum is 0.09 nm compared to 0.20 nm for the average of 1500. This broadening is attributed to random variations in the WGM peak positions, as the peakshape in the averaged spectrum show reasonable Gaussian distributions. The largest shot-to-shot variations observed are $\sim$0.5 nm shifts in WGM position and this is equivalent to $\sim$20 nm change in droplet radius, $\sim$0.1% of the radius – recalling that the droplet radius in this case is $\sim$21 μm. The results in Figure 2.3 reveal that the standard square-wave waveform yields highly reproducible droplets with very small random size variation ($<$0.2%).

Using the same analysis, the stability and reproducibility of the alternate waveforms are now investigated. Figure 2.4 shows a series of 1500 single droplets produced from waveform A. As previously shown, waveform A can be implemented to generate droplets significantly smaller than the 50 μm exit orifice diameter of the dispenser. As the case in Figure 2.3, the positions of the WGMs in the fluorescence spectra are tracked for each droplet over the course of the measurement. The spacing between the WGM peak positions is comparatively large as the droplets are significantly smaller. For this case A, the droplet size is extremely stable, within the limits of our spectral resolution (0.043 nm/pixel, where a WGM shift of 0.043 nm would correspond to a $\sim$2 nm change in droplet radius for a $\sim$10 μm radius droplet), with only few outlying spectra over the course of the measurement. The random fluctuations are just discernible in the zoom trace on the 571.2 nm WGM peak in Figure 2.4. The largest fluctuations observed here are shifts on the order of $\pm$0.3 nm, which corresponds to a 12 nm change in radius. Figure 2.4 also compares a single droplet spectrum to the average of the 1500 spectra shown. It shows that the reproducibility is such that the FWHM of the single droplet spectrum is essentially identical to the 1500 droplet average and presumably limited by the

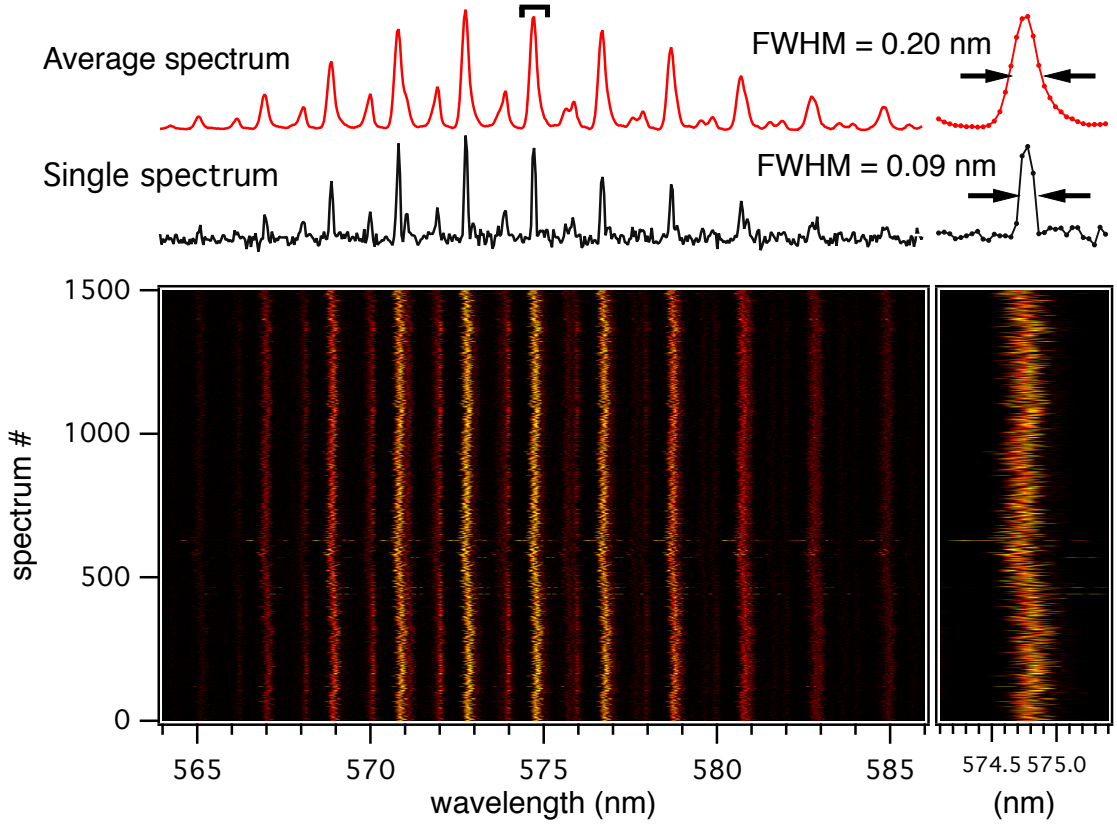

Figure 2.3: Representative spectra collected from microdroplets generated using waveform C (Figure 2.2). The red shows the average of 1500 consecutive single droplet fluorescence spectra, with the black showing a microdroplet spectrum. The intensity plot below contains the 1500 consecutive microdroplet spectra showing the WGM positions over time. The inset (right) shows an expansion of the WGM at ∼574.8 nm.

spectral resolution of the measurement, meaning that any radius fluctuations are <2 nm.

For larger droplets, the reproducibility is also very good. For waveform E, 1500 single droplets were also tracked and compared in the same way and these data are included in the supplementary information (Figure B.2). As the microdroplets produced from this waveform are much larger than the previous examples, the observed spacings between the WGMs are much smaller for the same spectral range. The WGM positions have similar stability to the previous waveform examples although this set of spectra exhibits some systematic drifting. The possible cause of drift might be temperature change experienced by the droplet generator – these are not temperature controlled droplet dispensers (although these are available). Although this systematic drift is clearly detectable, the actual droplet size drift is quite small, equating to ∼30 nm in radius over the course of the measurement (equivalent to ∼0.25 pL volume change). These results demonstrate that the complex waveforms presented in this study can produce droplet trains that have

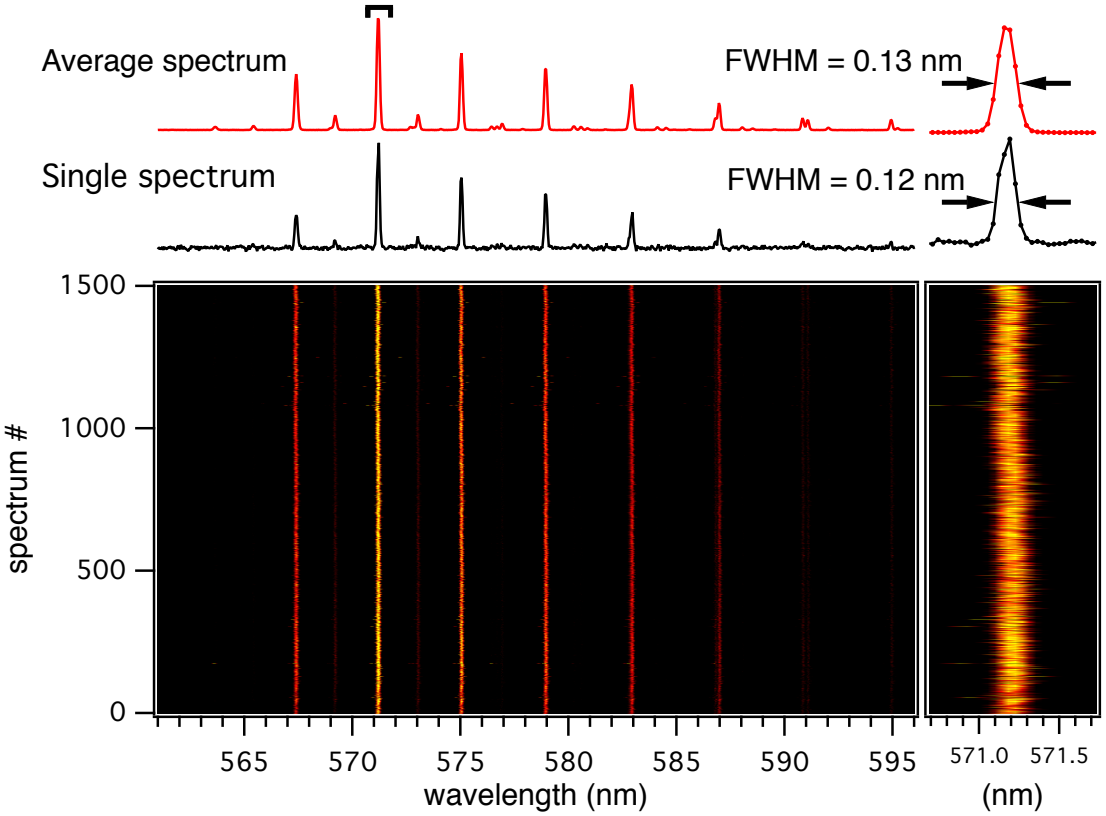

Figure 2.4: Spectra collected from microdroplets generated by waveform A (Figure 2.2). The average of 1500 consecutive droplets is shown in red, with a single microdroplet spectrum shown in black. The intensity plot below shows the 1500 consecutive single microdroplet fluorescence spectra stacked to track the WGM positions over time. The inset (right) shows an expansion of the WGM at ~571.2 nm.

excellent reproducibility, with size stability is within <0.2%.

Size stepping and tuning

We have demonstrated that altering the pulse waveform allows access to a large range of droplet sizes from the one dispenser with excellent reproducibility. The next section demonstrates that smaller size steps are possible, measurable and predictable. Figure 2.5 shows spectra from an experiment where single droplet WGMs are tracked as the square-wave pulsewidth is incrementally increased by 100 ns steps. The initial pulsewidth for this experiment was 37.1 μs, finishing at 38.1 μs to cover a total change of 1 μs. The inset in Figure 2.5 shows the pulsewidth value corresponding to the spectra. The WGM peaks show clear shifts towards longer wavelengths and this is due to the droplet size increasing, as the pulsewidth is incrementally increased.

The droplet size for each step in Figure 2.5 was calculated using the Mie Theory fitting routine – in this case the refractive index terms are held constant. By plotting

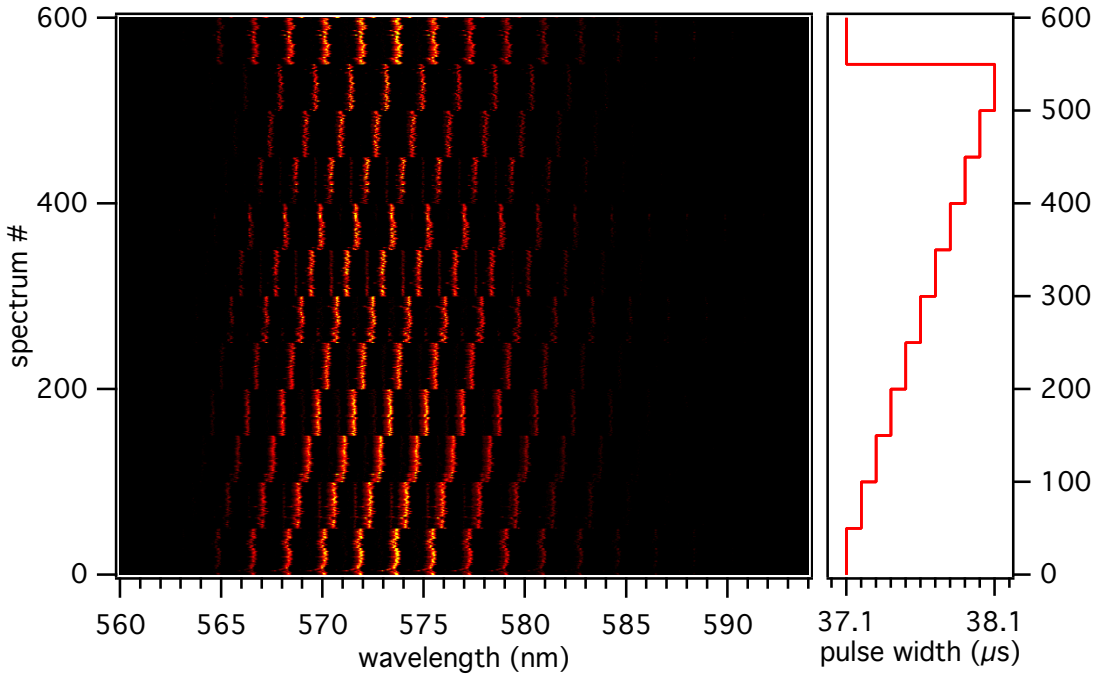

Figure 2.5: Single droplet fluorescence spectra showing WGM positions over time as the droplet generation potential is systematically stepped. The micrdroplet generator pulse is a square wave pulse ranging from 37.1 to 38.1 μs as indicated on the right panel. Every 50 droplets the pulse width is increased by 100 ns as shown on the right where the pulsewidth is plotted along side the spectrum number.

the fitted radii at each increment against the voltage pulsewidth (Figure 2.6) a linear trend is apparent. This measurement was repeated nine times (Figure 2.6 displays one iterant). The average radius change was measured to be 17.3 $\pm$ 2.3 nm (1σ) per 100 ns pulsewidth increment. This result can be recast as a size-change coefficient: 0.173 $\pm$ 0.023 nm/ns.

This procedure was then repeated for different pulsewidth increments (50 – 400 ns). When all these data are plotted against the pulsewidth step-size, the relative radius change also follows a linear trend (Figure 2.7). The data was fitted using linear regression, shown by the solid line in Figure 2.7. The gradient of the line is 0.172 $\pm$ 0.015 nm/ns (1σ), which is the same size-change coefficient, within the uncertainty, as the measured change in radius per nanosecond of pulse width for the 100 ns increment measurement (0.173 $\pm$ 0.023 nm/ns). The larger error bars for the larger step sizes in Figure 2.7 arise from a smaller sample size in those measurements.

When the same measurement was performed using 10 ns increments, shown in Figure 2.8, no resolvable steps were detected within our spectral resolution (0.043 nm/pixel). However, over the whole 1 μs range, when 100 steps of 10 ns are performed, an overall 4.8 nm shift in WGM position is measured. There is the appearance of smoothly tuning droplet size. This total shift in WGM peak position

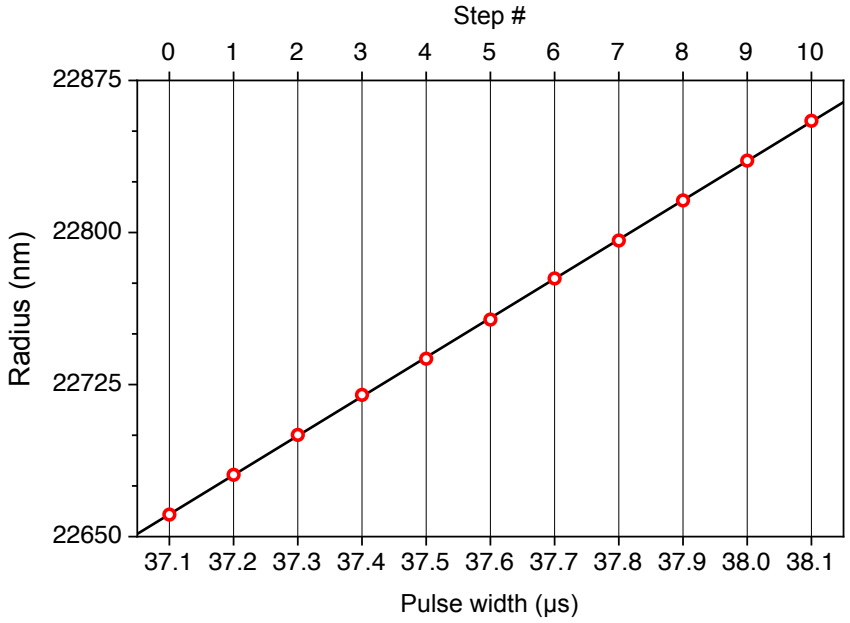

Figure 2.6: Calculated radii at each pulse width increment. Each step is an increment of 100 ns.

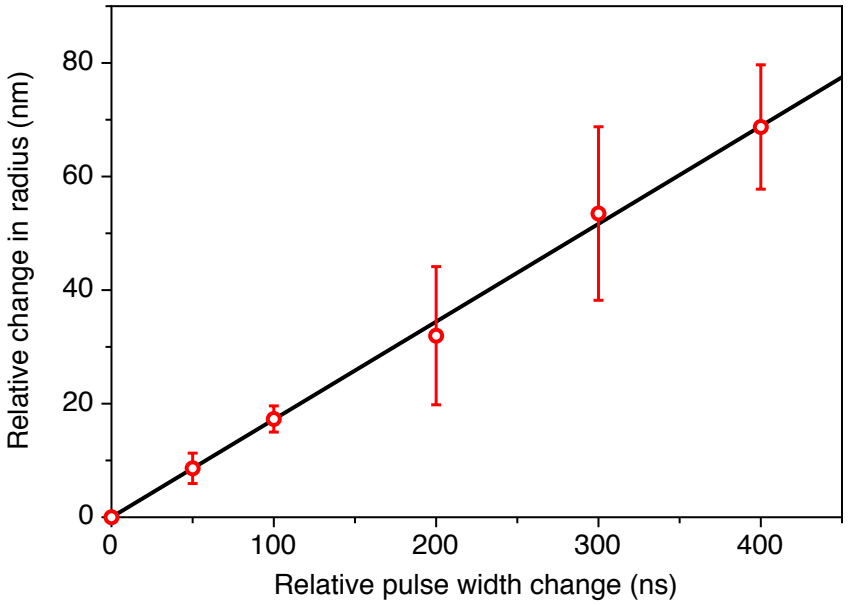

Figure 2.7: Measured average relative change in radius induced depending on the magnitude of the relative change in pulsewidth.

is the same total shift that is observed in the 100 ns increment set (Figure 2.5). The size-change coefficient is calculated in this case as 0.179 nm/ns. This shows that by varying the driving waveform provided to DOD dispensers, one can not only access large changes in the resulting droplet radius and also finely and controllably tune the droplet radii with good precision (below <10 nm). We also note that these data described in Figure 2.7 were acquired over many experimental days from the same stock solution. As all size change-coefficients are the same, there is good

predictability in the size change as the voltage pulsewidth is changed.

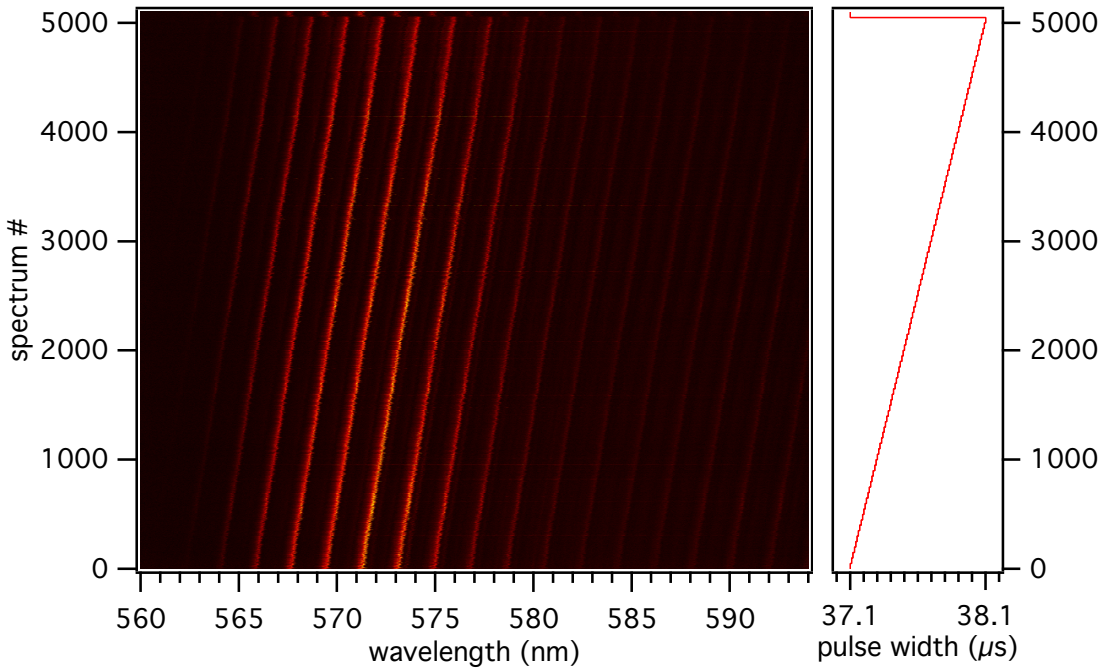

Figure 2.8: Consecutive single droplet fluorescence spectra stacked showing WGM positions over time as the droplet generation potential is systematically increased. The dye-doped droplets were generated using a standard square wave pulse (PW = 37.1 – 38.1 μs). Every 50 droplets the pulse width is increased by 10 ns as shown by the inset showing the pulse width change vs. spectrum number.

2.1.5 Conclusions

The conclusion of this study can be summarised as follows:

- A DoD microdroplet dispenser with ∼50 μm diameter orifice can produce droplets with radii ranging ∼10 to 30 μm (∼5 to 110 pL), by altering the shape of the waveform.Very stable droplet streams were recorded by monitoring WGM present in the fluorescence emission of dye-labeled microdroplets. Droplet size reproducibility was deemed excellent with <1% size variation measured for each waveform presented.

- By controlling the pulsewidth of the square-wave pulse it is possible to change the droplet size, stepwise, in discrete and reproducible increments. A linear relationship was established between the voltage pulse-width and the measuring shift in droplet radius, with a size-change coefficient of 0.173 ± 0.023 nm/ns.

- Finally, it is shown that it is possible to smoothly "tune" microdroplet size by scanning the pulsewidth of the square wave pulse in nanosecond increments.

In a temperature controlled laboratory, with relatively slow temperature variations on the order of 0.1 C, we assume that any changes in the physical properties of the liquid sample (viscosity, surface tension and density) negligibly affect the observed droplet shot-to-shot size fluctuations – temperature drifts may be more of an issue for longer timescale systematic deviations in droplet size. It is likely that the main variable affecting shot-to-shot variability in droplet size is the voltage of the square-wave pulse. Voltage fluctuations of less than a percent are likely to affect the droplet size distribution. But, as is evident from Figure 2.4, the production of micrometer diameter droplets can have an extremely narrow size distribution. A companion, systematic study of the voltage response would be desirable but maintaining stable voltages and precisely/reproducibly altering the applied voltage is significantly more difficult in practice than stepping the applied pulse-width. For broader application in inkjet printing, first-drop reliability and careful priming of the system prior to first-drop generation, would need to be carefully considered.

Ultimately, we have shown that microdroplet DoD generators are a very stable and convenient way to deliver small portions of liquid with very high levels of reproducibly and that microdroplet size can be altered – either by a large or small extent – by manipulation of the pulse waveforms. These alterations in the waveform do not sacrifice the reproducibility of microdroplet generation. A final point to note is that single droplets are typically on the order of 50 pL volume – therefore millions of single droplets can be dispensed with only a few mL of solvent consumed.

2.2 Additional Studies

In addition to the measurements shown in Section 2.1, where water was the only solvent, other studies were performed to investigate the microdroplet dispenser's stability when using other common solvents. The solvents were chosen as they are common solvents that are encountered throughout many chemical fields as well as photochemical and chemical kinetics measurements. Understanding how the microdroplet generator handles these solvents is key to designing the experimental conditions for single microdroplet measurements.

In order to measure the stability of the resulting droplets from these solvents the Raman spectra from a thousand consecutive single microdroplets were collected for each of the chosen solvents. The solvents included methanol, dimethylsulfoxide (DMSO), acetonitrile and acetone. The resulting single microdroplet Raman spectra are shown in the intensity plots in Figure 2.9. The average Raman spectrum from the thousand microdroplets for each solvent is shown in red above the respective intensity plots with representative single microdroplet Raman spectrum in black. As each intensity plot shows there is only a single main WGM observed for each solvent. This is due to the emission that is being measured resulting from the narrow C–H stretching band of each of these solvents, which occurs at $\sim$3000 cm^{-1}. The only solvent that appears to have a second minor peak is methanol and this is due to its C–H stretching band being much broader than the other solvents. As the cavity enhancement only impacts on the light trapped within the micrdroplet, it only improves the signal of the Raman scattered light. Since the C–H band of methanol is broader than the other solvents the resulting Raman emission spans a greater spectral range, leading to two cavity modes being observable. As there is only one or two peaks observed in each of these spectra no accurate microdroplet sizes can be obtained. But since the observed WGMs are consistent throughout each measurement, it shows that the generated microdroplets from these solvents are as stable as the microdroplets produced from water that were shown previously.

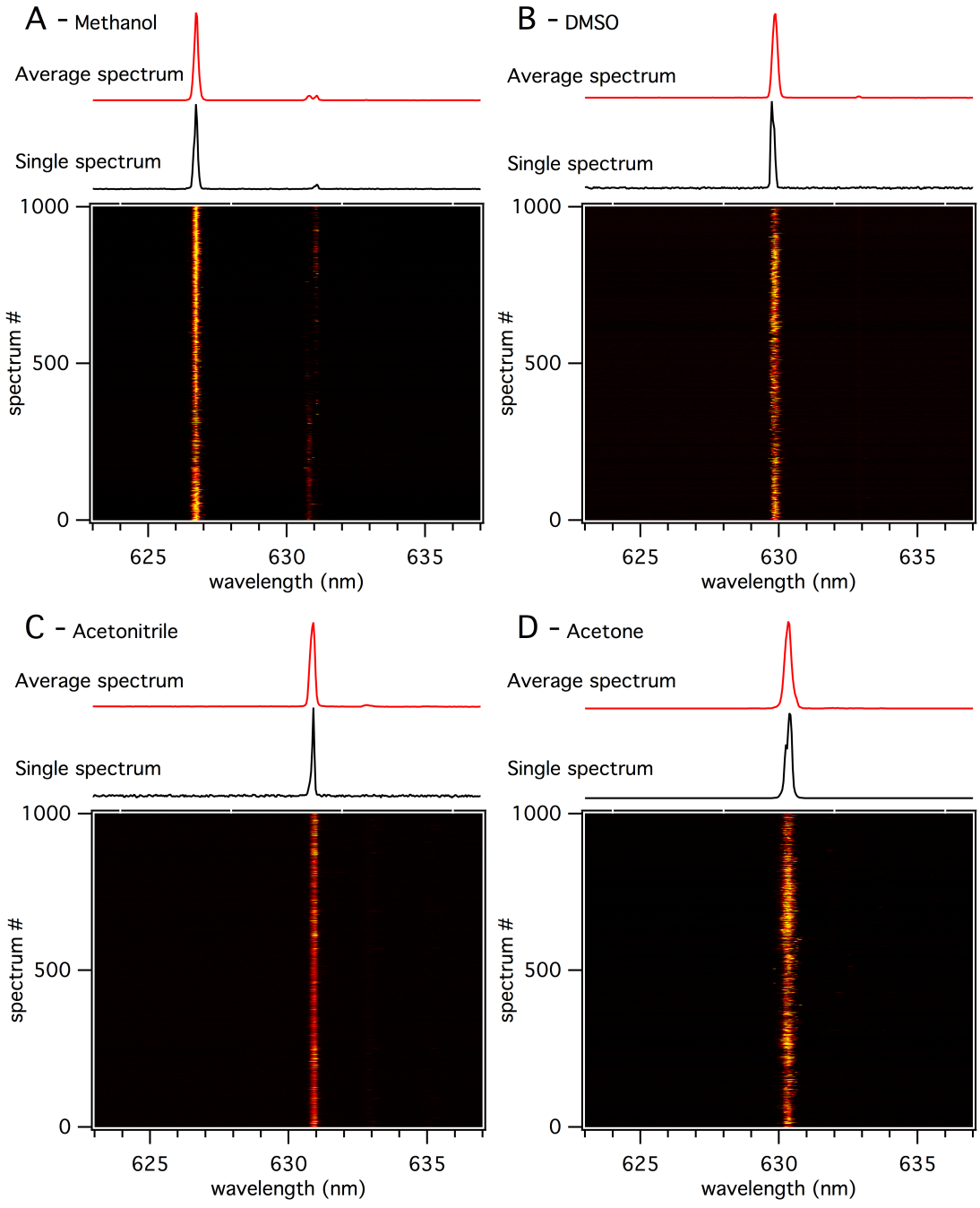

Figure 2.9: Representative Raman spectra collected from single microdroplets of methanol (**A**), DMSO (**B**), acetonitrile (**C**) and acetone (**D**). The red shows the average of 1000 consecutive single microdroplet Raman spectra, with the black showing a microdroplet Raman spectrum. The intensity plots below contain the 1000 consecutive microdroplet spectra showing the WGM positions over time.

2.3 Mie theory fitting routine

To calculate the size of the droplet, the measured whispering gallery modes (WGMs) must be assigned a mode number, l, mode order, ν, and polarization, either transverse electric (TE) or magnetic (TM). l describes the specific resonance position, while the mode order, ν, describes how far from the surface of the cavity the WGM is resonant. Greater ν values correspond to a deeper resonance. As the droplets are spherical, each WGM has an azimuthal degeneracy $(2l + 1)$. The polarisation describes whether the WGM is dependent on the light resonating within the electrical or magnetic field. Light that is resonant with the droplet's electrical field is TE, and light resonant with the magnetic field is TM [44]. The a_l term in the Q_{sca} equation describes TE resonances, while the b_l term describes TM resonances [45]. When calculating the size of a droplet the initial assignments for each experimentally measured WGM are provided as guesses.

To determine the radius and refractive index of the droplet, the Probert-Jones formulism for the scattering parameters, a_l and b_l, is used to simplify the calculation [45]. The scattering parameters are summarised into new functions p_l, q_l for the a_l term

$$p_l = \psi_l(x)\psi_l'(m_\lambda x) - m\psi_l(m_\lambda x)\psi_l'(x) \tag{2.1}$$

$$q_l = \chi_l(x)\psi_l'(m_\lambda x) - m\psi_l(m_\lambda x)\chi_l'(x) \tag{2.2}$$

providing

$$a_l = \frac{p_l}{p_l + iq_l} = \frac{p_l^2}{p_l^2 + q_l^2} - i\frac{p_l q_l}{p_l^2 + q_l^2} \tag{2.3}$$

and g_l, h_l for the b_l term.

$$g_l = m_\lambda\psi_l(x)\psi_l'(m_\lambda x) - \psi_l(m_\lambda x)\psi_l'(x) \tag{2.4}$$

$$h_l = m_\lambda\chi_l(x)\psi_l'(m_\lambda x) - \psi_l(m_\lambda x)\chi_l'(x) \tag{2.5}$$

providing

$$b_l = \frac{g_l}{g_l + ih_l} = \frac{g_l^2}{g_l^2 + h_l^2} - i\frac{g_l h_l}{g_l^2 + h_l^2} \tag{2.6}$$

Using this formulism, Probert-Jones was able to show that when the imaginary parts of the terms (q_l and h_l) headed towards zero the a_l and b_l terms would increase towards infinity, greatly increasing the magnitude of Q_{sac}. Size parameters where this phenomenon occurs results in a WGM. This allows the roots of these functions to be determined in order to find the locations of the WGMs. As there are multiple

roots for these equations, approximations of their locations assist in finding their exact positions. Approximations for the location of WGMs can found using the following function published by Lam *et al.*:

$$m_\lambda x = \nu + 2^{-1/3}\alpha_\nu \eta^{1/3} - \frac{P}{(m_\lambda^2 - 1)^{1/2}} + \frac{3}{10}2^{-2/3}\alpha_\nu^2 \eta^{-1/3} - \frac{2^{-1/3}P(m_\lambda^2 - 2P^2/3)}{(m_\lambda^2 - 1)^{3/2}}\alpha_\nu \eta^{-\frac{2}{3}} + O(\eta^{-1}) \quad (2.7)$$

Where $P = m_\lambda$ for TE resonances and P= $1/m_\lambda$ for TM, α_ν describes roots of the Airy function determined by the mode order of the resonance and η describes the position of the resonance as a series, where $\eta = l + \frac{1}{2}$ [46]. Using the approximated assignments, the approximate locations of the modes are determined using this function with the exact locations calculated subsequently using the Probert-Jones formulism. Three parameters are fit, radius, r, and the real and imaginary components of the refractive index for the Cauchy equation:

$$m_\lambda = \mathrm{A} + \frac{\mathrm{B}}{\lambda^2} \quad (2.8)$$

Using a Levenburg-Marquadt algorithm the parameters are optimised to reduce the difference between the theoretical and experimentally measured positions. Once the best fit is determined the mode number (l) assignments are iterated and the fitting procedure is repeated. This process is performed until the overall best fit is determined. From the best overall fit, the radius and refractive index the droplet are determined.

2.4 References for Chapter 2

(1) P. J. Tracey, B. S. Vaughn, B. J. Roberts, B. L. Poad and A. J. Trevitt, "Rapid profiling of laser-induced photochemistry in single microdroplets using mass spectrometry", *Analytical Chemistry*, 2014, **86**, 2895–9.

(2) P. Ben-Tzvi and W. Rone, "Microdroplet generation in gaseous and liquid environments", *Microsystems Technology*, 2010, **16**, 333–356.

(3) A. A. Castrejón-Pita, J. R. Castrejón-Pita and G. D. Martin, "A novel method to produce small droplets from large nozzles", *Review of Scientific Instruments*, 2012, **83**, 115105.

(4) A. U. Chen and O. A. Basaran, "A new method for significantly reducing drop radius without reducing nozzle radius in drop-on-demand drop production", *Physics of Fluids*, 2002, **14**, L1–L4.

(5) T. M. Liou, C. Y. Chan and K. C. Shih, "Effects of actuating waveform, ink property, and nozzle size on piezoelectrically driven inkjet droplets", *Microfluidics and Nanofluidics*, 2010, **8**, 575–586.

(6) H. Y. Gan, X. C. Shan, T. Eriksson, B. K. Lok and Y. C. Lam, "Reduction of droplet volume by controlling actuating waveforms in inkjet printing for micro-pattern formation", *Journal of Micromechanics and Microengineering*, 2009, **19**, 8.

(7) R. M. Verkouteren and J. R. Verkouteren, "Inkjet Metrology II: Resolved Effects of Ejection Frequency, Fluidic Pressure, and Droplet Number on Reproducible Drop-on-Demand Dispensing", *Langmuir*, 2011, **27**, 9644–9653.

(8) G. D. Martin, S. D. Hoath and I. M. Hutchings, "Inkjet printing - the physics of manipulating liquid jets and drops", *Journal of Physics: Conference Series*, 2008, **105**, 012001.

(9) B. Derby, "Inkjet Printing of Functional and Structural Materials: Fluid Property Requirements, Feature Stability, and Resolution", *Annual Review of Materials Research*, 2010, **40**, 395–414.

(10) L. T. Creagh and M. McDonald, "Design and performance of inkjet print heads for non-graphic-arts applications", *Mrs Bulletin*, 2003, **28**, 807–811.

(11) E. A. Roth, T. Xu, M. Das, C. Gregory, J. J. Hickman and T. Boland, "Inkjet printing for high-throughput cell patterning", *Biomaterials*, 2004, **25**, 3707–3715.

(12) T. Boland, T. Xu, B. Damon and X. Cui, "Application of inkjet printing to tissue engineering", *Biotechnology Journal*, 2006, **1**, 910–917.

(13) H. Sirringhaus, T. Kawase, R. H. Friend, T. Shimoda, M. Inbasekaran, W. Wu and E. P. Woo, "High-resolution inkjet printing of all-polymer transistor circuits", *Science*, 2000, **290**, 2123–2126.

(14) R. M. Verkouteren and J. R. Verkouteren, "Inkjet Metrology: High-Accuracy Mass Measurements of Microdroplets Produced by a Drop-on-Demand Dispenser", *Analytical Chemistry*, 2009, **81**, 8577–8584.

(15) M. Cernescu, T. Stark, E. Kalden, C. Kurz, K. Leuner, T. Deller, M. Gobel, G. P. Eckert and B. Brutschy, "Laser-Induced Liquid Bead Ion Desorption Mass Spectrometry: An Approach to Precisely Monitor the Oligomerization of the beta-Amyloid Peptide", *Analytical Chemistry*, 2012, **84**, 5276–5284.

(16) N. Morgner, H. D. Barth and B. Brutschy, "A new way to detect noncovalently bonded complexes of biomolecules from liquid micro-droplets by laser mass spectrometry", *Australian Journal of Chemistry*, 2006, **59**, 109–114.

(17) N. Morgner, T. Kleinschroth, H. D. Barth, B. Ludwig and B. Brutschy, "A novel approach to analyze membrane proteins by laser mass spectrometry: From protein subunits to the integral complex", *Journal of the American Society for Mass Spectrometry*, 2007, **18**, 1429–1438.

(18) K. Shigeta, H. Traub, U. Panne, A. Okino, L. Rottmann and N. Jakubowski, "Application of a micro-droplet generator for an ICP-sector field mass spectrometer - optimization and analytical characterization", *Journal of Analytical Atomic Spectrometry*, 2013, **28**, 646–656.

(19) K. Komatsu, T. Nirasawa, M. Hoshino-Nagasaka and J.-y. Kohno, "Mechanism of Protein Molecule Isolation by IR Laser Ablation of Droplet Beam", *The Journal of Physical Chemistry A*, 2016, **120**, 1495–1500.

(20) O. Borovinskaya, S. Gschwind, B. Hattendorf, M. Tanner and D. Gunther, "Simultaneous Mass Quantification of Nanoparticles of Different Composition in a Mixture by Microdroplet Generator-ICPTofMS", *Analytical Chemistry*, 2014, **86**, 8142–8148.

(21) R. Q. Iannone, D. Romanini, S. Kassi, H. A. J. Meijer and E. R. T. Kerstel, "A Microdrop Generator for the Calibration of a Water Vapor Isotope Ratio Spectrometer", *Journal of Atmospheric and Oceanic Technology*, 2009, **26**, 1275–1288.

(22) V. J. Cadarso, J. Perera-Nunez, A. Mendez-Vilas, L. Labajos-Broncano, M. L. Gonzalez-Martin and J. Brugger, "Microdrop generation and deposition of ionic liquids", *Journal of Materials Research*, 2014, **29**, 2100–2107.

(23) J. Y. Kohno, M. Kobayashi and T. Suzuki, "Protrusion formation during the collisional process of ethanol and water droplets: Capillary wave propagation on the water droplet", *Chemical Physics Letters*, 2013, **578**, 15–20.

(24) S. Moon, Y. G. Kim, L. S. Dong, M. Lombardi, E. Haeggstrom, R. V. Jensen, L. L. Hsiao and U. Demirci, "Drop-on-Demand Single Cell Isolation and Total RNA Analysis", *Plos One*, 2011, **6**, 10.

(25) S.-y. Zhong, L.-h. Qi, J. Luo, H.-s. Zuo, X.-h. Hou and H.-j. Li, "Effect of process parameters on copper droplet ejecting by pneumatic drop-on-demand technology", *Journal of Materials Processing Technology*, 2014, **214**, 3089–3097.

(26) J. Luo, L.-h. Qi, J.-m. Zhou, X.-h. Hou and H.-j. Li, "Modeling and characterization of metal droplets generation by using a pneumatic drop-on-demand generator", *Journal of Materials Processing Technology*, 2012, **212**, 718–726.

(27) J. Luo, L. Qi, Y. Tao, Q. Ma and C. W. Visser, "Impact-driven ejection of micro metal droplets on-demand", *International Journal of Machine Tools and Manufacture*, 2016, **106**, 67–74.

(28) J. D. Eversole, H. B. Lin, A. L. Huston, A. J. Campillo, P. T. Leung, S. Y. Liu and K. Young, "High-Precision Identification of Morphology-Dependent Resonances in Optical Processes in Microdroplets", *Journal of the Optical Society of America B*, 1993, **10**, 1955–1968.

(29) T. C. Preston and J. P. Reid, "Determining the size and refractive index of microspheres using the mode assignments from Mie resonances", *Journal of the Optical Society of America a-Optics Image Science and Vision*, 2015, **32**, Preston, Thomas C. Reid, Jonathan P., 2210–2217.

(30) J. P. Reid, H. Meresman, L. Mitchem and R. Symes, "Spectroscopic studies of the size and composition of single aerosol droplets", *International Reviews in Physical Chemistry*, 2007, **26**, 139–192.

(31) R. Symes, R. M. Sayer and J. P. Reid, "Cavity enhanced droplet spectroscopy: Principles, perspectives and prospects", *Physical Chemistry Chemical Physics*, 2004, **6**, 474–487.

(32) G. Chen, M. M. Mazumder, R. K. Chang, J. C. Swindal and W. P. Acker, "Laser diagnostics for droplet characterization: Application of morphology dependent resonances", *Progress in Energy and Combustion Science*, 1996, **22**, 163–188.

(33) C. C. Lam, P. T. Leung and K. Young, "Explicit asymptotic formulas for the positions, widths, and strengths of resonances in Mie scattering", *Journal of the Optical Society of America B*, 1992, **9**, 1585–1592.

(34) J. R. Probert-Jones, "Resonance component of backscattering by large dielectric spheres", *Journal of the Optical Society of America A*, 1984, **1**, 822–830.

(35) R. K. Chang and A. J. Campillo, *Optical processes in microcavities*, World Scientific Publishing Co. Pty. Ltd., 1996, p. 434.

(36) J. F. Owen, R. K. Chang and P. W. Barber, "Morphology-Dependent Resonances in Raman-Scattering, Fluorescence Emission, and Elastic-Scattering from Microparticles", *Aerosol Science and Technology*, 1982, **1**, 293–302.

(37) J. Popp, M. Trunk, M. Lankers, I. Hartmann, K. Schaschek and W. Kiefer, "Observability of morphology-dependent output resonances in the Raman spectra of optically levitated microdroplets", *Journal of Raman Spectroscopy*, 1997, **28**, 531–536.

(38) R. Symes and J. P. Reid, "Determining the composition of aqueous microdroplets with broad-band cavity enhanced Raman scattering", *Physical Chemistry Chemical Physics*, 2006, **8**, 293–302.

(39) A. J. Trevitt, P. J. Wearne and E. J. Bieske, "Coalescence of levitated polystyrene microspheres", *Journal of Aerosol Science*, 2009, **40**, 431–438.

(40) R. M. Sayer, R. D. B. Gatherer, R. J. J. Gilham and J. P. Reid, "Determination and validation of water droplet size distributions probed by cavity enhanced Raman scattering", *Physical Chemistry Chemical Physics*, 2003, **5**, 3732–3739.

(41) R. D. B. Gatherer, R. M. Sayer and J. P. Reid, "An optical method for determining size distributions of water droplets", *Chemical Physics Letters*, 2002, **366**, 34–41.

(42) B. S. Vaughn, P. J. Tracey and A. J. Trevitt, "Laser-initiated iodine radical chemistry in single microdroplets", *Chemical Physics Letters*, 2012, **551**, 134–138.

(43) R. J. Hopkins, R. Symes, R. M. Sayer and J. P. Reid, "Determination of the size and composition of multicomponent ethanol/water droplets by cavity-enhanced Raman scattering", *Chemical Physics Letters*, 2003, **380**, 665–672.

(44) R. Symes, R. M. Sayer and J. P. Reid, "Cavity enhanced droplet spectroscopy: Principles, perspectives and prospects", *Physical Chemistry Chemical Physics*, 2004, **6**, 474–487.

(45) J. R. Probert-Jones, "Resonance component of backscattering by large dielectric spheres", *Journal of the Optical Society of America A*, 1984, **1**, 822–830.

(46) C. C. Lam, P. T. Leung and K. Young, "Explicit asymptotic formulas for the positions, widths, and strengths of resonances in Mie scattering", *Journal of the Optical Society of America B*, 1992, **9**, 1585–1592.

Chapter 3

Laser-initiated iodine radical chemistry

This chapter has been published in its current form as the following peer-reviewed publication:

Bartholomew S. Vaughn, Phillip J. Tracey and Adam J. Trevitt, Laser-initiated iodine radical chemistry in single microdroplets, *Chemical Physics Letters* **551**, 134 - 138 (2012).

Reproduced as Appendix C

Author contributions
Bartholomew S. Vaughn performed all the experiments with the assistance of Phillip J. Tracey. Bartholomew S. Vaughn and Phillip J. Tracey prepared the manuscript which was edited by Adam J. Trevitt. Adam J. Trevitt is the corresponding author.

Certification
I, Assoc. Prof. Adam J. Trevitt, as Bartholomew S. Vaughn's supervisor and the principal investigator on this project, agree with and certify the author contributions described above.

Assoc. Prof. Adam. J. Trevitt

16/11/16

Date

3.1 Abstract

Iodine radical reactions in single free-falling microdroplets of iododododecane, initiated using UV laser photolysis, are probed using Raman spectroscopy. Stimulated Raman spectra, with 532 nm laser excitation, are recorded at varying time delays from the UV pulse. I atom recombination reactions lead to I_2 that changes the optical properties of the microdroplet ultimately quenching the Raman signal. This quenching is observed over ∼10 ns, which is about the time resolution of the two-laser experiment. Although the kinetics are too rapid to be measured in current laser configuration, it demonstrates that radical kinetics can be followed in single microdroplets.

3.2 Introduction

Aerosol chemistry affects a wide range of environments [1–5], from the burning fuel spray in a diesel combustion engine to atmospheric heterogeneous processes. In the latter case, aerosol chemistry can impact regional and global climates and has been shown to play a significant role in the chemistry implicated in ozone layer depletion and acid rain [6, 7]. Our understanding of these processes, and our ability to make accurate predictions, relies on accurate models constructed from validated data. Laboratory experiments that probe the chemical and physical properties of aerosols play a vital role in providing these details.

Studying the physical and chemical properties of aerosols presents significant challenges. Many properties of aerosols are inferred from ensemble-averaged measurements of bulk aerosol systems. These ensemble measurements can obscure variations in size and composition of the individual aerosol particles – finer processes resulting from their large surface-to-volume ratio may go unnoticed. To develop accurate models, and improve our understanding of aerosol chemistry, new experimental techniques are required to probe chemistry at the single particle/droplet level.

Single liquid droplets have been isolated for study using techniques including optical trapping [8] and electrodynamic trapping [9–11], allowing for interrogation of particle properties such as size [12, 13], composition [12, 14, 15], and IR absorption [16, 17] using laser based techniques. Recently, prominent advances employ laser-based spectroscopic methods exploiting microcavity effects within small microdroplets [8, 12–15, 18, 19]. Radical + aerosol reactions have been studied in flow-tube photolysis experiments, for example coupled to synchrotron photoionization mass spectrometry [20]. There are several studies that have investigated radical chemistry in real-time on the single droplet level. Using Raman

spectroscopy, radical reactions occurring within single microdroplets have been followed over time periods of minutes to hours [21–25]. Esen et al. employed Raman spectroscopy to observe real-time photoinitiated polymerization occurring in single microdroplets [25]. In that study, polymerisation was initiated in a single optically trapped microdroplet using UV radiation from a HgAr lamp. The Raman spectrum from the droplet was monitored with temporal resolution of ∼1 s to provide chemical information as the polymerization reaction evolved. King *et al.* also demonstrated the use of Raman spectroscopy to monitor chemical change within a single microdroplet over time, studying the reaction of ozone with seawater and oleic acid in optically tweezed droplets [22].

The desire to measure radical reaction rates within single droplets provides motivation for new experimental techniques. In this study we report the combination of a drop-on-demand microdroplet generator, providing a highly reproducible droplet stream, coupled with single laser shot Raman spectroscopy. By initiating photochemistry with a UV laser we can monitor radical reactions that change the optical properties of the microdroplet on the tens of nanosecond timescale.

3.3 Experimental

The experimental apparatus for performing single-microdroplet Raman spectroscopy has three key aspects: the drop-on-demand microdroplet generator, two pulsed-lasers and a spectrometer fitted with a CCD detector. Figure 3.1 illustrates the configuration of the experimental setup. 1-Iodododecane (Sigma Aldrich, 98%) microdroplets are produced at room temperature and pressure using a commercial drop-on-demand droplet generator (Microdrop Technologies GmbH) but with our own external electronics. A square-wave pulse from a signal generator (Agilent 33521A) is then amplified (FLC Electronics A400) to provide the drive pulse for the droplet generator. The pulse, with typical operating parameters of V_{0-P} = 100 V and pulsewidth = 40 μs, is applied across a piezoelectric crystal within the droplet head that compresses the liquid-filled capillary. This expels a portion of liquid out of the capillary nozzle that detaches to form a microdroplet. The droplet generator capillary has an internal diameter of 50 μm, typically producing iodododecane droplets of ∼45 μm diameter under these operating conditions, and is operated at a frequency of 50 Hz.

The microdroplets fall and traverse a continuous-wave diode laser (λ = 635 nm) that is directed perpendicular to the microdroplet path at 1 cm distance from the capillary exit. The droplet velocity is approximately 1.9 m/s. The light scattered off the microdroplets as they pass through the diode laser beam is detected by a photodiode and this signal is used to trigger a digital delay generator (SRS

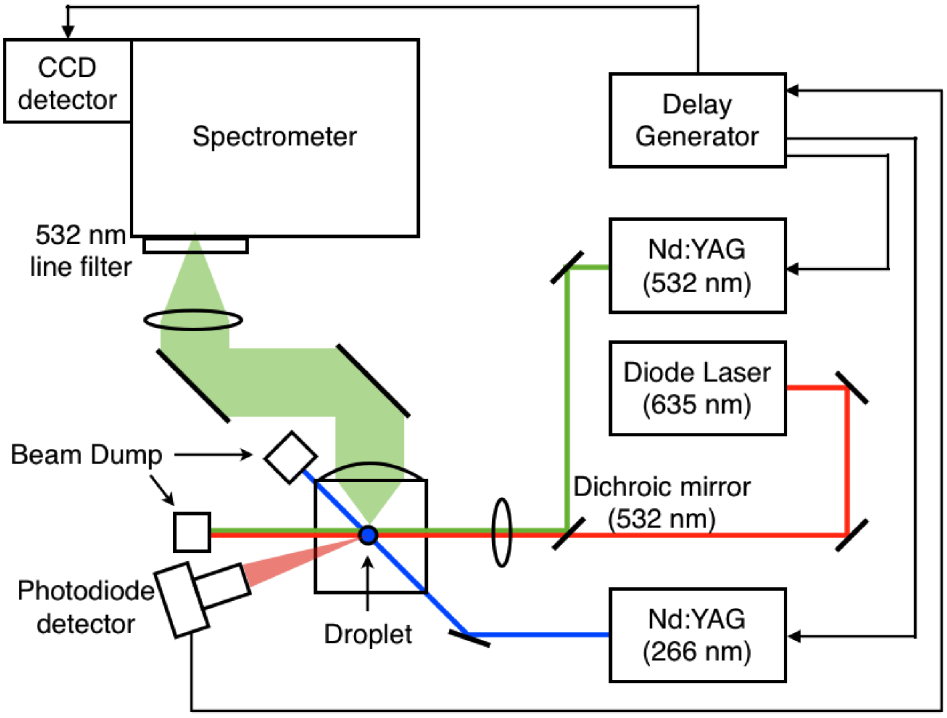

Figure 3.1: Schematic illustration of the instrument configuration for performing time-resolved single microdroplet Raman spectroscopy.

DG645) that controls the timing of two pulsed lasers and the CCD detector of the spectrometer.

At a delay of typically 300 μs after the photodiode trigger pulse, the microdroplet is irradiated by a single ~5 ns Nd:YAG (MiniLite, Continuum) 532 nm laser pulse that serves as the Raman excitation laser. This laser is focussed by a 100 mm lens to a spot size estimated at about 20 μm. The laser energy is approximately 0.2 mJ pulse^{-1}. The Raman excitation laser is operated at 10 Hz, so the laser experiments are actually performed on every fifth droplet – the droplet generator operates a 50 Hz – and the other droplets are ignored. A portion of the scattered light originating from the 532 nm pulse, containing both elastically and inelastically scattered (Raman) photons, is collected by a 2-inch diameter pickup lens (f/1.2) and directed into a spectrometer (Shamrock 500, Andor), via two mirrors, and focused using a lens selected to best-match the NA of the spectrometer (f/6). A 532 nm notch filter (Semrock) is placed in front of the spectrometer entrance slit to reject elastically scattered photons. The remaining Stokes Raman scattered light is dispersed over a cooled (-70 °C) 1024 × 256 pixel open-electrode CCD detector (Newton, Andor) via a grating of 600 groove/mm. The image is processed using custom LabVIEW software to yield a Raman spectrum for the one droplet. Using this scheme, single-shot microdroplet Raman spectra are obtained without fail for thousands of droplets.

To initiate photochemistry within the droplets, a second pulsed Nd:YAG laser (MiniLite, Continuum) $\lambda = 266$ nm, irradiates the droplet prior to the 532 nm Raman excitation laser. By precisely controlling the delay in steps of 1 - 5 ns between the 266 nm and 532 nm laser pulses, a change in the Raman signal intensity is observed over time providing kinetic detail. The UV laser beam is attenuated using a series of neutral density filters. In this study, the Raman band corresponding to the iodoalkane C–H stretch is integrated to yield a Raman signal intensity versus laser delay plot. In order to reduce the effect of systematic drifts, ten Raman spectra are acquired at each time-delay before the delay is stepped and the entire delay range is scanned ∼20 times to build the final data. Ultimately, ∼200 spectra are averaged at each delay.

3.4 Results and Discussion

A Raman spectrum of iodododecane acquired from a bulk sample (1 mm quartz cuvette) using this experimental setup at 532 nm excitation is shown in Figure 3.2(a) and matches the 1-iodododecane FT-Raman spectrum supplied by the vendor (Sigma-Aldrich). The large signal centred on ∼2900 cm^{-1} is the aliphatic C–H stretch band. The Raman spectrum obtained from single 45 μm diameter microdroplets of 1-iodododecane is shown in Figure 3.2(b), is averaged over 500 single shot droplet spectra. It is worth noting that the corresponding microdroplet volume is ∼50 pL. Due to optical feedback processes within the microdroplet, often referred to as whispering gallery modes or morphology dependent resonances (MDRs) [18, 26], stimulated Raman scattering (SRS) can occur at wavelengths commensurate with MDRs that fall within a spontaneous Raman band. This is evident in the single microdroplet spectrum (Figure 3.2(b)) where the C–H band (∼2900 cm^{-1}) is modulated by sharp, intense SRS peaks. Other less intense Raman signals over the 500-2000 cm^{-1} region, that are clearly noticeable in the bulk Raman spectrum, apparently do not meet SRS threshold conditions and are absent in the scale of Figure 3.2(b). These bands arise from the C-I stretch (∼500 cm^{-1}), long-chain band (∼600 cm^{-1}), -CH3 bend (∼1375 cm^{-1}) and -CH2- bend (∼1465 cm^{-1}). However, on closer inspection these Raman bands are observable at ×5000 magnification. These are spontaneous Raman bands that do not suffer modulation from the microdroplet cavity modes and likely arise from direct scattering off the front surface of the microdroplet or signal from the droplet bulk that do not surpass the threshold for SRS. In this study, we focus on the C–H Raman band. SRS is a nonlinear optical process, and the relationship between the increasing presence of an absorbing species and the SRS signal may complicate a direct linear analysis. An internal referencing approach, such as that described in Ref [27], may surmount this

problem. The 1-iodododecane microdroplets are largely transparent over the 400-

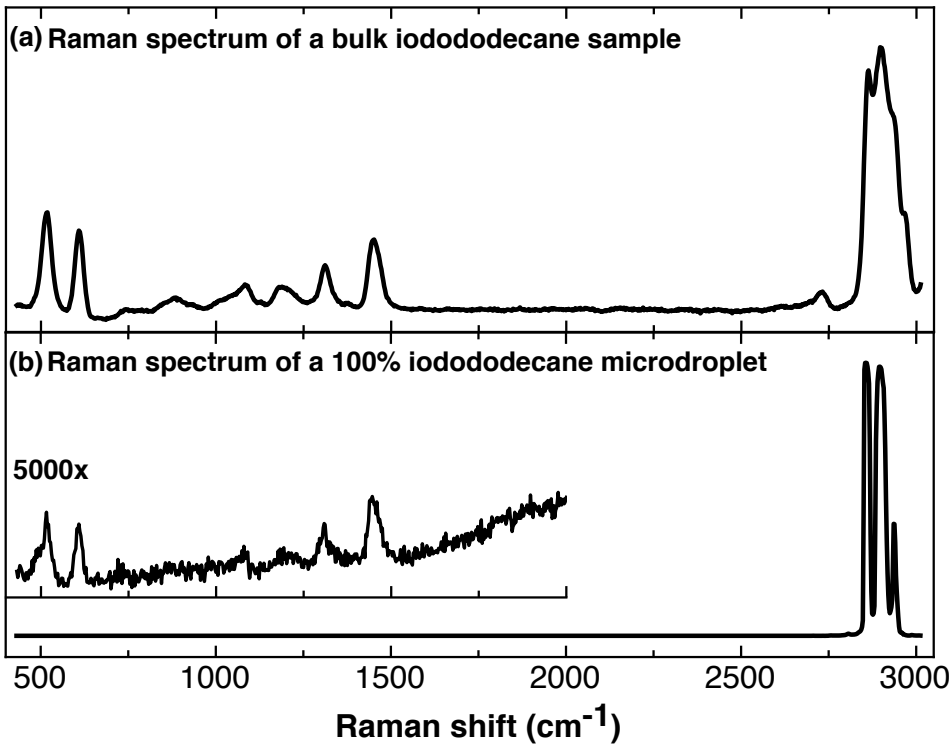

Figure 3.2: Raman spectra obtained for (a) a bulk iodododecane sample and (b) single iodododecane microdroplets.

700 nm range. Photolysis of 1-iodododecane at 266 nm produces alkyl and atomic iodine radicals:

$$CH_3(CH_2)_{10}CH_2I + h\nu_{266\ nm} \rightarrow CH_3(CH_2)_{10}CH_2^{\cdot} + I^{\cdot} \tag{3.1}$$

Once liberated, the iodine radicals can then readily undergo recombination forming molecular iodine (I_2) that has a broad absorption peak centred at ∼480 nm giving it a red/brown colour. Generating I_2 in this way can easily be observed in a quartz cuvette containing iodododecane and irradiating the sample with several 266 nm laser shots (4 mJ/pulse) and observing the resulting red/brown stain. A conventional UV-Vis spectrum confirms the formation of I_2. The fate of the alkyl radicals is not clear, some radical-induced polymerisation may occur. In the case of single microdroplets, the laser-initiated photolysis releases I radicals that recombine to produce I_2; this changes the optical properties of the microdroplet. As the I_2 concentration grows the droplet becomes increasingly opaque and it is found that this supresses and can ultimately quench the SRS signal. By increasing the time delay between photolysis and Raman probe lasers the intensity of the C–H Raman signal is observed to decrease over time, as represented schematically in Figure 3.3. This time-dependent quenching effect can be used to infer the progress of the radical

recombination reaction leading to I_2 formation. The presence of the I_2 will absorb a portion of the 532 nm Raman excitation laser as well as absorbing to some extent at the 630 nm C–H Raman shift region. By integrating the Raman band, a value for

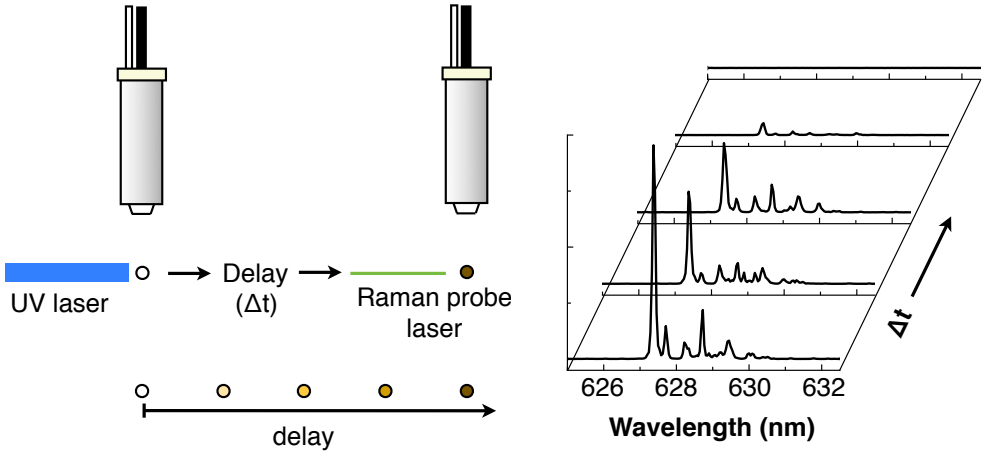

Figure 3.3: Schematic representation of how Raman spectra are obtained as the delay between the UV laser and Raman probe laser is increased the droplet becomes increasingly opaque. The C–H Raman band is quenched as the concentration of I_2 increases.

the intensity of Raman signal is obtained for a given laser delay. Figure 3.4 shows the time dependence of the Raman signal as a function of the two-laser delay of iododododecane microdroplets for five different UV laser fluences spanning 0.47 mJ cm^{-2} to 0.02 mJ cm^{-2} (a - e). The negative time delays correspond to when the 532 nm Raman excitation laser is pulsed before the UV laser. To within an uncertainty of $\pm$ 5 ns, zero time delay corresponds to the laser pulses irradiating the droplet at the same time. Traces (a) and (b), corresponding to 0.47 mJ cm^{-2} and 0.38 mJ cm^{-2} UV laser fluence, show the Raman signal quenching to zero over $\sim$10 ns. A reduction in the UV laser fluence to 0.13 mJ cm^{-2} (c) results also in a depletion that does not completely quench the Raman signal, with the final signal reaching a constant value of $\sim$16% of the original value after $\sim$10 ns. Traces corresponding to UV laser fluences of 0.05 mJ cm^{-2} (d) and 0.02 mJ cm^{-2} (e) show depletions to $\sim$65% and 83%, respectively. Figure 3.4(f) shows the same experiment, at 1 mJ cm^{-2} UV laser fluence, but with pure dodecane droplets, that shows no measurable depletion in the C–H Raman signal as a result of UV laser irradiation. This supports the idea that the iodine chemistry is responsible for the Raman suppression in the iododododecane microdroplets. Also plotted in traces (a) – (e) are Gaussian integrals that allow the temporal processes to be fitted and compared. Other than the extent of the quenching, these fits show a shallowing in the inflection of the profiles as the UV laser fluence is decreased. Traces (a) and (b) are fitted to corresponding Gaussian fwhm values of 3.5 $\pm$ 0.6 ns and 4 $\pm$ 1 ns, respectively. But as these signals

are completely quenched it is not clear if the processes leading to the quenching, e.g. the formation of I_2, continues on. Interestingly, trace (c) shows that the process that leads to the suppression of the Raman signal is complete within this ∼10 ns time window, as the non-zero Raman intensity reaches a constant value at longer delays. Trace (c) is fitted to corresponding Gaussian fwhm of 6 ± 1 ns. The time resolution expected from our lasers, however, (the manufacturer suggests pulse widths of 3-5 ns for both harmonics so we assume fwhm of 5 ns for the 532 nm and 3 ns for the 266 nm) corresponds to a convoluted Gaussian fwhm of about 8 ns, neglecting any electronic jitter. These fast-resolved processes are possibly due to the non-linear temporal response of the single laser SRS signal. Traces (d) and (e) are fitted with Gaussian fwhm values of 7 ± 5 ns and 9 ± 9 ns with the uncertainties notably increasing sharply. In the end, all these processes are occurring very close to the temporal resolution of the experimental arrangement so it is difficult to extract any quantitative information. Shorter laser pulse widths, however, may be more revealing. In order to understand the chemical processes, we can estimate the amount of I radicals that could be forming from the UV laser photolysis in attempt to account for these kinetics. Radical recombination follows the second order rate law:

$$\mathrm{I} + \mathrm{I} \rightarrow \mathrm{I_2} \tag{3.2}$$

$$\frac{d[\mathrm{I_2}]}{dt} = k[\mathrm{I}]^2 \tag{3.3}$$

To obtain an estimate for the reaction rate we might expect, we can perform simple but insightful calculations by making some assumptions. With knowledge of the laser photon density and droplet size, we can estimate the number of UV photons hitting the droplet. For a photon fluence of 0.39 mJ cm^{-2} and a droplet of 45 μm diameter, this corresponds to $\sim 1.8 \times 10^{10}$ photons. If we assume each of these photons yields an iodine radical, i.e. an I atom quantum yield of 1, the upper limit for I atom radicals is found, diluted over the volume of the droplet, to be $\sim 6 \times 10^{-4}$ mol L^{-1}. From this initial I atom concentration we can estimate the half-life of the reaction assuming the reaction follows a simple second order rate law, bearing in mind that the radical-radical reaction is limited by I atom diffusion and, at this point, that the concentration is calculated considering the entire volume of the droplet. The reaction half-life is given by:

$$t_{1/2} = \frac{1}{k[\mathrm{I}]_0} \tag{3.4}$$

where k is the second order rate coefficient and $[\mathrm{I}]_0$ is the initial I atom concentration. For a barrierless second-order radical recombination reaction in solution, k is dominated by the rate of diffusion of the reaction species, allowing it to be estimated

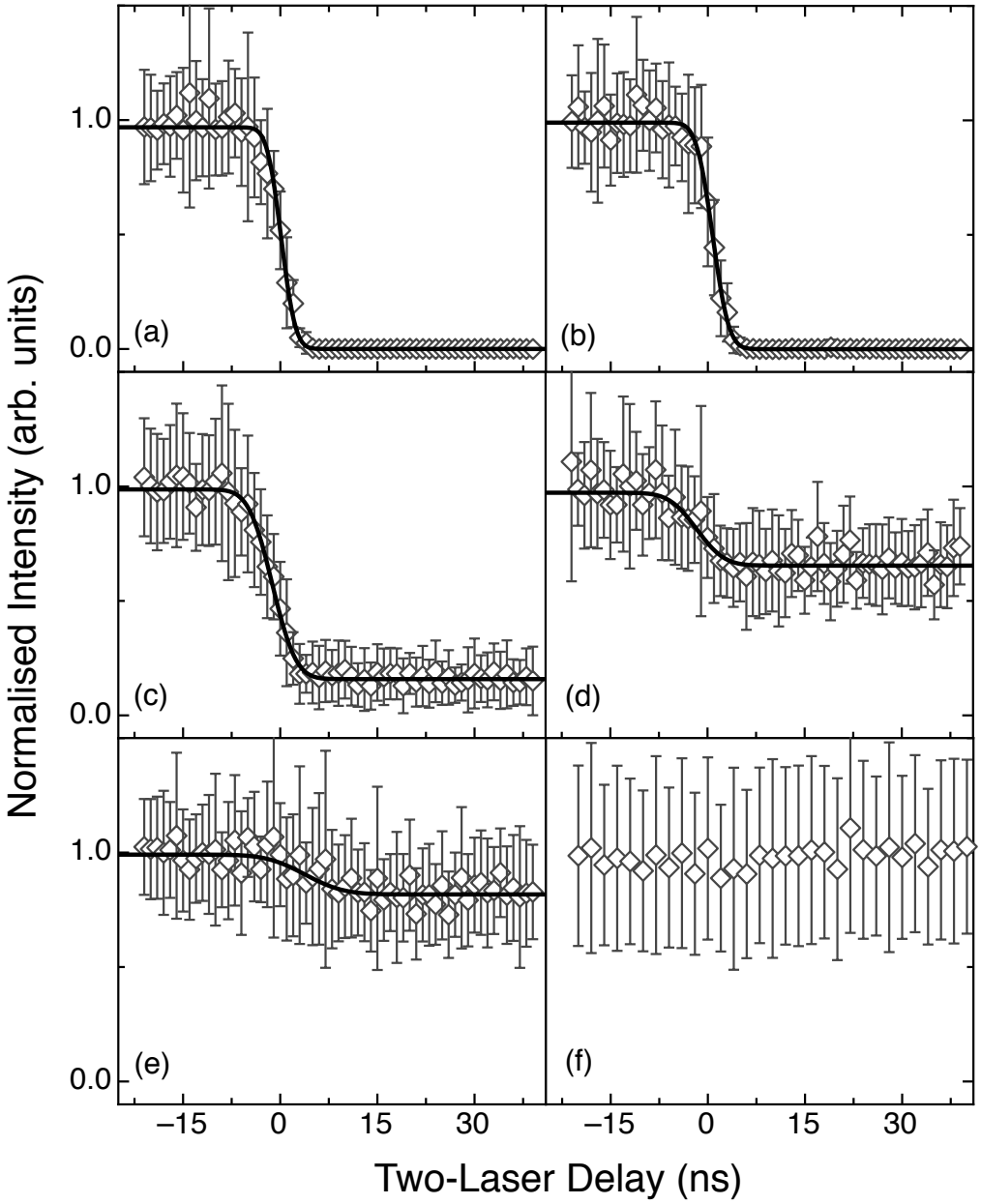

Figure 3.4: Normalised Raman signal intensity from iodododecane microdroplets as a function of the delay between UV and Raman probe lasers for different UV laser fluences; (a) 0.47 mJ cm^{-2}, (b) 0.38 mJ cm^{-2}, (c) 0.13 mJ cm^{-2}, (d) 0.05 mJ cm^{-2}, (e) 0.02 mJ cm^{-2}. A trace for pure dodecane is shown (f) at 1.0. mJ cm^{-2} UV laser fluence.

by:

$$k = 4\pi D_c R_0 \tag{3.5}$$

where D_c is the diffusion coefficient of the reactant and R_0 is the effective reaction distance. Using values for iodine atoms in dodecane from the literature at T = 298 K [28], $D_c = 2.60\times10^{-9}\ m^2s^{-1}$ and R_0= 0.38 nm, k can calculated to be $7.5\times10^9\ L^{-1}s^{-1}$, resulting in a reaction half-life, $t_{1/2}$= ∼200 ns. This value is an order of magnitude slower than the resolution-limited reaction times we have

measured; further analysis is required to explain our observations.

Fast reaction rates may be accounted for by a high absorption cross section of 1-iodododecane at 266 nm and the diffusion rate of the iodine atoms that are formed. If a large proportion of photons are absorbed close to the droplet surface, within the first tens to hundreds of nanometres, a localised, high concentration close to the droplet surface is possible. If the I atom concentration in this region is higher than that previously calculated, using the entire volume of the droplet, it will increase the reaction rate and hence reduce the estimated reaction half-life.

If we consider the diffusion rate of the I atoms again we can calculate the distance they may travel in the 20 ns between the UV laser hitting the droplet and the acquisition of the Raman spectrum. A simple estimate for the rms diffusion of some species over a distance, X, is given by[29]:

$$\langle X^2 \rangle^{1/2} = (q_i D_c t)^{1/2} \tag{3.6}$$

Where t is time and q_i is a numerical constant that depends on dimensionality, with $q_i = 6$ for a three dimensional case. Solving for X, the iodine radicals will have moved an average of 18 nm over a period of 20 ns. In a droplet with a radius of 22.5 μm this is a short distance, and supports the theory that there will be a significant I_2 concentration build up near the surface of the droplet, as neither the I radicals nor the I_2 will diffuse a significant distance in the timeframe of our observations.

If it is simply assumed that >99% of photons are absorbed, regardless of angle of incidence, within the first 100 nm of the droplet's surface this will produce a thin hemispherical shell of high I atom concentration on one side of the droplet corresponding to a volume of 0.3 pL. Correspondingly, a local I atom concentration of ∼0.1 M is generated. Using this concentration the resultant $t_{1/2}$ is ∼1 ns, below the resolution possible with our ns lasers. The end result, on the tens of nanosecond timescale, is an iodododecane droplet with a thin skin of I_2 concentration that has yet to diffuse and disperse over the entire droplet.

Despite the limitations of time resolution presently faced, the technique shows promise for studying radical processes in aerosols, particularly processes occurring at the droplet surface. It is important to note that the SRS signal observed is largely the result of the microdroplet MDRs. The electric field intensity is confined very close to the droplet surface with peak intensity at a radial coordinate of ≥90% of the droplet radius, depending on the mode number and mode order of the resonance [18]. The spectra presented in this paper are dominated by low-order resonances with mode numbers around 200-300 expected, and therefore confinement of electric field intensities in the outermost ∼10% of the droplet. This electric field localisation results in an enhancement of the Raman signal at resonant wavelengths and also

means the spectroscopic information obtained is specific to the outer volume of the droplet. This may allow for spectroscopic study of processes occurring specifically at, or close to, the droplet surface. This is currently under pursuit.

3.5 Conclusions

The measurements presented here demonstrate for the first time the ability of single laser shot Raman spectroscopy to observe a qualitative change in the concentration of a radical species in a microdroplet. I atom recombination reactions initiated by UV laser photolysis of iododododecane are found to proceed at rates faster than ∼10 ns which is the time resolution of the experiment. Estimates show that high local concentrations of radicals are likely generated from the UV laser affording sub-nanosecond recombination rates. Despite the limited time resolution, this demonstrates that radical reactions can be followed in single liquid microdroplets with nanosecond time resolution.

3.6 Acknowledgements

The authors gratefully acknowledge funding and support from the Australian Research Council (DP1094135) and the University of Wollongong.

3.7 References for Chapter 3

(1) R. Vogt, R. Sander, R. Von Glasow and P. J. Crutzen, "Iodine chemistry and its role in halogen activation and ozone loss in the marine boundary layer: A model study", *Journal of Atmospheric Chemistry*, 1999, **32**, 375–395.

(2) I. J. George and J. P. D. Abbatt, "Heterogeneous oxidation of atmospheric aerosol particles by gas-phase radicals", *Nature Chemistry*, 2010, **2**, 713–722.

(3) R. M. B. O. Duarte and A. C. Duarte, "A critical review of advanced analytical techniques for water-soluble organic matter from atmospheric aerosols", *Tractrends in Analytical Chemistry*, 2011, **30**, 1659–1671.

(4) D. Baumgardner, J. L. Brenguier, A. Bucholtz, H. Coe, P. DeMott, T. J. Garrett, J. F. Gayet, M. Hermann, A. Heymsfield, A. Korolev, M. Kraemer, A. Petzold, W. Strapp, P. Pilewskie, J. Taylor, C. Twohy, M. Wendisch, W. Bachalo and P. Chuang, "Airborne instruments to measure atmospheric aerosol particles, clouds and radiation: A cook's tour of mature and emerging technology", *Atmospheric Research*, 2011, **102**, 10–29.

(5) E. N. Korzhova, O. V. Kuznetsova, A. N. Smagunova and M. V. Stavitskaya, "Determination of inorganic pollutants in atmospheric aerosols", *Journal of Analytical Chemistry*, 2011, **66**, 222–240.

(6) J. P. Reid and R. M. Sayer, "Heterogeneous atmospheric aerosol chemistry: laboratory studies of chemistry on water droplets", *Chemical Society Reviews*, 2003, **32**, 70–79.

(7) M. Kanakidou, J. H. Seinfeld, S. N. Pandis, I. Barnes, F. J. Dentener, M. C. Facchini, R. Van Dingenen, B. Ervens, A. Nenes, C. J. Nielsen, E. Swietlicki, J. P. Putaud, Y. Balkanski, S. Fuzzi, J. Horth, G. K. Moortgat, R. Winterhalter, C. E. L. Myhre, K. Tsigaridis, E. Vignati, E. G. Stephanou and J. Wilson, "Organic aerosol and global climate modelling: a review", *Atmospheric Chemistry and Physics*, 2005, **5**, 1053–1123.

(8) L. Mitchem and J. P. Reid, "Optical manipulation and characterisation of aerosol particles using a single-beam gradient force optical trap", *Chemical Society Reviews*, 2008, **37**, 756–769.

(9) M. F. Buehler, T. M. Allen and E. J. Davis, "Microparticle Raman-spectroscopy of multicomponent aerosols", *Journal of Colloid and interface Science*, 1991, **146**, 79–89.

(10) E. J. Davis, "Electrodynamic balance stability characteristics and applications to the study of aerocolloidal particles", *Langmuir*, 1985, **1**, 379–387.

(11) A. J. Trevitt, P. J. Wearne and E. J. Bieske, "Calibration of a quadrupole ion trap for particle mass spectrometry", *International Journal of Mass Spectrometry*, 2007, **262**, 241–246.

(12) J. Buajarern, L. Mitchem and J. P. Reid, "Characterizing multiphase Organic/Inorganic/Aqueous aerosol droplets", *Journal of Physical Chemistry A*, 2007, **111**, 9054–9061.

(13) A. E. Carruthers, J. P. Reid and A. J. Orr-Ewing, "Longitudinal optical trapping and sizing of aerosol droplets", *Optics Express*, 2010, **18**, 14238–14244.

(14) H. Meresman, A. J. Hudson and J. P. Reid, "Spectroscopic characterization of aqueous microdroplets containing inorganic salts", *Analyst*, 2011, **136**, 3487–3495.

(15) R. Symes and J. P. Reid, "Determining the composition of aqueous microdroplets with broad-band cavity enhanced Raman scattering", *Physical Chemistry Chemical Physics*, 2006, **8**, 293–302.

(16) S. Arnold and A. B. Pluchino, "Infrared-spectrum of a single aerosol-particle by photothermal modulation of structure resonances", *Applied Optics*, 1982, **21**, 4194–4196.

(17) S. Arnold, E. K. Murphy and G. Sageev, "Aerosol-Particle Molecular-Spectroscopy", *Applied Optics*, 1985, **24**, 1048–1053.

(18) R. Symes, R. M. Sayer and J. P. Reid, "Cavity enhanced droplet spectroscopy: Principles, perspectives and prospects", *Physical Chemistry Chemical Physics*, 2004, **6**, 474–487.

(19) J. P. Reid, H. Meresman, L. Mitchem and R. Symes, "Spectroscopic studies of the size and composition of single aerosol droplets", *International Reviews in physical Chemistry*, 2007, **26**, 139–192.

(20) C.-L. Liu, J. D. Smith, D. L. Che, M. Ahmed, S. Leone and K. Wilson, "The direct observation of secondary radical chain chemistry in the heterogeneous reaction of chlorine atoms with submicron squalane droplets", *Physical Chemistry Chemical Physics*, 2011, **13**, 8993–9007.

(21) M. P. Houlne, C. M. Sjostrom, R. H. Uibel, J. A. Kleimeyer and J. M. Harris, "Confocal Raman microscopy for monitoring chemical reactions on single optically trapped, solid-phase support particles", *Analytical Chemistry*, 2002, **74**, 4311–4319.

(22) M. D. King, K. C. Thompson and A. D. Ward, "Laser tweezers Raman study of optically trapped aerosol droplets of Seawater and oleic acid reacting with ozone: Implications for cloud-droplet properties", *Journal of the American Chemical Society*, 2004, **126**, 16710–16711.

(23) J. Musick, J. Popp, M. Trunk and W. Kiefer, "Investigations of radical polymerization and copolymerization reactions in optically levitated microdroplets by simultaneous Raman spectroscopy, Mie scattering, and radiation pressure measurements", *Applied Spectroscopy*, 1998, **52**, 692–701.

(24) J. F. Widmann, C. L. Aardahl and E. J. Davis, "Microparticle Raman spectroscopy", *Trac-trends in Analytical Chemistry*, 1998, **17**, 339–345.

(25) C. Esen, T. Kaiser and G. Schweiger, "Raman investigation of photopolymerization reactions of single optically levitated microparticles", *Applied Spectroscopy*, 1996, **50**, 823–828.

(26) T. R. Lettieri and R. E. Preston, "Observation of sharp resonances in the spontaneous Raman-spectrum of a single optically levitated microdroplet", *Optics Communications*, 1985, **54**, 349–352.

(27) W. P. Acker, A. Serpenguzel, R. K. Chang and S. C. Hill, "Stimulated Raman-scattering of fuel droplets - Chemical concentration and size determination", *Applied Physics B - Photophysics and Laser Chemistry*, 1990, **51**, 9–16.

(28) J. A. Laverne and L. Wojnarovits, "Rates of alkyl radical-radical, alkyl radical-iodine, and iodine atom-atom reactions in normal-alkanes and cycloalkanes", *Journal of physical Chemistry*, 1994, **98**, 12635–12640.

(29) P. Atkins and J. de Paula, *Physical Chemistry, Eighth Edition*, 2006.

Chapter 4

Hydroxylation of terephthalate

4.1 Introduction

As interest in the fundamental dynamics of aerosol particles increases, the demand for techniques to probe these processes also grows with an emphasis on controlled laboratory experiments [1–3]. Current lab-based techniques focus on isolation of single aerosol particles/droplets to investigate long timescale processes (>1 ms) such as organic oxidation dynamics [4], evaporation and growth dynamics [5] and mass accommodation and transfer [6]. While these techniques provide excellent control over the particle and surrounding environment they lack the ability to perform measurements on the microsecond timescale [1]. This has left a void in the knowledge-base pertaining to short timescale processes (<100 μs), such as those involving photoinitiated and radical chemistry. As such, new techniques with the capabilities to investigate these fast processes within single aerosol particles are required to redress this knowledge gap.

Previously, microdroplets utilised in collision experiments exhibited enhanced mixing rates [7, 8], but these studies concluded that inconsistencies in the coalesced microdroplet size and shape limited the accuracy of the measurement [7, 8]. These studies emphasised the importance of microdroplet stability when performing kinetic measurements in single microdroplets as minor changes in shape and size can greatly impact optical measurements.

As shown in Chapter 3, iodine recombination kinetics are tracked in single microdroplets and were found to occur faster than the temporal resolution provided by the two nanosecond-pulse lasers (∼7 ns). The study demonstrated that the UV irradiation of droplets of 1-iodododecane resulted in C–I bond photolysis generating iodine radicals ($I^{\cdot}$), which recombined to form molecular iodine (I_2). The formation of I_2 was inferred by monitoring the quenching of the cavity-enhanced Raman signal, resulting from the C-H stretching band of 1-iodododecane, as the I_2 efficiently

absorbs the Raman excitation laser (λ = 532 nm). This study demonstrated that laser-initiated chemical processes are observable in free-falling single microdroplets using spectroscopic detection, however in this case only limited kinetic and molecular details were extracted. To further expand on this idea, and determine if chemical kinetics measurements in single microdroplets are possible, a fluorescence strategy is now investigated. Furthermore, a radical addition reaction is investigated rather than a (second order) radical recombination.

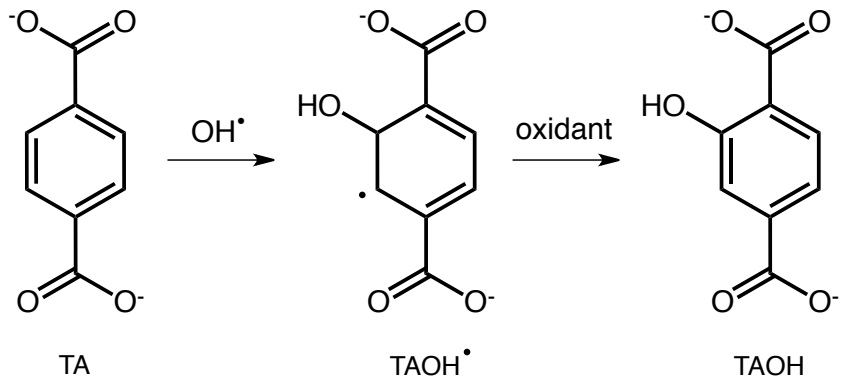

Figure 4.1: The non-fluorescent terephthalate (TA) anion reacts with hydroxyl radicals forming 1,4-dicarboxy-2-hydroxycyclohexadienyl radical (TAOH$^{\cdot}$) that after further reactions forms the fluorescent product, hydroxyterephthalate (TAOH).

The terephthalate anion (TA), shown in Figure 4.1, is a known profluorescent hydroxyl radical scavenger [9–18]. A profluorescent molecule is non- or minimally fluorescent in one form but highly fluorescent once reacted making these molecules well-studied to optical monitoring of chemical reactions. TA is known to react with hydroxyl radicals to ultimately form the fluorescent hydroxyterephthalate (TAOH) after a number of sequential reactions (Figure 1) [9, 10, 13]. Hydroxyl radicals efficiently react with TA forming 1,4-dicarboxy-2-hydroxycyclohexadienyl radical (TAOH$^{\cdot}$) that is followed by an oxidation process to form TAOH [9, 10, 13]. TA has been used to detect hydroxyl radicals in sonolysis [9, 10, 18], radiolysis [19], photolysis [14] and metal catalysis [16] studies with links to biological [20] and industrial studies [21]. Due to its wide use throughout these fields, the chemical characteristics of TA should be well defined. A summary of literature rate constants for the hydroxylation of TA and the common oxidation pathways are summarised in Table 4.1.

Previous studies have shown that the initial hydroxyl addition reaction occurs quickly and would complete in less than 250 ns for the lowest TA concentrations presented here. The product from this initial addition (TAOH$^{\cdot}$) is non-fluorescent and must be oxidised to form the final fluorescent TAOH. Studies by Fang *et al.*

Table 4.1: Published rates for hydroxylation of terephthalate.

Reaction	Rate constant	Author
TA + $OH^{\cdot} \rightarrow TAOH^{\cdot}$	$k_1 = 3.3\times10^9$ $M^{-1}s^{-1}$	Fang *et al.* (1995)
TA + $OH^{\cdot} \rightarrow TAOH^{\cdot}$	$k_1 = 4.4\times10^9$ $M^{-1}s^{-1}$	Page *et al.* (2010)
2 $TAOH^{\cdot} \rightarrow$ TAOH + TA + H_2O	$k_2 = 2.5\times10^8$ $M^{-1}s^{-1}$ (pH 5) $k_2 = 4\times10^7$ $M^{-1}s^{-1}$ (pH 10.2)	Fang *et al.* (1995) Fang *et al.* (1995)
$TAOH^{\cdot}$ + $O_2 \rightarrow TAOHOO^{\cdot}$	$k_3 = 1.6\times10^7$ $M^{-1}s^{-1}$	Fang *et al.* (1995)
$TAOHOO^{\cdot} \rightarrow TAOH^{\cdot}$ + O_2	$k_{-3} = 3.4\times10^3$ s^{-1}	Fang *et al.* (1995)
$TAOHOO^{\cdot} \rightarrow$ TAOH + $HO_2^{\cdot}$	$k_4 = 3.9\times10^2$ s^{-1}	Fang *et al.* (1995)
TAOH + $OH^{\cdot} \rightarrow TA(OH)_2^{\cdot}$	$k_5 = 6.3\times10^9$ $M^{-1}s^{-1}$	Page *et al.* (2010)

have shown that there are two oxidation pathways that are possible, one being a disproportionation reaction where two $TAOH^{\cdot}$ radicals react to form a TAOH, TA and water, while the second requires an oxygen addition to form a peroxyl species ($TAOHOO^{\cdot}$) that must undergo further reaction to form TAOH. Under aerobic conditions it was found that the oxygen addition pathway dominates but leads to lower TAOH yields, as $TAOHOO^{\cdot}$ can follow a number of decomposition pathways leading to non-fluorescent products. Although the $TAOHOO^{\cdot}$ species is the major product, the $HO_2^{\cdot}$ loss pathway that generates the fluorescent TAOH is much slower than the O_2 loss channel that returns to the $TAOH^{\cdot}$ species. This renders the generation of TAOH through this pathway slow. Neither of these two published oxidation pathways can adequately explain the chemical kinetics that are observed herein.

The following chapter describes a new experimental technique for measuring chemical kinetics in single microdroplets. The experimental setup used throughout this chapter is detailed below. Pseudo-first order rate constants for the oxidation of the resulting $TAOH^{\cdot}$ radical are measured in single microdroplets of water containing various concentrations of TA. This is performed using a precisely timed two-laser setup to measure the growth of the fluorescence emission of TAOH. The measured pseudo-first order rate constants are used to find the second order rate coefficient for the oxidation process, in order to determine whether this experimental technique is able to measure a chemical second order reaction rate coefficient. The ultimate goal of this study is to accurately measure the second order rate constant of this reaction in single microdroplets and compare the measured rate to literature bulk solution values.

4.2 Experimental

Single microdroplets are generated from aqueous solutions containing varying known concentrations of disodium terephthalate (1 – 52 mM). The solutions also contain

10 μM hydrogen peroxide (H_2O_2) that serves as a OH radical precursor. Upon irradiation with 266 nm light, H_2O_2 undergoes photolysis generating hydroxyl radicals within the microdroplet. Formation of TAOH is measured as a function of reaction time by measuring laser induced fluorescence as a function of delay time. Using this strategy the aim is to provide insight into the radical chemistry proceeding within these single microdroplet environments.

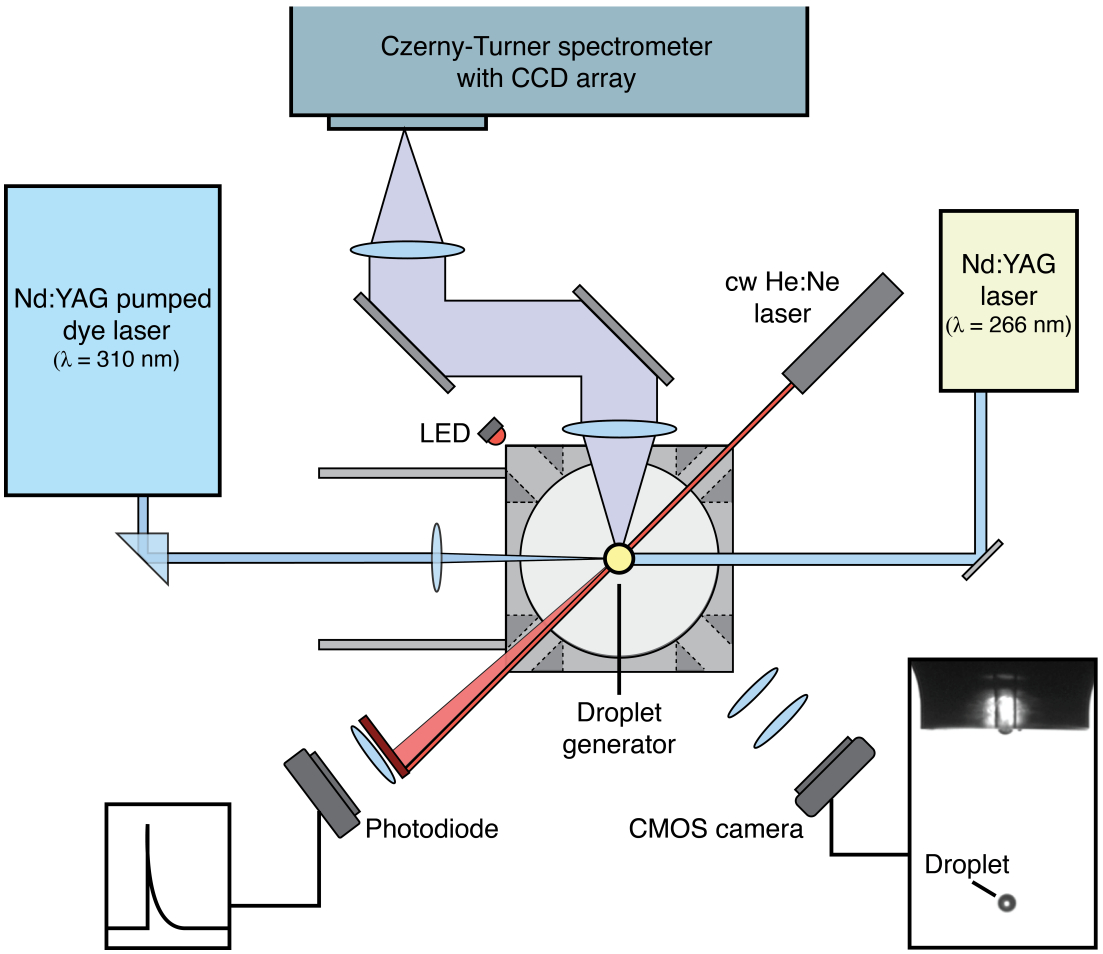

Figure 4.2: Schematic diagram of the microdroplet kinetics experiment.

The droplet generator (Microdrop, MDK-130) is located in the center of a 60 mm cubic chamber that is modified with additional holes along the diagonal axes, as shown in Figure 4.2. As the microdroplets free-fall they are inspected using a CMOS camera aligned along one of the diagonal axes, as shown in Figure 4.2. Directly opposing the CMOS camera is a light emitting diode that is pulsed (3V amplitude, 4 μs pulse-length) at a controllable time-delay after microdroplet generation, creating a single bright-field image for every single microdroplet. The droplet is imaged, via a compound microscope, onto the CMOS camera. Along the alternate diagonal axis, a continuous wave He:Ne laser (Thorlabs, 632.8 nm, 2 mW, HRP020-1) is focused through the centre of the chamber by a 25 mm lens (f = 100 mm). As

the microdroplet transverses the He:Ne beam, elastically scattered laser pulse is collected by a photodiode. Before the photodiode, a 25 mm lens (f = 75 mm) collects and focuses the elastically scattered light onto the photodiode. In addition to the collection lens, a 633 nm line-pass filter is situated in front of the photodiode ensuring mostly elastically scattered laser light reaches the detector. The cw He:Ne laser beam terminates to the side of the photodiode housing. The detected elastically scattered light is used to synchronise two pulsed-lasers by triggering two digital delay generators (DG645, Stanford Research Systems) with the rising edge of this signal. One delay generator controls the timing of the visualization LED and the spectrometer's CCD exposure and the second delay generator controls the flashlamp and Q-switch timing of the two pulsed-laser systems.

Two pulsed-lasers are optically aligned, counter propagating, through the centre of the chamber. The first is a Nd:YAG pulsed laser (Minilite II, Continuum) operating on the 4th harmonic (2.5 mJ, λ = 266 nm) that is used as the photolysis laser. This laser is not focused, as it is required to irradiate microdroplets at varying laser delays without any adjustments to the alignment. Chemical reactions are measured over ~25 μs, which corresponds to the microdroplets traveling a distance of ~50 μm, or approximately one microdroplet diameter. As this distance is short, it is assumed that the unfocused photolysis lasers beam profile is uniform over this distance, meaning each microdroplet is irradiated with the same number of photons. The second laser system is a dye laser (Sirah Lasertechnik Cobra-Stretch), pumped with the second harmonic (λ = 532 nm) from a pulsed Nd:YAG laser (Spectra-Physics QuantaRay Pro-230), operating on Rhodamine 101 in ethanol and lasing at 620 nm. This wavelength is then frequency doubled to produce 310 nm. The 310 nm pulse is used to excite the fluorescent TAOH as a function of delay time from the photolysis pulse. This laser is gently focused onto the microdroplets by a 25 mm lens (f = 150 mm) in order to increase the fluorescence signal. This allows the measurement of low TA concentrations (<5 mM).

Fluorescence from the microdroplets is collected and collimated perpendicular to the laser input axis by a 2" lens (f = 60 mm) and directed towards the Czerny-Turner spectrometer (Andor Shramrock 303i) with a CCD detector (Andor iDus DV401A-BV, 1024x127). Prior to entering the spectrometer, the collected light is focused by a second 2" lens (f = 150 mm) chosen to best match the f-number of the spectrometer ($f/6$). Once inside the spectrometer, the light is dispersed onto the CCD array by a 300 lines/mm grating centered at 375 nm. This provides detection over a spectral region ranging from 231.93 to 517.11 nm, which is sufficient to collect the entire TAOH fluorescence emission band centred at 427 nm and ranging from 370 – 500 nm. The CCD detector exposure is triggered immediately (0 ns delay) after the He:Ne scattered light detection with a 100 ms exposure time. This ensures

that fluorescence emission is collected from a single microdroplet.

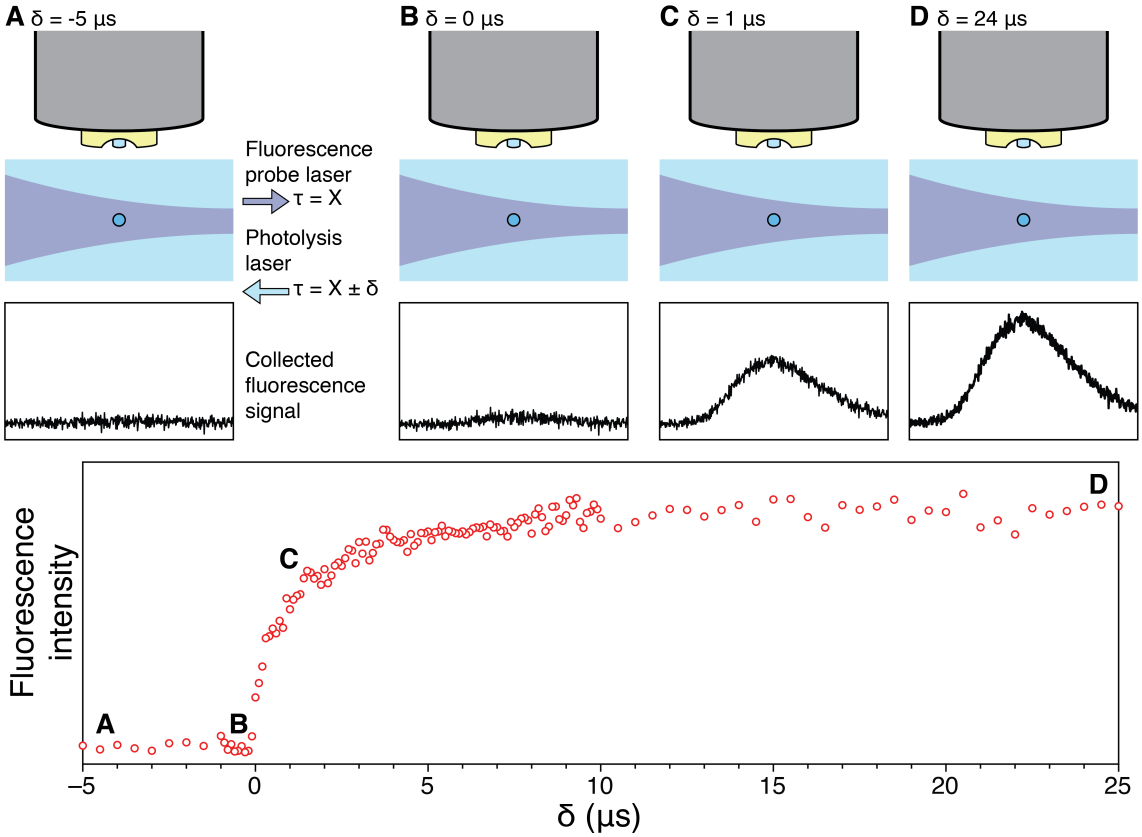

Figure 4.3: Graphical summary of the single microdroplet kinetics measurement. (A) The microdroplet is initially subjected to the photolysis laser pulse after the probe laser, no chemistry has occurred. (B) Both lasers irradiate the microdroplet at the same time ($\tau = 0$ in regards to the reaction). (C) The photolysis laser pulses the microdroplet 1 μs before the probe. (D) Photolysis occurs 24 μs before the probe laser, effectively 24 μs of reaction has occurred.

To observe the TA formation kinetics, the fluorescence emission from the microdroplets is measured at controlled delay times between the two pulses: the pump ($\lambda = 266$ nm) and probe ($\lambda = 310$ nm) (as depicted in Figure 4.3). The probe laser is triggered to pulse at a fixed delay after the detected He:Ne scatter, typically 300 μs. This ensures that the fluorescence emission is detected at the same time for every single microdroplet. As a background determination, the photolysis laser is triggered to pulse 5 μs after the probe laser as shown in panel A (Figure 4.3). Since photolysis is occurring after the probe laser, no fluorescence emission is detected as no fluorescent species should be present within the microdroplet. The photolysis laser delay is stepped, with coarse steps (500 ns) at the start and end of each measurement and fine steps (50 ns) over the initial fluorescence growth, after each microdroplet. This iterative stepping procedure is controlled by a custom LabView program that communicates with the delay generator via GPIB. A screenshot of the custom LabView program is shown in Figure 4.4 When the laser delay is negative,

the photolysis laser pulses after the probe laser with no reaction occurring before the probe. At a laser delay of zero, both lasers irradiate the droplet at the same time. Once the laser delay is positive, the photolysis laser pulses before the probe laser allowing the reaction to commence prior to the fluorescence probe. As the time delay between the two laser pulses increases, the allowed reaction time also increases and a time-resolved fluorescent signal is measured. By plotting the total fluorescence emission intensity against the time delay between the two lasers, labeled as δ in Figure 4.3, the fluorescence growth can be measured.

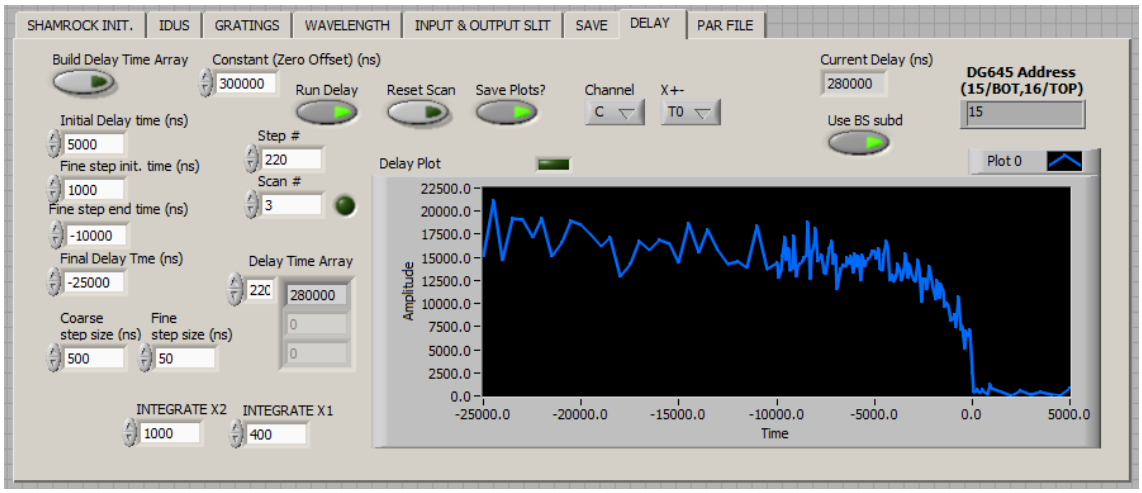

Figure 4.4: Screenshot of the custom LabView program that controls the iterative laser-delay stepping procedure.

4.3 Results

TAOH fluorescence emission is collected from single microdroplets with varying TA concentrations, ranging from 1.0 – 52.5 mM. A scan of all laser delay times is combined to produce a 3D intensity plot shown in Figure 4.5. Time-dependent fluorescence growth curves are extracted from this plot by integrating over a specified wavelength range. This can be performed for entire fluorescence emission or smaller domains. Figure 4.5 A shows the fluorescence growth from a single emission wavelength (λ = 427 nm). After integration along the laser delay axis (Figure 4.5 B), a fluorescence emission spectrum is obtained.

Kinetic traces are extracted from each TA concentration (Figure 4.6) and fitted with the following standard exponential growth function:

$$f(t) = 1 - \mathrm{A}e^{-kt} + c \tag{4.1}$$

Where t is the effective reaction time (i.e. the two-laser delay time), A is the pre-exponential factor, c is an offset and k is the rate constant. Traces are only

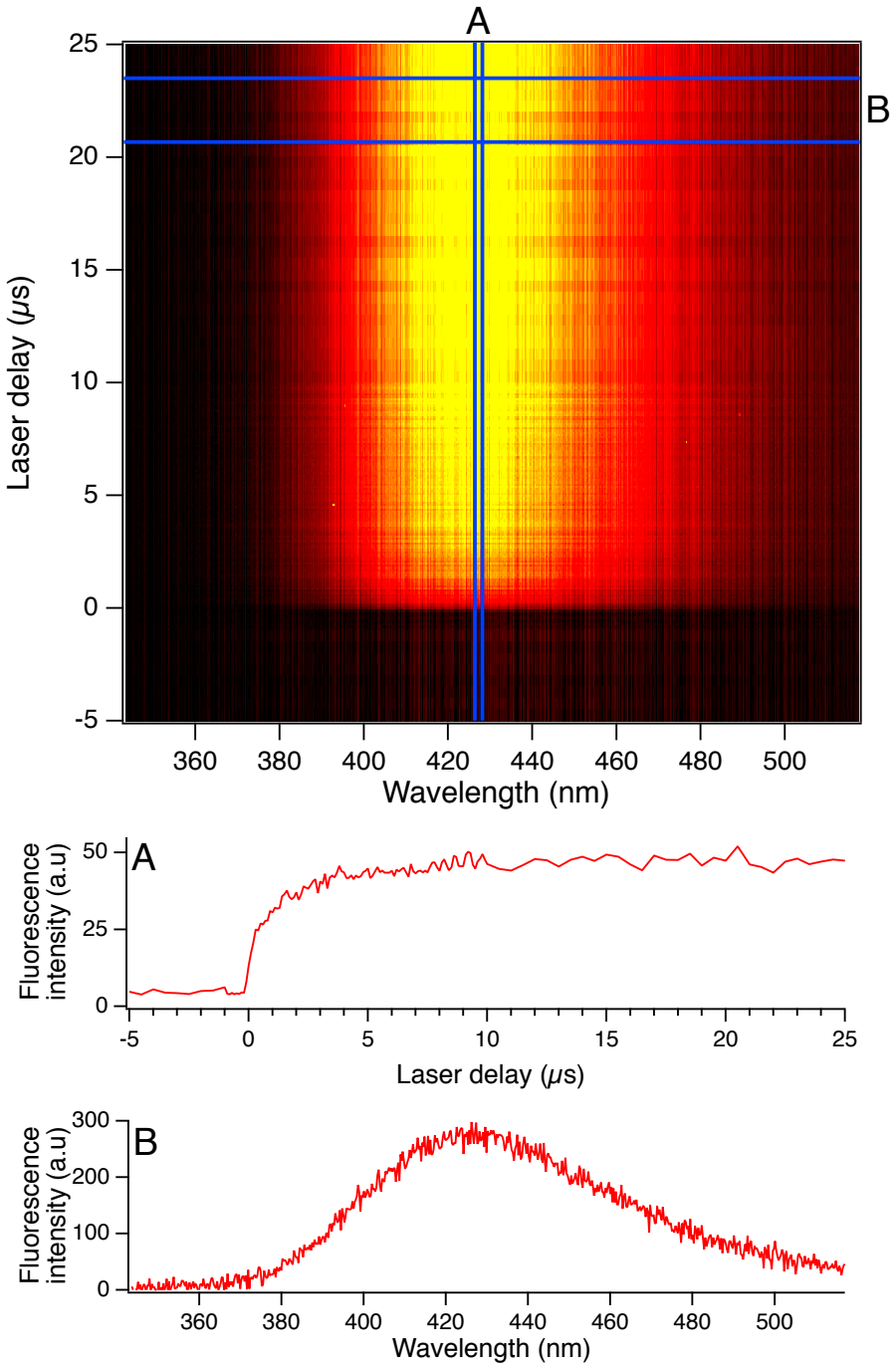

Figure 4.5: Measured TAOH fluorescence emission collected from single microdroplets, containing 52 mM TA, at each photolysis laser delay time. Growth of the fluorescence band is observed once the photolysis laser irradiates the micrdroplet before the probe, occurring at laser delays less than 0 ns. (A) Integration between the two vertical blue lines located at $\lambda = 427$ nm provides a trace of the fluorescence growth. (B) Integration between the two horizontal blue lines providing a fluorescence emission spectrum from the TAOH.

fit from laser delays greater than 0.2 μs, as the initial hydroxyl radical addition may still be occurring in the lowest concentration samples. In order to avoid any convolution of these kinetics these data points are omitted from the fit. As the curves in Figure 4.6 show, the function provides a good fit to the data. From these fitted curves the pseudo-first order rate constants (k) are extracted for each measured TA concentration.

Figure 4.7 shows the fitted pseudo-first order rate constants (k) measured at each TA concentration. Strikingly these data do not follow a linear trend as might be expected. The fitted pseudo-first order rate constants appears to plateau at TA concentrations higher than 20 mM. The lower TA concentrations (0 – 11.5 mM) and high concentration (11.5 – 52.5 mM) were fitted separately, as shown by the dashed lines in Figure 4.7. The lower concentration line was found to have a gradient of 4.6 $\pm$ 0.2$\times 10^7$ $M^{-1}s^{-1}$ (k_{low}), while the higher concentration was 3.4 $\pm$ 1.2$\times 10^6$ $M^{-1}s^{-1}$ (k_{high}) (with an intercept of 2.5 $\pm$ 0.3$\times 10^5$ $M^{-1}s^{-1}$). This suggests that there is a transition at approximately 10 mM where the rate constants plateau. But it is not immediately clear how to interpret this result set.

The fluorescence growth curve for each fluorescence emission wavelength was fitted with the same exponential function to determine whether there was any wavelength dependent phenomena. Figure 4.8 shows the fitted rate constant (k) values for each wavelength of the fluorescence emission. At the shorter wavelengths, those below 390 nm, the fitted k values are largely scattered due to these wavelengths being on the edge of the fluorescence emission band. At wavelengths longer than 390 nm it appears that the fitted k values are constant until 480 nm, which is nearing the edge of the band. There is a noticeable systematic decrease in the fitted k values at wavelengths longer than 480 nm, but along with an increased uncertainty suggesting there is not sufficient signal to provide a good fit.

A possible explanation for the decrease in the rate constant values at higher TA concentration is that some TA may be precipitating within the droplet generator's capillary. To test this, a 52.5 mM TA solution, without H_2O_2, was subjected to UV-vis spectroscopy before and after being passed through the droplet generator. It was found that there was no discernible difference in the absorbance intensity (<0.001) at 260 nm after the solution had been pushed through the droplet generator.

The effect of photolysis laser power was investigated by measuring fluorescence growth with the laser photolysis power reduced from 2.5 to 1.1 mJ/pulse. Two fluorescence growth curves collected from droplets containing 17.4 mM TA irradiated are shown in Figure 4.9, the data in red represents droplets irradiated with 2.5 mJ/pulse photolysis laser energy, while the blue corresponds to the 1.1 mJ/pulse. It was found that there was significant difference with the fitted pseudo-first order k from the 1.1 mJ/pulse measurement being $\sim$60% slower than that measured at 2.5

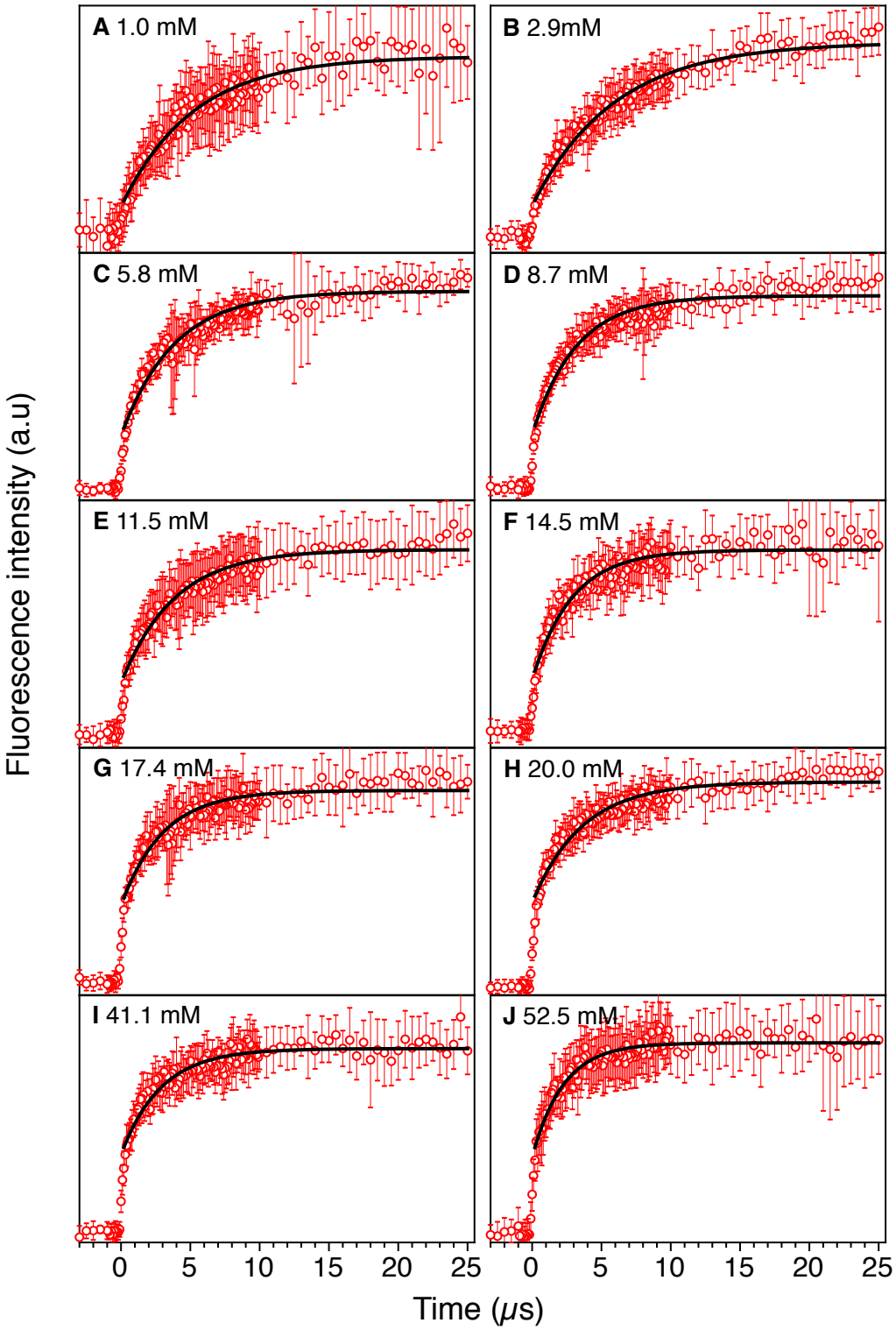

Figure 4.6: Measured fluorescence growth curves for various TA concentrations and the resulting exponential fits. Curves are extracted from the fluorescence emission at 427 nm.

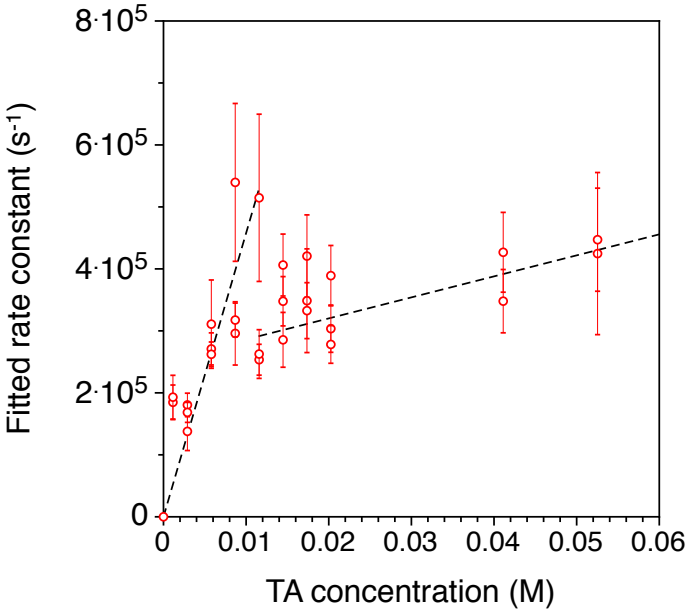

Figure 4.7: The resulting fitted fluorescence growth rate constants at various terephthalate concentrations.

mJ/pulse. This result is evidence that the kinetics of the measured reaction could be dependent on the OH concentration, which affects the pseudo-first order assumption. A similar power dependence study was conducted in earlier experiments, not shown here, and found no variation over a range of laser energies. This points to reproducibility issues that may arise from the complex radical chemistry affecting the reaction. This will be discussed further below.

4.3.1 Single droplet desorption mass spectrometry

Because of this unexpected kinetic behaviour, more insight into the chemistry occurring with the single droplets was needed. Therefore, single droplet desorption mass spectrometry (SDDMS), a technique that will be described in more detail in Chapter 5, was utilised to probe the resulting chemistry of the photolysis event. This technique uses a probe needle desorption platform to probe single microdroplets using a commercial mass spectrometer. Single microdroplets containing 100 μM TA and $\sim$100 nM H_2O_2 were analysed with the mass spectra shown in Figure 4.10.

The top spectrum is measured from single microdroplets that have not been irradiated by the 266 nm photolysis laser pulse. TA is the most abundant species with the singly protonated form (TA^-) at m/z 165 and the monosodium adduct at m/z 187. It is also noticeable that there is a number of other peaks present as background. When the droplet is irradiated (Laser On) there is an increase in the relative abundance of these minor products, which is due to the reduction of total ion count as some TA either reacts or decomposes to form neutral products when

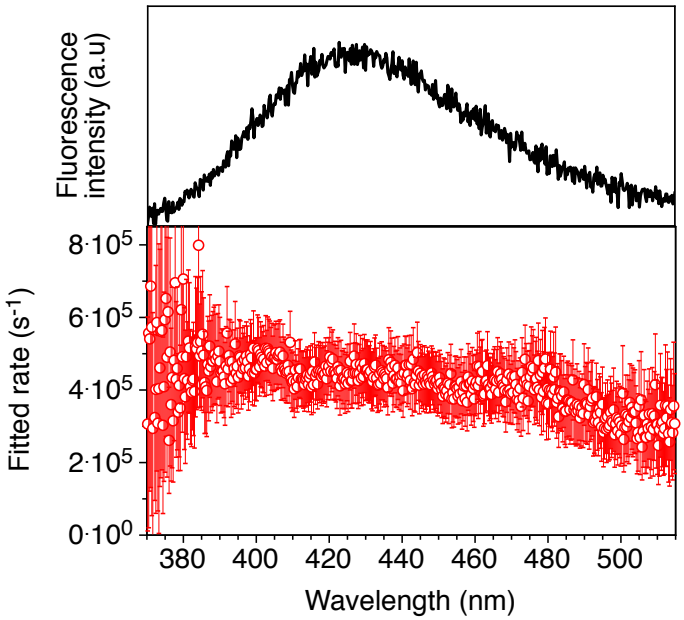

Figure 4.8: Fitted rate constants (k) at each wavelength of the fluorescence emission collected from single microdroplets containing 52.5 mM TA.

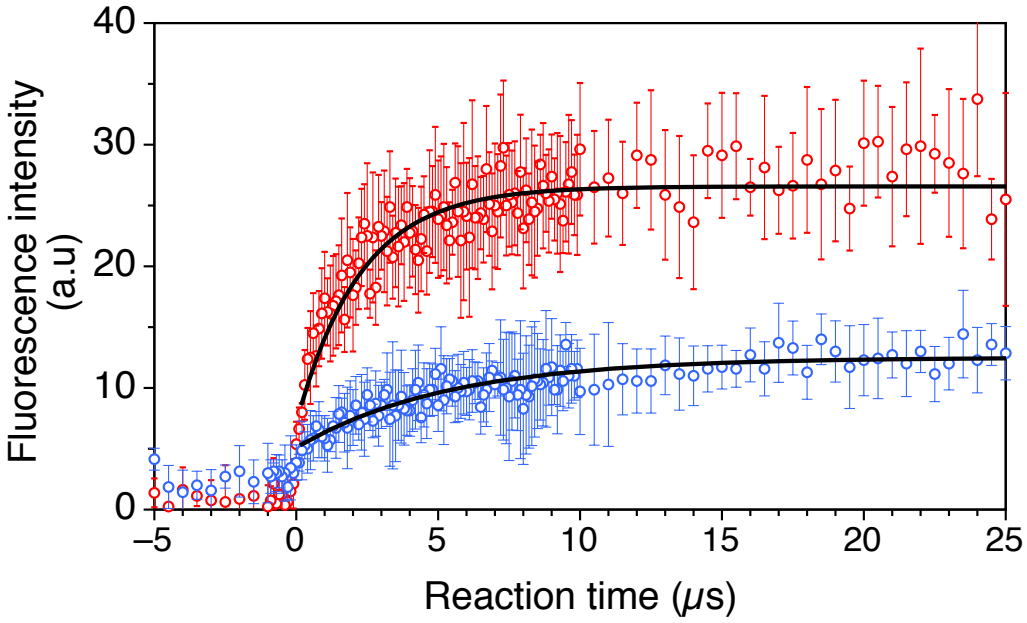

Figure 4.9: Resulting fluorescence growth curves from microdroplets irradiated with 2.5 (red) and 1.1 mJ/pulse laser powers. The black lines represent the best exponential fit.

subjected to laser irradiation. However, there is a new photoproduct at m/z 181 which corresponds to the singly protonated TAOH anion ($TAOH^-$). Additionally m/z 197 is also detected as a photoproduct, which is 16 Da greater than the TAOH and provides evidence that there may be a second hydroxylation occurring. Considering that the TA concentration is much greater than H_2O_2, it is surprising that photoproducts consistent with a second OH addition are detected. This

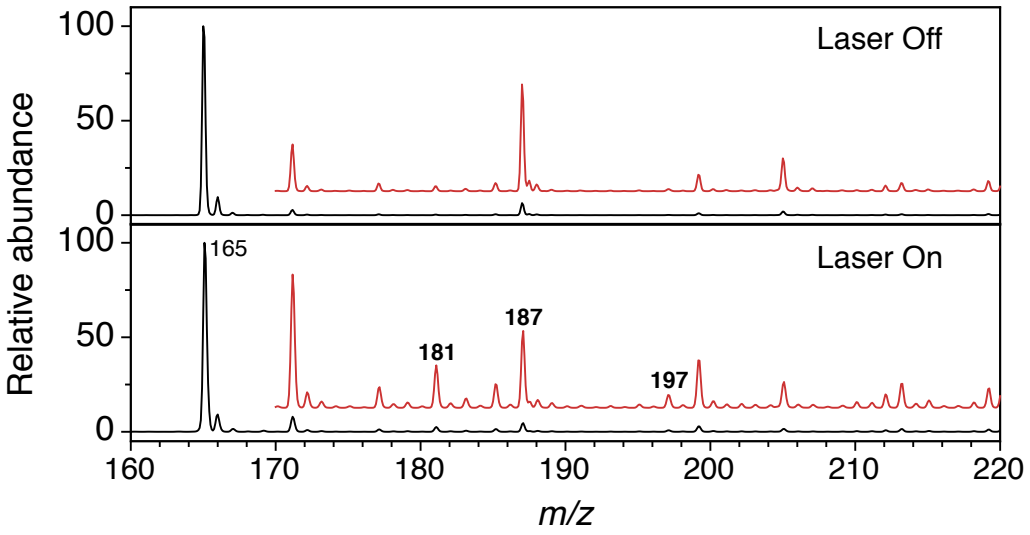

Figure 4.10: Mass spectra collected from single water droplets containing TA and H_2O_2 before (top) and after (bottom) UV laser irradiation.

may be evidence for more complicated radical chemistry taking place within the microdroplet. Radical chain chemistry pathways may be affecting the kinetics with complex concentration dependencies.

4.4 Discussion

The initial hydroxyl addition to the TA dianion, as shown in Scheme 4.1, is known to be an efficient, fast reaction and at the concentrations used here will come to completion on the nanosecond timescale. The TAOH detection experiment show reactions on the order of tens of microseconds. The product of the OH addition reaction is the adduct complex TAOH$^{\cdot}$, which is non-fluorescent and is not detected by the technique. These kinetic data measured here arise from the reaction of TAOH$^{\cdot}$ to form the fluorescent product TAOH. Previously, studies have considered the kinetics for the formation of the TAOH by two pathways [9, 19].

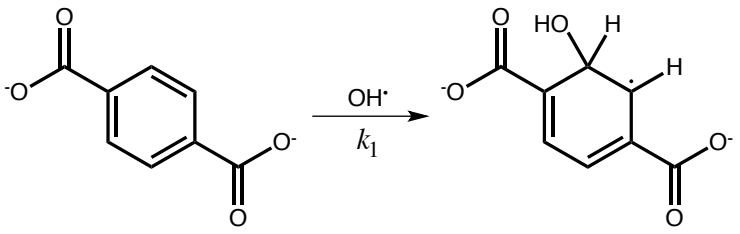

Scheme 4.1

It has been shown that in anaerobic conditions the TAOH$^{\cdot}$ species can undergo a disproportionation reaction, shown in Scheme 4.2, where two TAOH$^{\cdot}$ radicals produce a TAOH molecule, a TA molecule and water [9, 19]. A study by Fang

et al. (1995) found the second order rate coefficient for this reaction varied with pH. It was found that at a higher pH (10.5) the measured rate constant was 4×10^7 $M^{-1}s^{-1}$ [9], while at a lower pH (5) the measured rate constant was 2.5×10^8 $M^{-1}s^{-1}$. The low TA concentration second-order rate coefficient (k_{low}) fitted in Figure 4.7 was $4.6 \pm 0.2\times10^7$ $M^{-1}s^{-1}$ which is on the same order as these literature values. While the results are similar, the data presented here are exhibiting some (albeit complex) trend with TA concentration, the published disproportionation reaction rate constant has no dependence on TA concentration. Additionally, the samples used here were not purged of dissolved O_2 and hence the conditions within the droplet are aerobic. Assuming the maximum $TAOH^{\cdot}$ concentrations possible in this study ($[TAOH^{\cdot}] = 20$ μM for a quantum yield of 2 for the H_2O_2 photolysis) the time to required to complete this reaction is on the order of milliseconds while the data presented here is completed within 25 μs. This suggests that the rate coefficient measured here is not due to the disproportionation reaction.

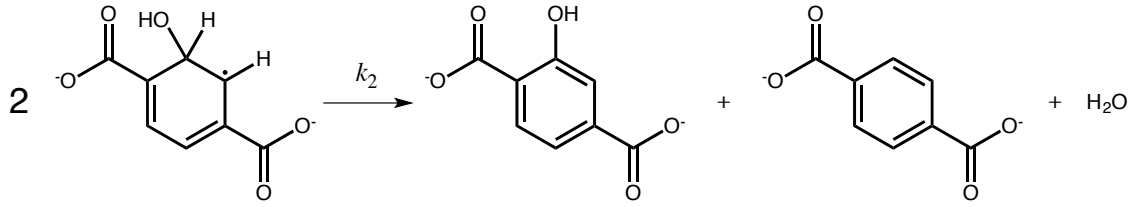

Scheme 4.2

Fang and coworkers have shown that oxidation of the $TAOH^{\cdot}$ radical species can occur via oxygen addition to the radical, as shown in Scheme 4.3, with a second order rate coefficient of 1.6×10^7 $M^{-1}s^{-1}$ [9]. This oxidation pathway requires a subsequent reaction to produce the final fluorescent TAOH product. $TAOHOO^{\cdot}$ must undergo a $HO_2^{\cdot}$ elimination to form TAOH. In the same study it was found that the unimolecular $HO_2^{\cdot}$ elimination has a first-order rate coefficient of 3.9×10^2 s^{-1} [9] that is an order of magnitude slower than the reverse reaction, an O_2 loss to return to the $TAOH^{\cdot}$ species (3.4×10^3 s^{-1}) [9]. As the initial $OH^{\cdot}$ addition is much faster than the following O_2 pathway steps it can be assumed, using the steady-state approximation, that the $OH^{\cdot}$ addition is completed and that the concentration of $TAOH^{\cdot}$ is equal to the $OH^{\cdot}$. To give an idea of what the observed overall rate coefficient for this pathway would be, the following rate law can be written:

$$\frac{d[\mathrm{TAOH}]}{dt} = \frac{k_4 k_3 [\mathrm{TAOH}^{\cdot}][\mathrm{O_2}]}{k_4 + k_{-3}} \tag{4.2}$$

Using the published rate coefficients for this pathway (Table 4.1), an observed rate coefficient of 1.65×10^6 $M^{-1}s^{-1}$ is expected. This is within an order of magnitude of the fitted k_{high} values ($3.4 \pm 1.2\times10^6$ $M^{-1}s^{-1}$). Assuming the

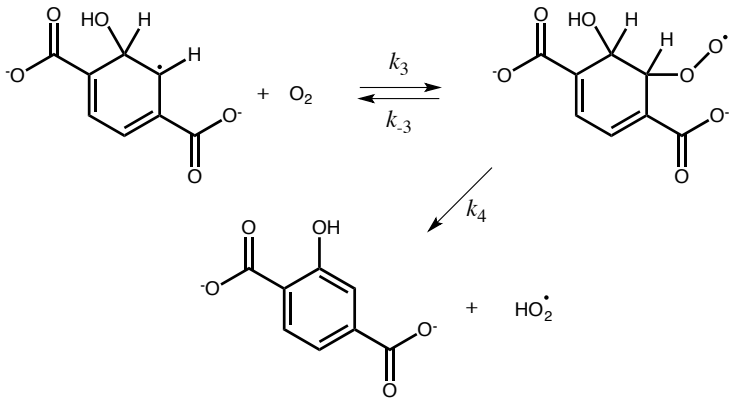

Scheme 4.3

oxygen concentration within the droplets is at a maximum (0.25 mM at 25°C) this oxidation pathway would require ∼2.5 ms to come to completion. Similar to the disproportionation pathway, this O_2 addition route has no dependence on the TA concentration and is too slow to account for the fluorescence growth times observed here.

Both oxidation pathways from literature cannot be reconciled with the measured data, as neither is fast enough or can explain the TA concentration dependence. However, organic aromatic molecules are known to act as electron acceptors for aromatic radical anions, as resonance stability allows the formation of stable aromatic radicals [22]. The most common aromatic molecules that can act in this way are large polycyclic structures, like naphthalene, or benzene derivatives containing electron withdrawing functional groups, such as nitrobenzene [22–24]. These oxidation reactions occur rapidly with second-order rate constants on the order of 10^8 – 10^9 $M^{-1}s^{-1}$ depending on the electron acceptor's structure [23, 24]. TA could potentially act in this manner as it contains two carboxylate groups that are weak electron withdrawing functional groups.

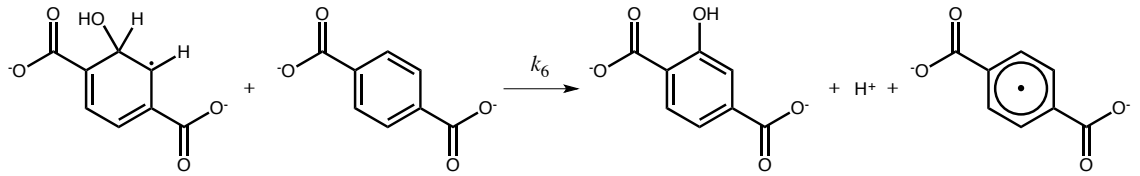

Scheme 4.4

This pathway requires TA to act as an electron acceptor to oxidise the $TAOH^{\cdot}$ species (Scheme 4.4). Despite both reactants being dianions the droplet solvent is water and also contains Na^+ counter ions from the TA salt so this reaction might be possible. Coloumbic repulsion may explain why k_{low} ($4.6 \pm 0.2 \times 10^7$ $M^{-1}s^{-1}$) was found to be an order of magnitude slower than other neutral substituted benzene molecules, such as dinitrobenzene [24] and terephthalonitrile [23]. While

the electron transfer rate coefficients for this neutral species were measured in dimethylformamide, similar rate coefficients can be assumed for a water solvent [22]. Interestingly, this oxidation pathway is not mentioned in previously studies of TA, but in the experiments performed here the TA concentrations are greater than that typically used in literature which may allow this reaction to compete.

Although this reasoning may provide an explanation to what oxidation process is generating the TAOH, none of these pathways can explain why the fitted pseudo-first order rate constants exhibit the plateau at higher TA concentrations. The decreased rate observed at higher TA concentrations (>10 mM) may be due to a number of chemical or physical processes.

Reactions while photolysed H_2O_2 is "caged" by solvent effects could explain the reduced rate at high TA concentrations. When H_2O_2 undergoes photolysis in the condensed-phase, the excited molecule can be trapped within a solvent cage before separating into two radicals, in this case $OH^{\cdot}$, as depicted in Scheme 4.5 [25]. At high TA concentrations the mean inter-particle distance between TA molecules is greatly reduced. For example the mean inter-particle distance for the TA concentrations used here is 12 nm, at the lowest TA concentration (1 mM) and <5 nm for the high concentrations (>10 mM). The average distance between a H_2O_2 and the surrounding TA molecule is also greatly reduced. This decreased inter-particle distance could lead to an increase in multiple $OH^{\cdot}$ additions to the same TA molecule, if the TA molecule is able to interact while the photolysed H_2O_2 is "caged". The second order rate coefficient for the $OH^{\cdot}$ addition to TAOH (the second hydroxylation) is slightly greater than that for TA (Table 4.1), suggesting that once TAOH has formed the addition of a second $OH^{\cdot}$ is competitive. This can lead to the formation of other products such as dihydroxyterephthalate and non-fluorescent products via ring opening [9]. An increase in the formation of non-fluorescent products and the resulting decrease in TAOH yields could explain the roll-over observed at high TA concentrations. As shown in the mass spectra collected using SDDMS (Figure 4.10), a photodependent signal was observed at m/z 197, which corresponds to the singly protonated dihydroxyterephthalate species ($TA(OH)_2^-$). This provides evidence that the second hydroxylation product is present and that reactions involving two $OH^{\cdot}$ are able to occur.

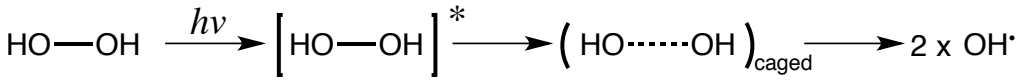

Scheme 4.5

Changes in the optical properties of the droplets may also be the cause of the unexplained plateau in rate constants. As the TA concentration increases the absorption profile of the droplet solutions also increases, which ultimately

leads to a decrease in transmittance. To investigate how much the increase of TA concentration affects the absorption profile the molar extinction coefficient of disodium terephthalate was measured using conventional UV-vis spectroscopy. The measured molar extinction coefficient of TA, at 266 nm, is 2770 ± 50 $cm^{-1}M^{-1}$. Using this value, the transmittance is calculated for a each TA concentration used, assuming that the optical pathlength is equal to the diameter of the microdroplet (50 μm). This does not account for the spherical shape of the droplet. The resulting transmittance values are shown in Figure 4.11.

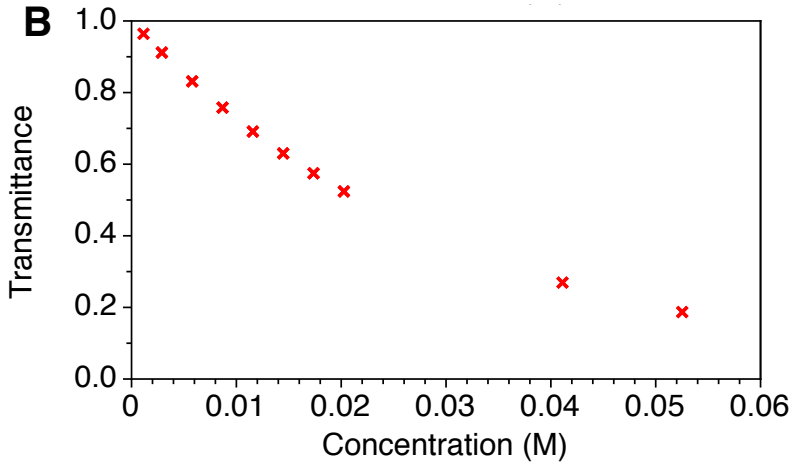

Figure 4.11: Calculated transmittance for 266 nm light interacting with aqueous microdroplets (50 μm diameter) with varying TA concentrations.

As shown in Figure 4.11 the transmittance at 266 nm follows an exponential decay as the concentration of TA increases. The transmission varies greatly over the TA concentration range and could affect the yield of the H_2O_2 photolysis (i.e the OH concentration). If the formation of TAOH is dependent on $TAOH^{\cdot}$ recombination kinetics ($TAOH^{\cdot}$ + $TAOH^{\cdot}$), or an electron transfer with TA ($TAOH^{\cdot}$ + TA), the concentration of $OH^{\cdot}$ will affect this reaction, as the $TAOH^{\cdot}$ concentration is considered equal to the $OH^{\cdot}$ when the TA concentration is much greater than the H_2O_2. But, because the chemistry within the microdroplet is complex, the exact process leading to the formation TAOH remains unknown.

Ultimately, these results have shown that while chemical transformations can be measured from streams of single free-falling droplets, for complex reaction mechanisms the technique needs to be expanded to incorporate other detection methods. Also, other radical reactions and detection strategies need to be explored. The study also showed that the chemical kinetics observed did not follow any of the literature pathways for this well-studied hydroxylation reaction, but may be explained by a previously unreported pathway. Whether the microdroplet have characteristic properties that affect the chemical kinetics also remains an interesting unknown.

4.5 Conclusions

Pseudo-first order rate constants for the oxidation of $TAOH^{\cdot}$ in single microdroplets of water were measured with the resulting rate constants appearing to plateau at high TA concentrations. Two second-order rate coefficients were found, one for low TA concentrations (k_{low}) and one for high TA concentrations (k_{fast}). Neither of the rate coefficients could be explained by previously reported oxidation pathways as both showed dependence on TA concentration, suggesting that the oxidation was affected by an unreported pathway involving the original TA molecule.

This study has demonstrated that using a precisely timed two-laser setup chemical kinetics in single microdroplets can be followed, utilising laser-induced fluorescence. The main limitation of this technique is the requirement for an optically sensitive chemical system with products or reactants required to exhibit a change in optical properties that can be detected. Hence, further development is required to expand upon the detection abilities of the technique, but nonetheless the strategy is presented here.

4.6 References for Chapter 4

(1) J. B. Wills, J. K. Knox and J. P. Reid, "Optical control and characterisation of aerosol", *Chemical Physics Letters*, 2009, **481**, 153–165.

(2) J. P. Reid and L. Mitchem, "Laser probing of single-aerosol droplet dynamics", *Annual Review of Physical Chemistry*, 2006, **57**, 245–271.

(3) U. K. Krieger, C. Marcolli and J. P. Reid, "Exploring the complexity of aerosol particle properties and processes using single particle techniques", *Chemical Society Reviews*, 2012, **41**, 6631–6662.

(4) B. J. Dennis-Smither, R. E. H. Miles and J. P. Reid, "Oxidative aging of mixed oleic acid/sodium chloride aerosol particles", *Journal of Geophysical Research: Atmospheres*, 2012, **117**, D20204, 1–13.

(5) F. D. Pope, B. J. Dennis-Smither, P. T. Griffiths, S. L. Clegg and R. A. Cox, "Studies of Single Aerosol Particles Containing Malonic Acid, Glutaric Acid, and Their Mixtures with Sodium Chloride. I. Hygroscopic Growth", *The Journal of Physical Chemistry A*, 2010, **114**, 5335–5341.

(6) R. E. H. Miles, J. P. Reid and I. Riipinen, "Comparison of Approaches for Measuring the Mass Accommodation Coefficient for the Condensation of Water and Sensitivities to Uncertainties in Thermophysical Properties", *Journal of Physical Chemistry A*, 2012, **116**, 10810–10825.

(7) S. F. Simpson, J. R. Kincaid and F. J. Holler, "Microdroplet Mixing for Rapid Reaction-Kinetics with Raman Spectrometric Detection", *Analytical Chemistry*, 1983, **55**, 1420–1422.

(8) S. F. Simpson and F. J. Holler, "Effects of experimental variables on the mixing of solutions by collision of microdroplets", *Analytical Chemistry*, 1988, **60**, 2483–2487.

(9) X. W. Fang, G. Mark and C. vonSonntag, "OH radical formation by ultrasound in aqueous solutions .1. The chemistry underlying the terephthalate dosimeter", *Ultrasonics Sonochemistry*, 1996, **3**, 57–63.

(10) G. Mark, A. Tauber, L. A. Rudiger, H. P. Schuchmann, D. Schulz, A. Mues and C. von Sonntag, "OH-radical formation by ultrasound in aqueous solution - Part II: Terephthalate and Fricke dosimetry and the influence of various conditions on the sonolytic yield", *Ultrasonics Sonochemistry*, 1998, **5**, 41–52.

(11) L. X. Li, Y. Abe, Y. Nagasawa, R. Kudo, N. Usui, K. Imai, T. Mashino, M. Mochizuki and N. Miyata, "An HPLC assay of hydroxyl radicals by the hydroxylation reaction of terephthalic acid", *Biomedical Chromatography*, 2004, **18**, 470–474.

(12) M. Sahni and B. R. Locke, "Quantification of hydroxyl radicals produced in aqueous phase pulsed electrical discharge reactors", *Industrial and Engineering Chemistry Research*, 2006, **45**, 5819–5825.

(13) I. Snyrychova and E. Hideg, "The first application of terephthalate fluorescence for highly selective detection of hydroxyl radicals in thylakoid membranes", *Functional Plant Biology*, 2007, **34**, 1105–1111.

(14) S. E. Page, W. A. Arnold and K. McNeill, "Terephthalate as a probe for photochemically generated hydroxyl radical", *Journal of Environmental Monitoring*, 2010, **12**, 1658–1665.

(15) S. E. Page, W. A. Arnold and K. McNeill, "Assessing the Contribution of Free Hydroxyl Radical in Organic Matter-Sensitized Photohydroxylation Reactions", *Environmental Science and Technology*, 2011, **45**, 2818–2825.

(16) M. Janus, E. Kusiak-Nejman and A. W. Morawski, "Influence of water temperature on the photocatalytic activity of titanium dioxide", *Reaction Kinetics Mechanisms and Catalysis*, 2012, **106**, 289–295.

(17) S. E. Page, M. Sander, W. A. Arnold and K. McNeill, "Hydroxyl Radical Formation upon Oxidation of Reduced Humic Acids by Oxygen in the Dark", *Environmental Science and Technology*, 2012, **46**, 1590–1597.

(18) R. Y. Xiao, D. Diaz-Rivera, Z. Q. He and L. K. Weavers, "Using pulsed wave ultrasound to evaluate the suitability of hydroxyl radical scavengers in sonochemical systems", *Ultrasonics Sonochemistry*, 2013, **20**, 990–996.

(19) M. Saran and K. H. Summer, "Assaying for hydroxyl radicals: Hydroxylated terephthalate is a superior fluorescence marker than hydroxylated benzoate", *Free Radical Research*, 1999, **31**, 429–436.

(20) J. C. Barreto, G. S. Smith, N. H. Strobel, P. A. McQuillin and T. A. Miller, "Terephthalic acid: a dosimeter for the detection of hydroxyl radicals in vitro", *Life sciences*, 1995, **56**, 7823778, PL89–96.

(21) K. R. Millington and L. J. Kirschenbaum, "Detection of hydroxyl radicals in photoirradiated wool, cotton, nylon and polyester fabrics using a fluorescent probe", *Coloration Technology*, 2002, **118**, 6–14.

(22) I. V. Khudyakov and V. A. Kuz'min, "Oxidation-reduction Reactions of Free Radicals", *Russian Chemical Reviews*, 1978, **47**, 22.

(23) B. A. Kowert, L. Marcoux and A. J. Bard, "Homogeneous electron-transfer reactions of several aromatic anion and cation radicals", *Journal of the American Chemical Society*, 1972, **94**, 5538–5550.

(24) H. Kojima and A. J. Bard, "Determination of rate constants for the electroreduction of aromatic compounds and their correlation with homogeneous electron transfer rates", *Journal of the American Chemical Society*, 1975, **97**, 6317–6324.

(25) J. H. Baxendale and J. A. Wilson, "The photolysis of hydrogen peroxide at high light intensities", *Transactions of the Faraday Society*, 1957, **53**, 344–356.

Chapter 5

Photochemistry of the berberine cation

5.1 Introduction

Photochemistry plays an important role in many biological processes. Investigating the photophysics and photochemistry of these processes is key to understanding their function. Traditionally, photochemical studies in the condensed phase have required sizeable quantities of sample and the use of narrow and broadband light sources (e.g. lamps, lasers), while this has been effective many newer techniques are moving to high throughput and high sample efficiency. Furthermore, elucidating the fundamental photochemical mechanisms remains challenging.

A recently developed technique, single microdroplet desorption mass spectrometry, has investigated liquid-phase photochemistry of small organic molecules one microdroplet at a time [1]. In that study, single microdroplets of methanol containing 10 – 100 μM of 4-iodoaniline and 3-(iodomethyl)-N,N,N-trimethylbenzenamine were investigated using pulsed ultraviolet laser irradiation coupled with online mass spectrometry. The results showed that single microdroplets could be subjected to desorption using a charged needle (+2 kV) with the resulting spray collected by the inlet of a commercial ion trap mass spectrometer. In the case of the microdroplets containing 4-iodoaniline, UV laser irradiation of the microdroplet prior to desorption led to the detection of photoproducts that corresponded to the loss of iodine ($I^{\cdot}$) followed by a subsequent reactions with the methanol solvent. In the case of 4-iodoaniline, protonated aniline, was the most abundant photoproduct with two other photoproducts arising from the addition of a methyl or hydroxyl group to the phenyl radical (Scheme 5.1).

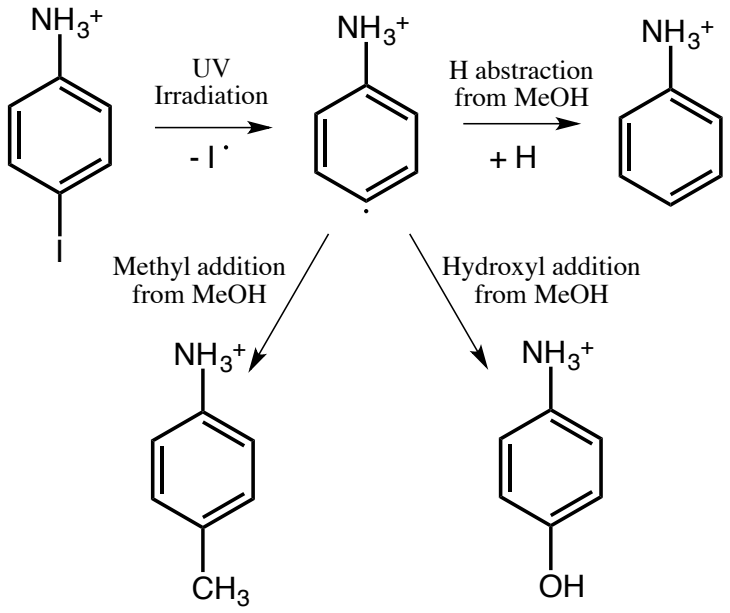

Scheme 5.1

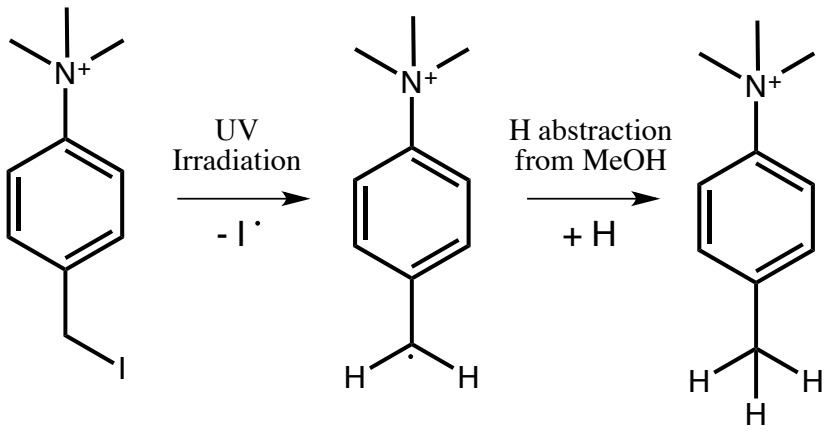

Scheme 5.2

The 3-(iodomethyl)-N,N,N-trimethylbenzenamine system was also studied using the same technique with the main photoproduct resulting from homolysis of the C–I bond losing I$^{\cdot}$ and generating a benzylic radical that was followed by a hydrogen abstraction from the solvent (Scheme 5.2). Interestingly, there was also a major photoproduct arising from the addition of a methoxyl group to the benzylic radical, which was not observed in the iodoaniline measurement. In addition to these two major photoproducts many other photoproducts were detected that were rationalised as forming from reactions with the solvent or methyl losses from the trimethyl amine charge tag. The study demonstrated that the technique is suitable for photochemical measurements of molecules containing photolabile bonds, such as the C–I bond. To further expand the application of this technique, additional development and benchmarking is required, particularly with larger biologically relevant molecules. In the following chapter, the solution phase photolysis of berberine (Figure 5.1) is examined using this single microdroplet technique.

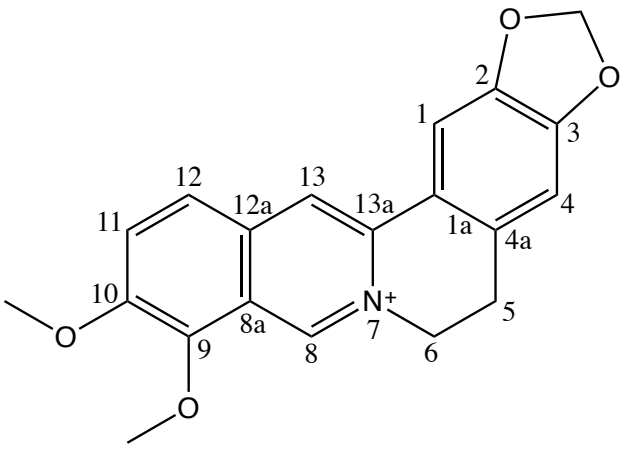

Figure 5.1: The berberine cation (m/z 336) with its reaction sites labeled.

The berberine cation (Figure 5.1) is a naturally occurring isoquinoline alkaloid that is used in traditional Eastern medicine. Berberine has been linked to the treatment of a diverse range of health issues such as inflammation [2], bacterial [3] and viral infections [4], and various forms of cancer [5–7]. It is also shown to have potential as a drug to lower cholesterol [8] and treat Alzheimer's disease [9]. Due to these promising studies, berberine is a well-studied molecule. A significant problem with berberine is that upon photoexcitation to its first triplet state, it can react with molecular oxygen to form cytotoxic singlet oxygen [10–15]. As berberine is commonly applied to the skin for various treatments, it will be exposed to ultraviolet radiation (280 – 380 nm). Due to this, the photochemistry of the berberine cation has been well studied in the condensed phase. As berberine contains an iminium salt, it is able to react with electron donating solvents, such as alcohols, upon

irradiation with ultraviolet light [10, 12, 13, 15–19]. The photoexcited iminium cation, in a singlet state, participates in single electron transfer (SET) with the donor solvent, generating a neutral iminium radical and a solvent radical cation [16–19] as shown in Scheme 5.3. In the case of berberine, this generates a neutral berberine radical that can further react with the solvent, resulting in addition of a solvent molecule to the carbon alpha to the tertiary amine (labeled 8 in Figure 5.1). But the primary photoproducts, and their fate, of berberine are not known. Due to this interesting and well-known photochemistry, berberine is a suitable candidate molecule to benchmark and expand the single droplet desorption mass spectrometry technique.

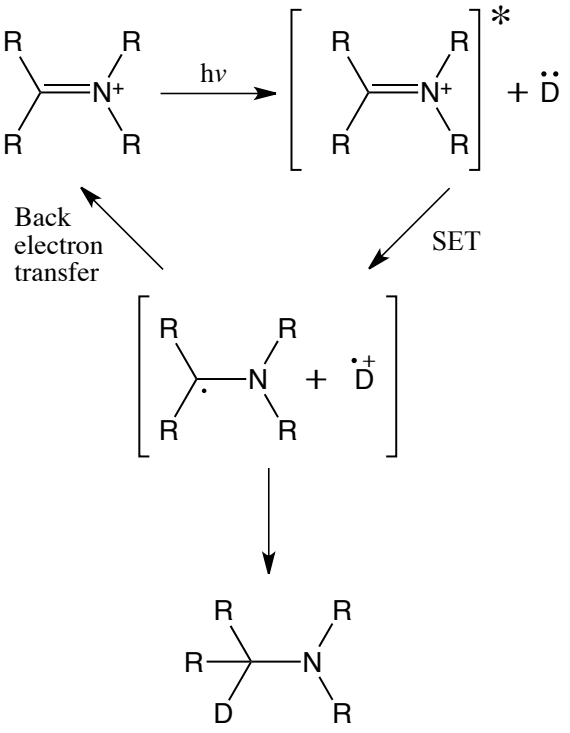

Scheme 5.3

This chapter describes the application of single droplet desorption mass spectrometry to probe the photochemistry of the berberine cation. The experimental arrangement used throughout this chapter is outlined, as well as comparison experiments with bulk condensed-phase and gas phase photochemical measurements. The photochemistry and photophysics of the berberine cation in methanol is investigated in single microdroplets using pulsed laser irradiation. Photoproducts are assigned using previous literature as a guide. The results are compared to both condensed-phase and gas phase photolysis measurements. Wavelength dependence of the photoproducts is also discussed.

5.2 Single droplet and bulk-phase studies

5.2.1 Experimental

Bulk liquid-phase photolysis studies were performed using 100 μM berberine chloride solutions in both methanol and ethanol, both solutions contain 1% v/v water. The solutions were then transferred to 1 cm pathlength quartz cuvette and subsequently irradiated for 30 minutes using the 3rd and 4th harmonics (λ = 355, 266 nm) of the pulsed Nd:YAG laser system (Minilite II, Continuum) operating at a frequency of 10 Hz. Each solvent was irradiated, separately, with 355 (1.9 mJ/pulse) and 266 nm (2.5 mJ/pulse) light, with the laser power adjusted to provide an equal number of photons irradiating the sample. Irradiated samples were diluted 10× and analysed using a commercial linear ion trap mass spectrometer with a standard ESI source used to introduce the sample for MS analysis.

Single microdroplet photolysis experiments were performed using the microdroplet generator setup described in Chapter 2. However, a number of modifications are required to interface the single microdroplet generator to the commercial linear quadropole ion trap mass spectrometer (Thermo Fisher Scientific LTQ). Figure 5.2 shows a schematic of the experiment. At the source of the mass spectrometer is a 30 mm cubic chamber (Thorlabs, C6W) that has additional holes drilled to provide additional access ports along the diagonal axis. The extended transfer capillary from the mass spectrometer enters this chamber from the side closest to the mass spectrometer. Located directly opposite the capillary is a stainless steel acupuncture needle mounted on a *x,y,z,* translatable mount allowing full control of the needle's position relative to the capillary. Above the chamber a drop-on-demand microdroplet generator (Microdrop, MDK-130) is also mounted on a *x,y,z* translatable mount. This provides a source of droplets. The stainless steel needle is held at a potential of +2 kV for a short period of time (1 ms) using a high voltage (HV) pulser (DEI, PVX-4140 pulse generator) coupled with a HV power supply (Canberra, Model 30020). As the microdroplet free-falls it comes in contact with the charged needle where it undergoes electrospray desorption with the spray sampled by the mass spectrometer inlet and ultimately introduced into the mass spectrometer where a full mass spectrum is recorded.

The timing of droplet generation and HV pulser is controlled by a digital delay generator (Stanford Research Solutions, DG645) that is triggered from the injection-period TTL-out pulse from the mass spectrometer. The microdroplet generator is then triggered with no delay, while the HV pulse-trigger is delayed to charge the needle 500 μs before the microdroplet comes in contact. In order to synchronise the microdroplet with the pulsed laser system, the laser's flashlamp is pulsed ∼500 μs after droplet generation to ensure the microdroplet is irradiated before desorption.

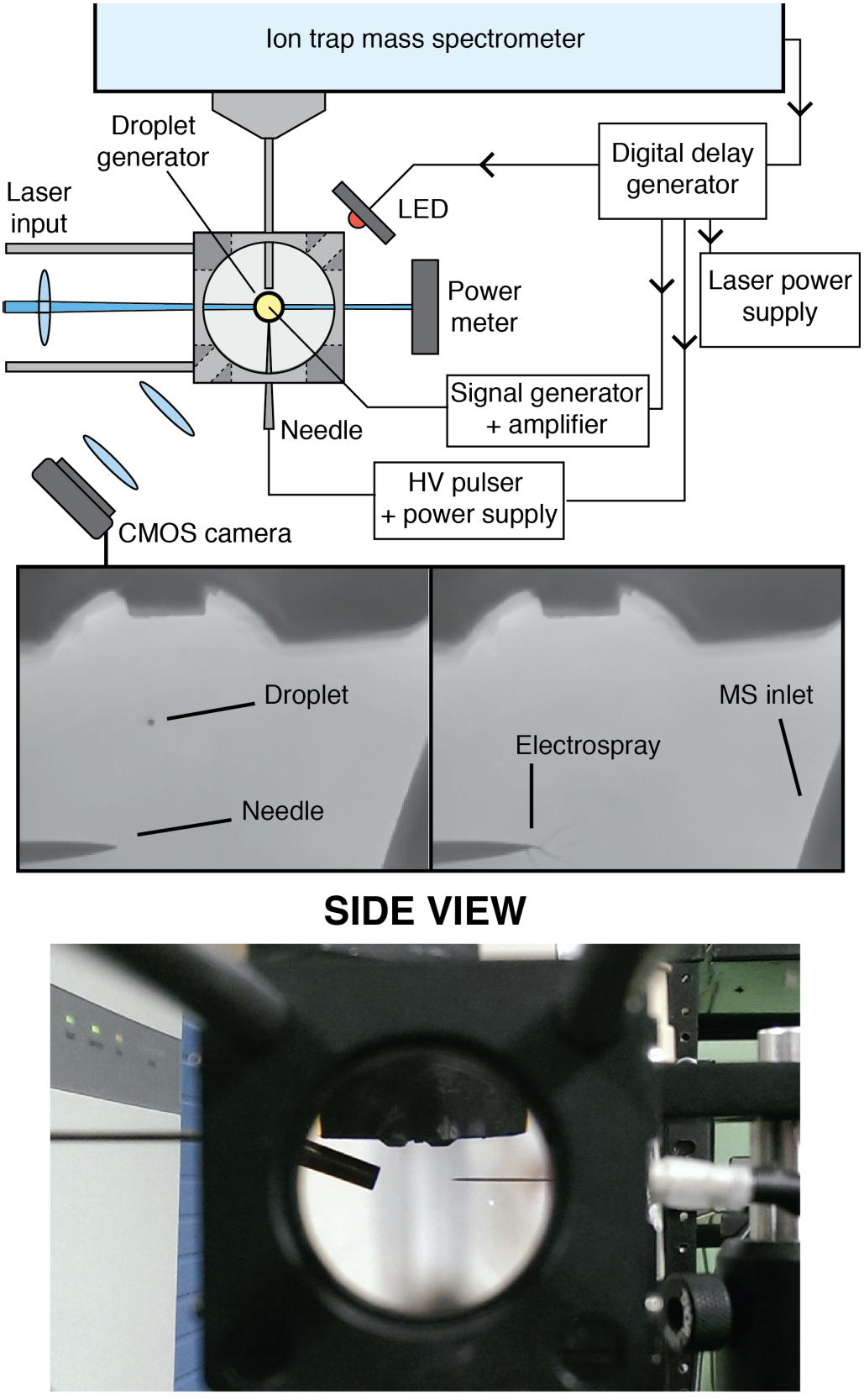

Figure 5.2: Schematic diagram of the single microdroplet mass spectrometry arrangement and a photo showing a side view (along the laser axis). The needle is retracted in the side view photo and is located directly under the droplet generator capillary during operation.

The laser's Q-switch is internally triggered with a set internal delay of 150 μs.

The tip of the needle and microdroplet interaction is monitored using bright-field imaging. This is achieved using a CMOS camera (Thorlabs, DC20023) and LED set up shown along the diagonal axis of the chamber in Figure 5.2. The LED is pulsed at controllable delays after microdroplet generation creating the bright field images that are collected using a compound microscope arrangement coupled to the CMOS camera.

For the single microdroplet photolysis measurements, microdroplets are generated from a solution consisting of 100 μM berberine chloride in methanol with 1% v/v water. The presence of water arises from a $\times$100 dilution of an aqueous 10 mM berberine chloride stock solution and was found to improve microdroplet stability compared to 100% methanol solutions.

5.2.2 Results

Bulk-liquid photolysis

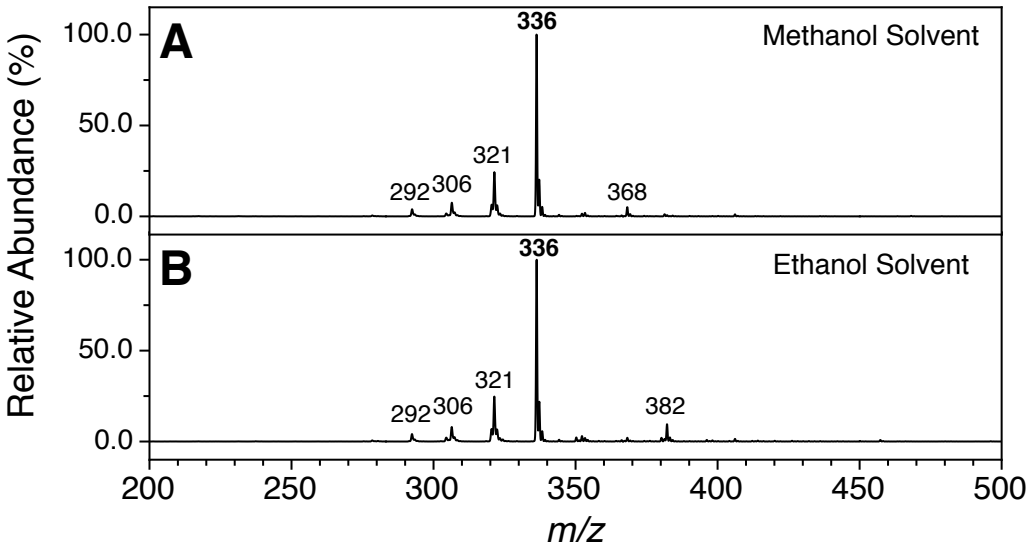

Figure 5.3: Mass spectra of 100 μM berberine methanol (A) and ethanol (B) solutions after 30 minutes of irradiation with pulsed 355 nm laser (1.9 mJ/pulse).

The mass spectra collected from the samples subjected to 355 nm bulk-solution irradiation are shown in Figure 5.3. The main peak observed for both solvents (methanol and ethanol) is the berberine cation at *m/z* 336 (Figure 5.1). Both cases show a photoproduct at a *m/z* greater than the precursor ion, which has been assigned as the addition of a solvent molecule, +32 Da for methanol and +46 Da for ethanol. These photoproducts were subjected to collision induced dissociation (CID), with the resulting product mass spectrum shown in Figure 5.4. This was performed to confirm that these products resulted from the SET and not

solvent clustering in the mass spectrometer. The product mass spectrum shows the photoproduct (m/z 368) is the most abundant species after being collisionally activated (Figure 5.4).

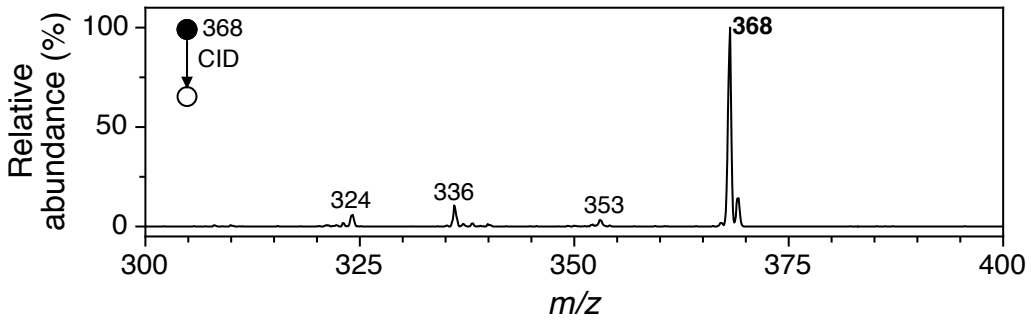

Figure 5.4: CID product mass spectrum from the isolated major photoproduct, m/z 368, from 100 μM berberine solutions irradiated 355 nm light.

For both solvents there are three observed peaks at lower m/z values than the precursor ion, these are photofragmentation products: m/z 321, 306 and 292. The observed photofragmentation product at m/z 321 corresponds to a loss of 15 Da, which is typical of a methyl loss. This methyl loss likely occurs at one of the methoxy functional groups located on the berberine cation (Figure 5.1). Interestingly, this photolysis generates an oxyl radical species, which typically undergoes hydrogen abstraction from the solvent and is not stable for lengths of time here (30 min). Due to this, the photofragmentation product at m/z 321 results from multiple photolysis events. The photofragmentation product m/z 306 corresponds to a neutral loss of 30 Da which may result from either a methoxy loss ($-OCH_3$, -31 Da) followed by hydrogen abstraction (+1 Da) with the solvent or two consecutive methyl losses ($2 \times -CH_3$) followed by the formation of a quinone species. More details of the mechanism will be provided below. The photofragmentation product observed at m/z 292 corresponds to a neutral loss of 44 Da and is assigned as the result of two neutral losses. The first neutral loss is a methoxy group (-31 Da) followed by a hydrogen abstraction (+1 Da) with the solvent, similar to that observed at m/z 306. The second neutral loss is a methyl loss (-15 Da) from the remaining methoxy functional group with the resulting oxyl radical undergoing hydrogen abstraction (+1 Da) to generate a phenol species.

It is noted that the observed products at m/z less than the precursor are not affected by the change in solvent, while those greater than m/z 336 are solvent dependent.

Figure 5.5 shows the mass spectra collected from bulk liquid samples irradiated, for the same duration as the previous measurement, with 266 nm laser light from two solvents, methanol and ethanol. The product distribution is significantly more complex. Similar to the 355 nm case, the berberine cation is observed at m/z

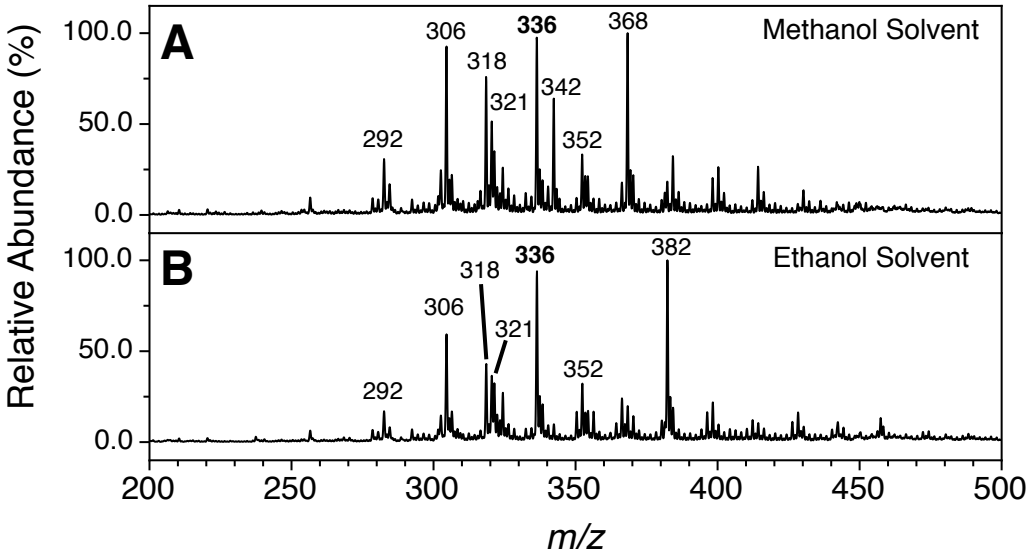

Figure 5.5: Mass spectra of 100 μM berberine methanol (A) and ethanol (B) solutions after 30 minutes of irradiation with pulsed 266 nm laser (2.5 mJ/pulse). The Berberine precursor m/z (336) is shown in bold.

336, but is no longer the most abundant peak. In both cases, the solvent addition photoproduct observed at m/z 368 and 382 for methanol and ethanol respectively, is the most abundant peak. Furthermore, there is an increase in the number of photoproduct peaks observed at m/z values significantly greater than the precursor ion, which may point to radical propagation chemistry. Similarly, the number of photofragmentation products has also increased, with a new product observed at m/z 318. As each photoproduct still contains a chromophore, subsequent photochemistry complicates the analysis. The single droplet experiments, shown next, attempt to intercept the first photochemical stages of this photochemistry.

Single microdroplet desorption mass spectrometry

An average of 200 single microdroplet mass spectra is shown in Figure 5.6 for two cases. The first panel, labeled A, is from single free falling microdroplets with no laser irradiation. The only major peak observed is at m/z 336 and corresponds to the berberine cation (Figure 5.1). When the higher mass region is expanded $\times$20, shown in red, there are minor peaks recorded in the background. Panel B shows the average of 200 single microdroplet mass spectra that have been irradiated with a single 355 nm pulse prior to the desorption process. When the higher mass region is magnified there are new products apparent at higher m/z ratios (above m/z 336). The most abundant new product is m/z 352, which was observed in small amounts in the non-irradiated spectrum. This product appears more abundant when the droplet is irradiated, but this increase is due to a larger decrease in the total ion count as the precursor ion reacts with solvent causing the relative abundance of m/z

352 to increase. The difference spectrum between laser on (B) and laser off (A), is shown in the bottom panel of Figure 5.6. There is a noticeable negative peak at m/z 352 showing there is a net decrease of this species when the microdroplet is irradiated.

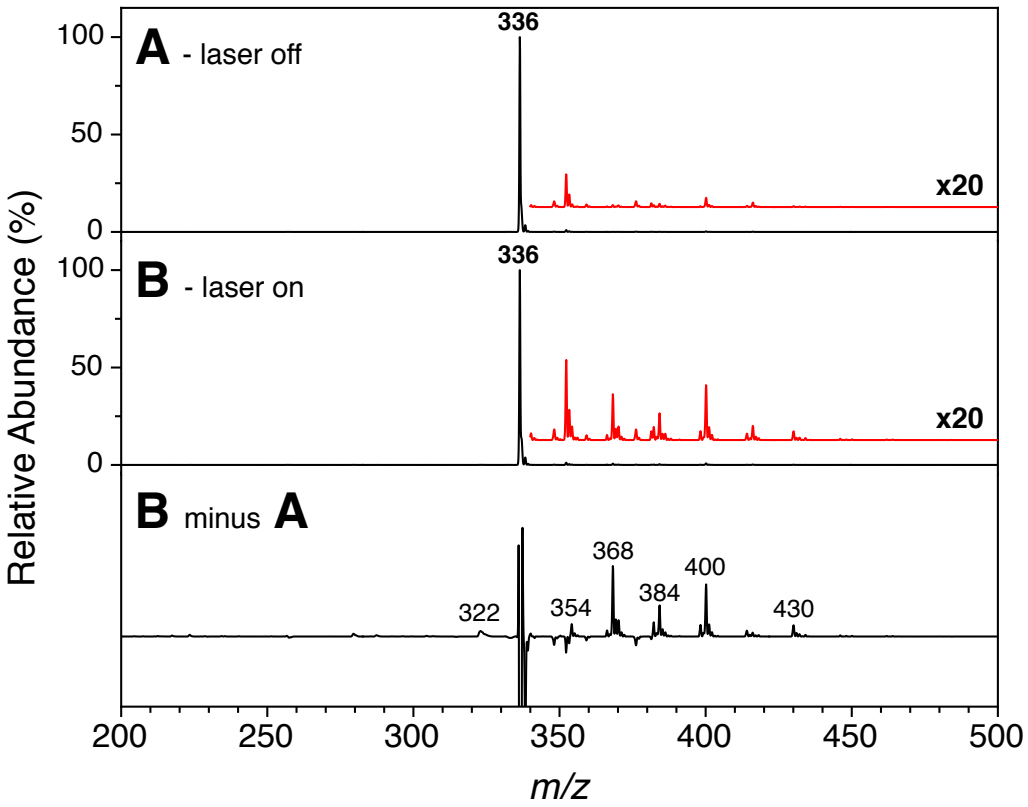

Figure 5.6: The average mass spectra collected from 200 single methanol microdroplets containing 100 μM berberine chloride. (A) Resulting mass spectrum from droplets with no laser irradiation prior to desorption. (B) Resulting mass spectrum from droplets that are irradiated with 355 nm light prior to desorption. All the masses above m/z 340 have been magnified by $\times$20 in red. Panel B minus A shows the difference between the two mass spectra, all products above the base line represent photodependent products, while anything below the base line represents a photodependent loss.

The difference spectrum (Figure 5.6, B minus A) shows a large negative peak at m/z 336, corresponding to photodepletion of the berberine cation. It is noted that the positive peaks observed $\pm$ ~1 Da of m/z 336 are due to the mass subtraction noise from this large signal. A major photoproduct observed is at m/z 368, 32 Da higher than the berberine cation (m/z 336), and similarly to the bulk-phase study, is assigned as a solvent addition (+31 Da, +1 Da). There is also a photoproduct observed at m/z 400 (+64 Da) that is assigned as the second MeOH addition. While the photoproduct at m/z 354 (+18 Da) is assigned as the addition of a hydroxyl group (+17 Da) to a neutral berberine species following electron transfer chemistry that subsequently undergoes protonation at the amine (+1 Da). The

photoproduct at m/z 430 is 30 Da greater than m/z 400 and does not follow the +32 Da pattern. Similarly, the photoproduct observed at m/z 384 is 30 Da greater than the photoproduct at m/z 354. These assignments require more consideration and are discussed later. The only photofragmentation product observed (< 336 m/z) is at m/z 322 and is assigned as the loss of a methyl group (-15 Da) from one of the methoxy groups forming an oxyl radical, which abstracts a hydrogen atom (+1 Da) from the solvent generating a phenol. These photoproducts and their assignments will be further discussed below in section 5.2.3.

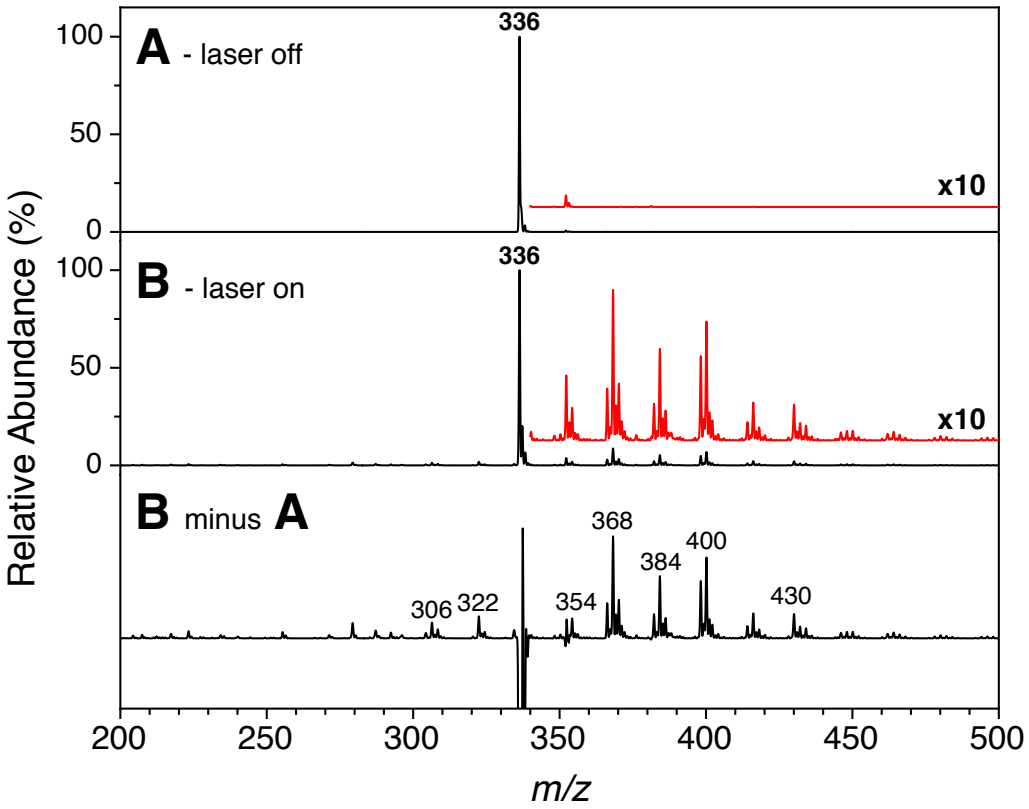

Figure 5.7: The average mass spectra collected from 200 single microdroplets. (A) The resulting average mass spectrum from droplets with no laser irradiation prior to desorption. (B) Average mass spectrum from droplets irradiated with 266 nm light prior to desorption. All the masses above m/z 340 have been magnified by $\times 10$ in red. Panel B minus A is the difference between the two spectra, all products above the base line represent photodependent products, while anything below the base line represents a photodependent loss.

Single microdroplets were also irradiated with the $\lambda = 266$ nm (4^{th} harmonic of the pulsed Nd:YAG laser system) with the product mass spectra shown in Figure 5.7. The laser off spectrum (A) is nearly identical to the previous laser off spectrum (Figure 5.6). When the microdroplets are irradiated prior to desorption the same photoproducts as the 355 nm case are observed, but in higher abundance, with additional photoproducts at m/z greater than 430 being detected. Much like the 355 nm experiment, the observed photoproducts are assigned as combinations of solvent

and hydroxyl additions, and the photofragmentation products due to methyl loss and subsequent H addition. The major difference between the two laser wavelengths is that the higher energy irradiation (λ = 266 nm) generates higher orders of methoxylation as photoproducts are measured at higher m/z ratios with groups of peaks observed at m/z 464 and 496, that have been assigned as the 4th and 5th solvent addition, respectively.

To confirm that the photoproducts measured are due to consecutive solvent additions, the measurement was performed using a 100 μM berberine chloride solution made up with 50:50 methanol:methanol-d_3 (CD_3OH). The difference spectrum (laser on - laser off) is shown in Figure 5.8. When methanol-d_3 is the solvent there are new photoproducts observed with the most noticeable being the photoproduct at m/z 371 (+35 Da) now accompanying the photoproduct at m/z 368 (+32 Da). This has been assigned as the addition of CD_3OH. Similarly, there is a new photoproduct observed at m/z 355 (+19 Da), 1 Da greater than the hydroxyl photoproduct at m/z 354, which is assigned as the addition of a –OD group. It is noted that while the addition of two methanol-d_0 units is observed at m/z 400 (+64 Da) and the addition of one methanol-d_0 and one methanol-d_3 (+67 Da) is observed at m/z 403, the addition of two methanol-d_3 units (+70 Da) is not observed at m/z 406 which may provide insight into how the solvent is added to the berberine molecule. This result is discussed later in section 5.2.3

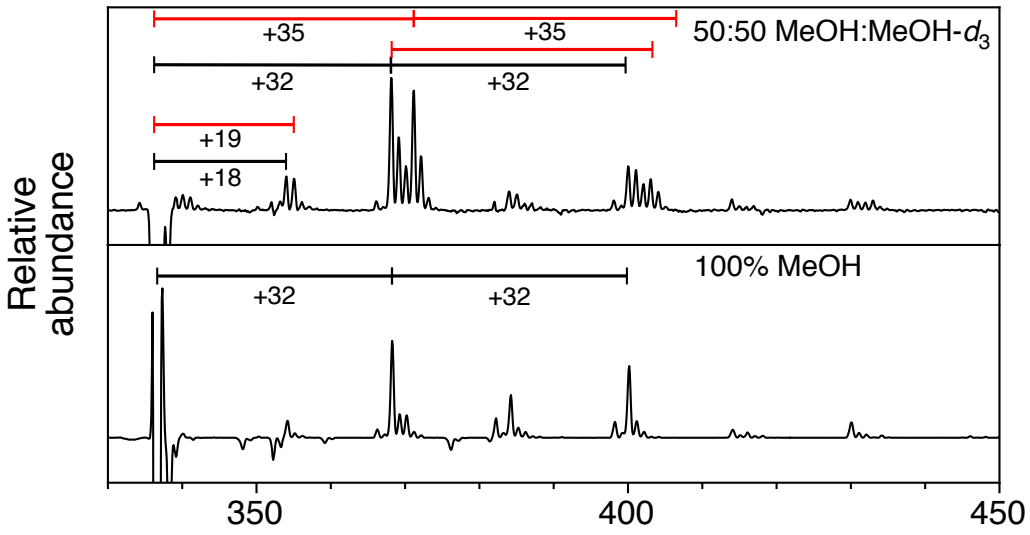

Figure 5.8: (Top) Difference spectrum from single microdroplets containing 100 μM berberine chloride in a solution of 50:50 methanol:methanol-d_3. (Bottom) Difference spectrum from microdroplets generated from a 100 μM berberine solution containing no methanol-d_3, previously shown in Fig. 5.6. The microdroplets have been irradiated with 355 nm laser light prior to desorption.

To ensure this reaction was purely between the berberine cation and an electron donating solvent, the experiment was also performed in droplets of acetonitrile. No

photoproducts were observed when using acetonitrile as the solvent, under similar laser conditions, confirming that the SET depends on the presence of electron-donating alcohol solvents.

Power dependence

To further probe the photophysics of the berberine cation, the power dependence of the major photoproduct m/z 368 was investigated at both of the previously used laser wavelengths. Power dependence of the main photoproduct, m/z 368, was investigated by plotting the photoproduct yield, where the yield is the peak area normalized to the total ion count, as the laser power was varied. This was performed to give insight into whether this reaction was a single or multiphoton process. Figure 5.9 shows the power dependence of the photoproduct yield of m/z 368 collected from microdroplets irradiated with 355 nm photons. The data generally tracks with a linear trend at lower laser powers, but as it reaches higher laser powers the yield rolls over, suggesting that the process is becoming saturated. This initial linear trend shows that the reaction is likely to be dominated by single-photon mediated processes with 355 nm photons (<∼5 mW).

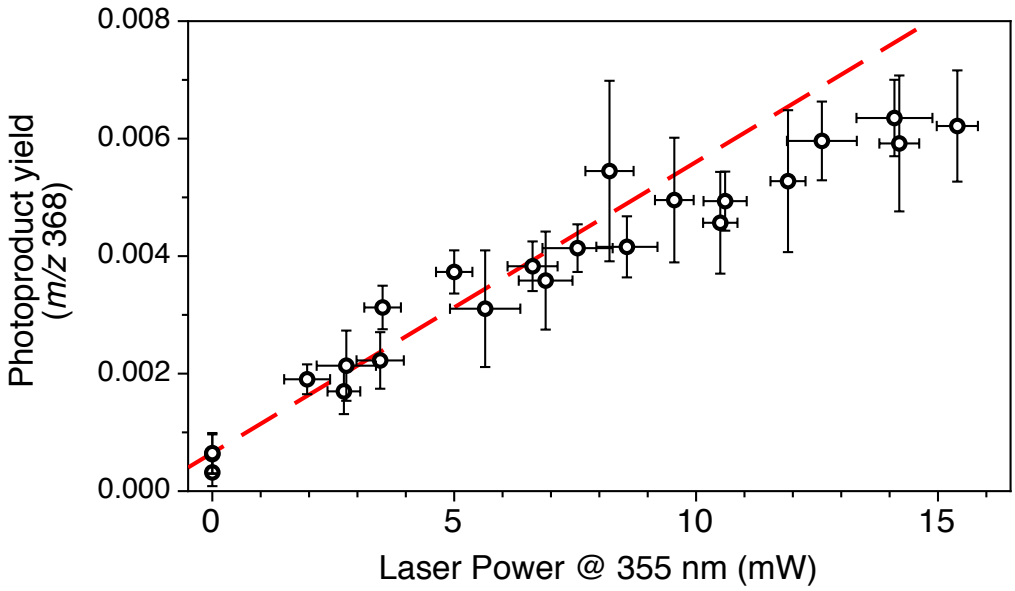

Figure 5.9: Power dependence of the photoproduct at m/z 368 when irradiated with 355 nm laser light.

The same measurement was performed with $\lambda = 266$ nm laser with the power dependence of photoproduct m/z 368 shown in Figure 5.10. It is noticeable that these data do not follow the linear trend that was observed at lower powers when irradiated with 355 nm photons. While these data follow a non-linear trend at lower powers, a roll over at higher powers similar to the 355 nm data is observed.

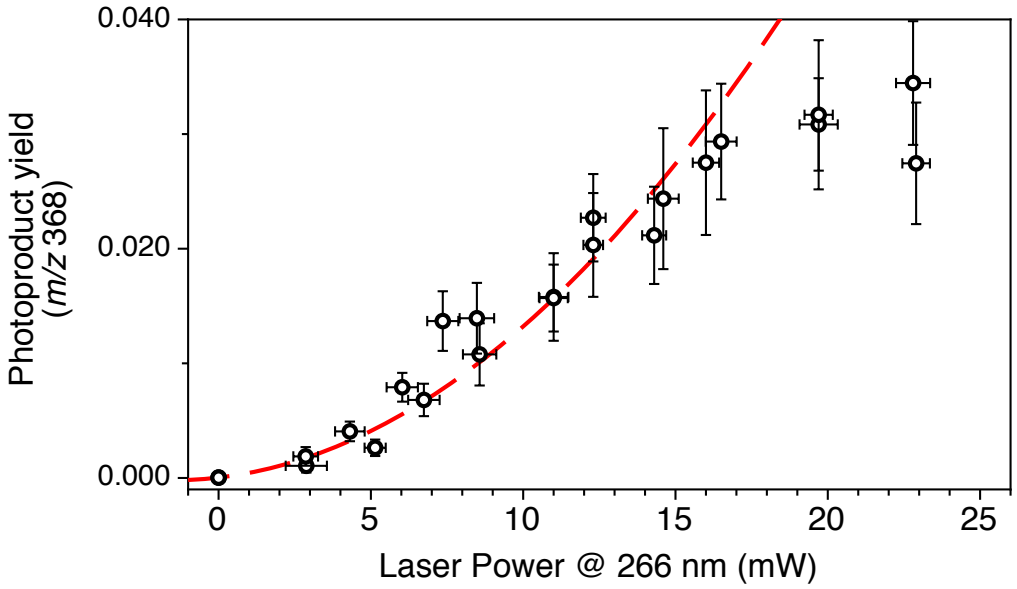

Figure 5.10: Power dependence of the photoproduct at m/z 368 when irradiated with 266 nm laser light.

Single microdroplet photodissociation action spectroscopy

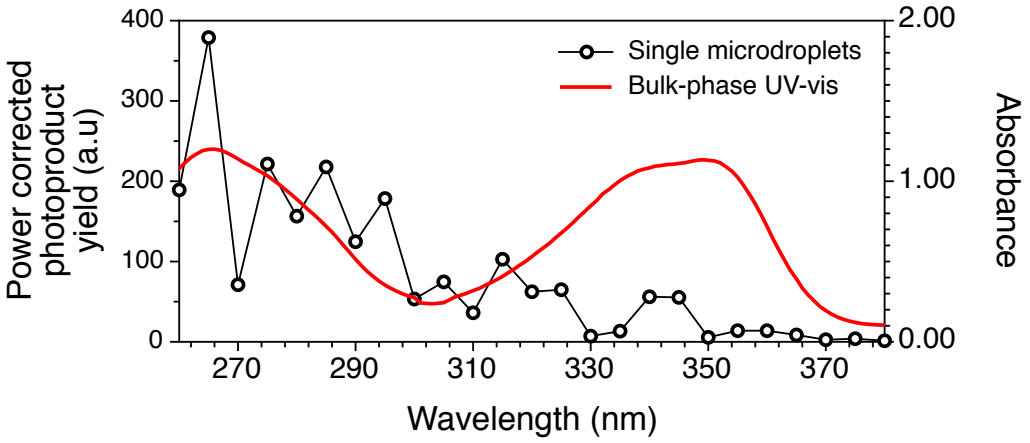

Figure 5.11: Wavelength dependence of the total photoproduct yield (Black) compared to the bulk condensed-phase absorption spectrum (Red).

The wavelength dependence of the total photoproduct yield was investigated by replacing the fixed frequency pulsed laser system with a tunable OPO laser system, allowing the photolysis wavelength to be scanned. This process requires careful synchronisation of the OPO scanning software, the mass spectrometer software, the OPO laser repetition rate and droplet generation and is rather challenging, but the scan in Figure 5.11 provides first evidence of a solution-phase action spectrum. The yield of all photoproducts (>360 m/z) was measured at various wavelengths over the 260 – 380 nm region, as shown in Figure 5.11. As the spectrum shows, there is a gradual increase in the photoproduct yield as the photolysis wavelength is tuned shorter, with an onset occurring in tandem with the observed increase

in absorbance at ∼300 nm. This is compared to the optical absorption spectrum from a 100 μM berberine solution in methanol, in red (Figure 5.11), shows that the absorbance at both 355 and 266 nm is high (1.02 at 355 nm and 1.20 at 266 nm) and it absorbs >90% of the light at these wavelengths. This provides some insight into the fate of photo excited berberine molecules at $\lambda = 355$ nm the absorption should be very strong, as shown in Fig 5.11, but the amount of photoproducts is rather low compared to the shorter wavelength. This suggests the dominant relaxation pathway >300 nm proceeds by radiationless processes, as berberine is weakly fluorescent in methanol [15, 20].

5.2.3 Discussion

Analysis of photoproduct assignments

The major photoproduct observed throughout these berberine photolysis studies in methanol solutions is *m/z* 368 that was assigned as the addition of methanol (+32 Da). It is well known that photoexcited iminium salts are able to undergo a single electron transfer (SET) with an electron donating solvent[7, 15–19, 21]. In the case of berberine (ber^+), when photoexcited in an alcohol solvent, SET can occur that generates a neutral berberine radical ($ber^{\cdot}$)(Scheme 5.4) that is then able to react with the solvent resulting in the formation of either a (i) methoxyl ($CH_3O^{\cdot}$, +31 Da) or (ii) methyl alcohol adduct ($C^{\cdot}H_2OH$, +31 Da). The adduct site is most likely the carbon alpha to the tertiary amine (labeled as 8 in Figure 5.1), as the charge of the iminium cation makes this site vulnerable to nucleophilic attacks [22]. In the product mass spectra, the observed mass gain is 32 Da, one Da greater than both of these functional groups. This is accounted for by subsequent protonation of the tertiary amine during the desorption process (+1 Da), as the electron transfer reaction product is neutral and thus required protonation to be detected by mass spectrometry. These reaction steps are initiated by the ber^+ photo excitation. The mechanism is summarised in Scheme 5.4 [4, 17, 19].

$$ber^+ \xrightarrow{h\nu} [ber^+]^* \xrightarrow[CH_3OH]{SET} ber^{\cdot}$$

i) $$\underbrace{ber^{\cdot}}_{336\text{ Da}} \xrightarrow{+CH_3O^{\cdot}} \underbrace{(CH_3O)ber}_{+31 = 367\text{ Da}} \xrightarrow[+H^+]{ESI} \underbrace{(CH_3O)berH^+}_{+1 = 368\text{ Da}}$$

or

ii) $$\underbrace{ber^{\cdot}}_{336\text{ Da}} \xrightarrow{+CH_2OH} \underbrace{(HOCH_2)ber}_{+31 = 367\text{ Da}} \xrightarrow[+H^+]{ESI} \underbrace{(HOCH_2)berH^+}_{+1 = 368\text{ Da}}$$

Scheme 5.4

The second most abundant photoproduct in the single microdroplet desorption photodissociation spectra (Fig. 5.6 and 5.7) occurs at *m/z* 400 and is assigned as the second MeOH addition (+32 Da) to the photoproduct observed at *m/z* 368. Since photoreactions of iminium salts are well-studied [4, 12, 15, 17–19, 21], it is known that a radical cation of the electron-donating molecule is produced from a SET, in this case the methanol radical cation, $CH_3O^{\cdot+}H$. However, in a study on the phototoxicity of the berberine cation by Inbaraj *et al.*, they showed that upon irradiation of the berberine cation in the presence of ethanol, the radical $CH_3^{\cdot}CHOH$ is generated with no oxygen centred radical cation detected by electron paramagnetic resonance spectroscopy (EPR)[15]. In addition to this, when our experiment was performed with 50% methanol-d_3 (CD_3OH) (Figure 5.12) there is no photoproduct observed at *m/z* 406, which is expected to be the second methoxyl-d_3 addition (+ –OCD_3, +34 Da, +H, +1 Da). Although, new photoproducts are observed at *m/z* 403 and 404 showing that there is a second deuterated solvent addition. The lack of a photoproduct at *m/z* 406 suggests that the second deuterated solvent addition occurs selectively as a radical substitution rather than a radical addition, since the radical substitution of d_3-methoxy (–OCD_3) or d_2-methyl alcohol (–CD_2OH) account for the photoproducts at *m/z* 404 and 403, respectively. Since *m/z* 403 is the most abundant of the new photoproducts, coupled with the literature results measuring the carbon-centred alcohol radical in solution, it is likely the second solvent addition occurs as a methyl alcohol adduct (–CH_2OH) and not the methoxy form (–OCH_3).

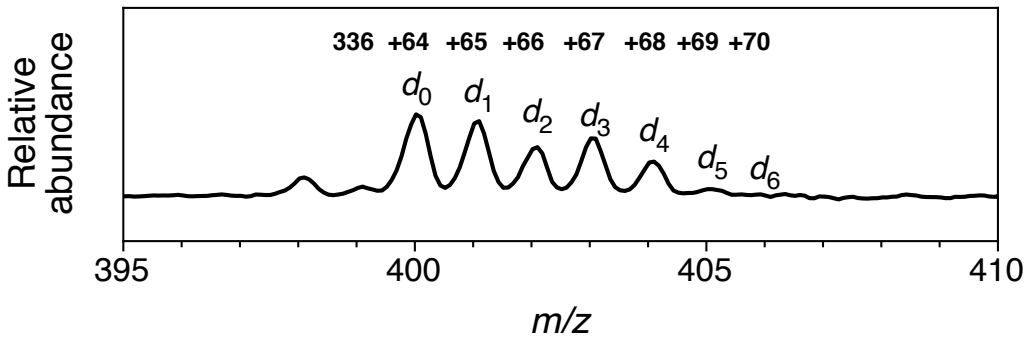

Figure 5.12: Expansion of the mass region where the second solvent photoproducts appear in the difference spectrum collected 50:50 methanol:methanol-d_3 microdroplets.

Hence, the photoproduct at *m/z* 400 is assigned as the radical methyl alcohol addition, (+31 Da), as shown in Scheme 5.5, at the carbon labeled 13 (Figure 5.1) followed by a subsequent hydrogen abstraction from the solvent (+1 Da) to hydrogenate the alpha carbon (13a).

Interestingly, the photoproduct observed at *m/z* 430 was generally assigned as involving a third solvent addition but does not follow the pattern of multiple 32

$$\underbrace{(CH_3O)ber}_{367\ Da} \xrightarrow[+H^+]{C^{\cdot}H_2OH} \underbrace{(HOCH_2)(CH_3O)Hber}_{+31\ +1\ =\ 399\ Da} \xrightarrow[+H^+]{ESI} \underbrace{(HOCH_2)(CH_3O)HberH^+}_{+1\ =\ 400\ Da}$$

or

$$\underbrace{(HOCH_2)ber}_{367\ Da} \xrightarrow[+H^+]{C^{\cdot}H_2OH} \underbrace{(HOCH_2)_2Hber}_{+31\ +1\ =\ 399\ Da} \xrightarrow[+H^+]{ESI} \underbrace{(HOCH_2)_2HberH^+}_{+1\ =\ 400\ Da}$$

Scheme 5.5

Da additions, as it is only 30 Da greater than the photoproduct observed at *m/z* 400. This addition must occur as a radical substitution of a methyl alcohol group (+31 Da), which directly replaces a hydrogen atom (-1 Da). The location of this substitution is unknown but possibly occurs on one of the remaining aromatic rings in the molecule.

Between the observed solvent additions photoproducts there is also a repeating pattern of photoproducts observed at *m/z* 354 and 384. This pattern follows +30 additions, with the exception of the first photoproduct at *m/z* 354 that is 18 Da greater than the precursor ion and has been assigned as the addition of a hydroxyl group (+17 Da), followed by protonation (+1 Da). This hydroxyl addition, similar to the original solvent addition, likely occurs at carbon 8.

The next photoproduct in this sequence is *m/z* 384 and corresponds to a mass gain of +30 Da from the previously discussed hydroxyl addition. This product arises from the radical substitution of a methyl alcohol group on the photoproduct at *m/z* 354, similar to that of the product observed at *m/z* 430. This plausibly involves methanol radicals present within the microdroplet after the initial photoreaction.

In the higher energy laser photolysis (λ = 266 nm) data, there is an increase in the number of photoproducts at *m/z* values greater than 430. These values follow the pattern of +30/32 mass gains and correspond to consecutive solvent additions.

Most of the photoproducts discussed have been observed *m/z* values greater than the precursor ion but there is also a noticeable product observed at *m/z* 322 in both microdroplet studies, with an additional product at *m/z* 306 in the 266 nm data. The first product at *m/z* 322 ultimately corresponds to a loss of 14 Da and has been assigned as the loss of a methyl group (-15 Da) from cleavage at one of the native methoxy groups labeled 9 and 10 in Figure 5.1, and then the remaining oxyl radical abstracts a hydrogen atom (+1 Da) from the solvent generating an alcohol. Similarly the product at *m/z* 306 corresponds to a loss of 30 Da, which corresponds to the loss of a native methoxy group (-31 Da) that forms a phenoxy radical that then undergoes hydrogen abstraction from the solvent (+1 Da).

These postulated assignments are supported by measured spectra and literature studies, but it is important to note that due to the nature of mass spectrometry, only

the mass to charge ratio is measured and identifying isomer specific photoproducts is challenging. As this measurement is performed on an ion trap mass spectrometer additional instrumentation, such as further gas-phase reactions within the ion trap, could be used to identify photoproducts. Nonetheless, the observed mass-to-charge ratios are shown to result from various combinations of methoxyl, hydroxyl and methyl alcohol additions as well as methyl and methoxyl losses. Single droplet photodissociation spectrometry provides new mechanistic insight into photochemical mechanisms.

When comparing the bulk with the single droplet irradiation studies, the observed photoproducts are similar in both cases, with the bulk studies showing higher orders of solvent addition. Additionally, other minor photoproducts were observed that were not present in the single droplet study. These differences in observed photoproducts are due to the bulk sample undergoing continued irradiation from multiple laser pulses. This leads to the photoproducts generated from initial laser pulses to be repeatedly irradiated which can obscure data. This makes determining photoproducts that arise from single photolysis events challenging. The single microdroplet photolysis experiments showed that the photoproducts from single photolysis events could be clearly measured as each single droplet is exposed to only one laser pulse.

The goal of this study is to investigated the photochemistry and photophysics of a complex system as a method for benchmarking this newly developed single droplet mass spectrometry technique. This has been achieved using the berberine cation as a case study.

Wavelength Comparison

Comparing the two laser photolysis wavelengths used through this study, the higher energy irradiation (λ = 266 nm) consistently produced a larger number of photoproducts and greater photoproduct yields. This result is likely due to the berberine cation also undergoing a photoionisation process, in addition to the SET process, when photoexcited with 266 nm light, which generates a berberine radical dication as well as a solvated electron [12, 21]. This will lead to an increased concentration of radical berberine species, as there are two pathways to generate berberine radicals, which ultimately results in an increased concentration of solvent radicals in solution. A previous study by Cheng *et al.* has shown that this photoionisation is highly efficient [21], explaining the observed increase in photoproduct yield as well as the increase in observed radical substitutions (+30 Da). Although this explains the increase in photoproduct yield, the study showed that the photoionisation followed a linear trend in regards to laser power, instead of the non-linear power dependence measured and presented in this chapter.

This discrepancy could be due to photoproduct generation proceeding by different electron transfer processes, or that the additional solvated electron is driving rampant radical propagation chemistry within the microdroplets.

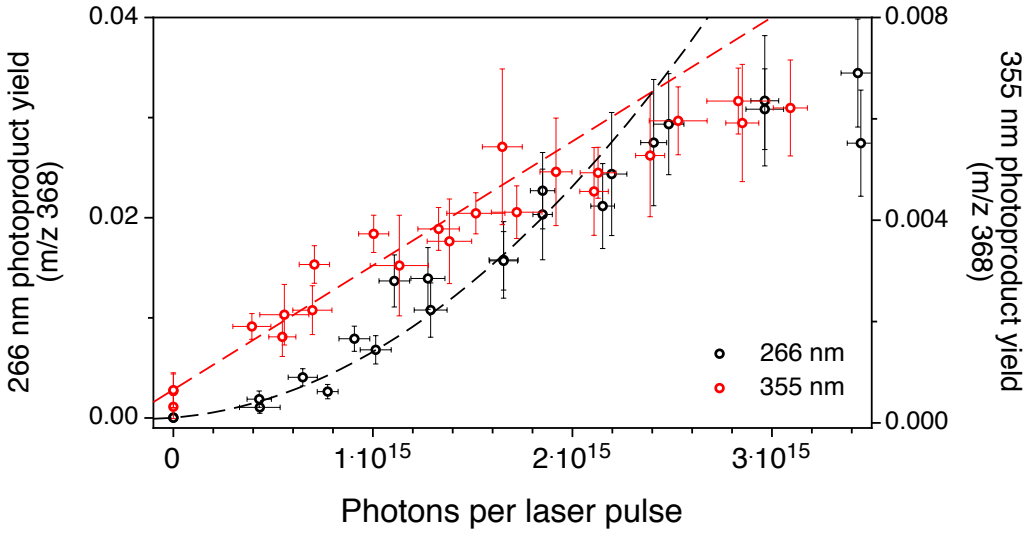

Figure 5.13: Power dependence of the photoproduct at m/z 368 in terms of photons of pulse when irradiated by 355 (red) and 266 (black) nm laser light.

Interestingly, both wavelengths exhibit a roll over in photoproduct yield at higher laser powers. When both data sets are compared in terms of photons per laser pulse, as shown in Figure 5.13, it is apparent that both data sets roll over at ~2 x 10^{15} photons per pulse. This suggests that the reaction has reached a saturation point where every molecule within the microdroplet has been irradiated. This is possible with each single microdroplet containing ~3 x 10^{9} berberine molecules, which is a million times smaller than the number of photons per laser pulse.

Wavelength dependence

As shown in Figure 5.11, there is an increase in the photoproduct yield when the photolysis laser wavelength is tuned shorter than ~300 nm. This is primarily due to an increase in berberine radical generation as the photoionisation process is able to occur. It is noted that although the optical arrangement was unchanged between each photolysis wavelength, as the OPO wavelength is scanned differences in beam profile and effective focal length of the input lens can impact on the number of photons that interact with the droplet. Since both fixed frequency experiments experienced the saturation effect at the same number of photons per pulse, this provides reasonable justification that these factors had little effect on the resulting spectrum. Due to this, the assumption that these spectra are interpretable, once corrected for laser power, is made. The noticeable increase in photoproduct yield as the laser is tuned to shorter wavelengths appears to coincide with the increase

in optical absorption at ∼290 nm, with a λ_{max} at ∼265 nm. This increase in photoproduct yield is a result of the photon energy surpassing the photoionisation threshold for the berberine cation. By including a tunable laser system into the experimental setup the onset of the photoionisation of the berberine cation has been observed.

5.3 Gas-phase studies

5.3.1 Introduction

As previously shown, unravelling the mechanism of liquid phase photochemistry is complex. Often gas-phase analysis, where molecules are free from solvent, is utilised as a useful comparison. Also as will be shown, the gas-phase photochemistry of the berberine cation is relatively simple to rationalise and this illustrates the complexity of solution-phase photochemistry. This further highlights the need for new techniques to provide insights into solution phase photochemistry.

5.3.2 Experimental

Gas phase photochemistry is investigated using a modified commercial linear ion trap mass spectrometer (Thermo Fisher Scientific LTQ) coupled with a standard ESI source. A schematic of the experimental setup is shown in Figure 5.14. Typical operating parameters: Source voltage 4 kV, low mass cut-off 90 *m/z*, q-parameter of 0.25, isolation time of 120 ms for photodissociation or 200 ms for collision induced dissociation (CID) and normalised collision energies of 20-30 (arb. units). The backside of the mass spectrometer is modified to include a quartz window, allowing laser light to be directed through the ion trap. A methanol solution containing 10 μM berberine chloride is subjected to electrospray and berberine cations are mass selected and isolated. Following isolation the contents of the ion trap are irradiated with a single UV laser pulse ($\lambda = 355$ or 266 nm). The laser power at each wavelength is adjusted to provide equal photon density. Once irradiated, the ions are scanned out of the trap, generating a product mass spectrum revealing any photoproducts [23–27]. Photochemistry is investigated for both 355 and 266 nm irradiation.

5.3.3 Results

Product mass spectra collected from the gas phase UV irradiation of the berberine cation at $\lambda = 355$ and 266 nm are shown in Figure 5.15. After irradiation there are large yields of photoproducts at both laser wavelengths. Recalling that photodissociation occurs after *m/z* 336 is isolated within the ion trap, all peaks

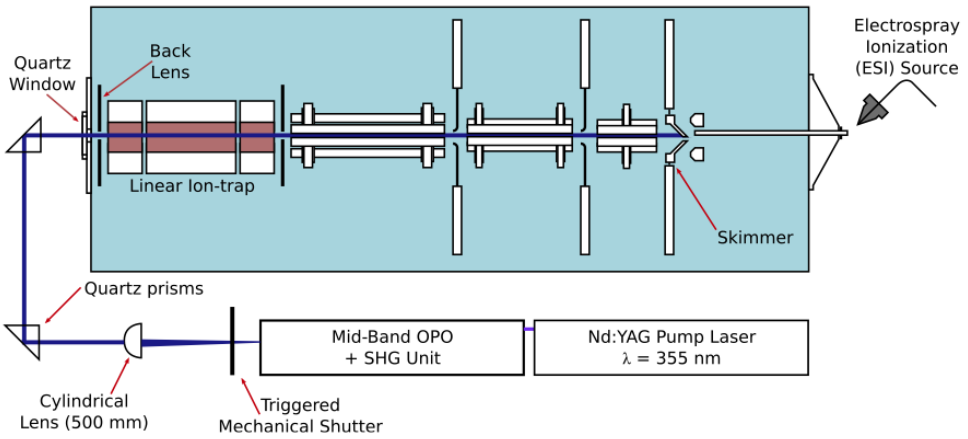

Figure 5.14: Schematic of the modified LTQ mass spectrometer coupled with a tuneable OPO laser. The quartz window on the backside allows isolated gas-phase ions to be irradiated. Figure reproduced from Ref [23]

other than m/z 336 arise from laser excitation. When comparing the two spectra it is apparent that both wavelengths generate a similar distribution of photoproducts. The most noticeable difference is the abundance of the precursor ion (m/z 336) as it is the most abundant species for 266 nm photodissociation, while the photoproduct located at m/z 279 is most abundant for the 355 nm case.

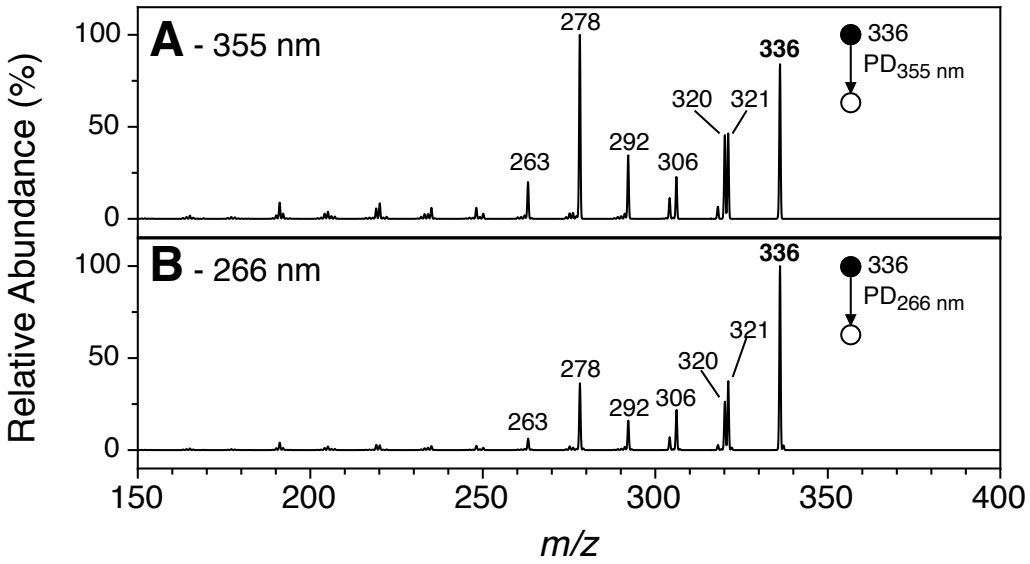

Figure 5.15: Measured mass spectra after irradiating the gas-phase berberine cation (336 m/z) with 355 nm (A) and 266 nm (B) laser light.

In order to elucidate the photoproduct identities, and link these photoproduct pathways, the major photoproducts were isolated and subsequently subjected to collision induced dissociation (CID). The CID product mass spectra from the major photoproducts are shown in Figure 5.16.

Two distinct fragmentation pathways were observed in the CID product mass

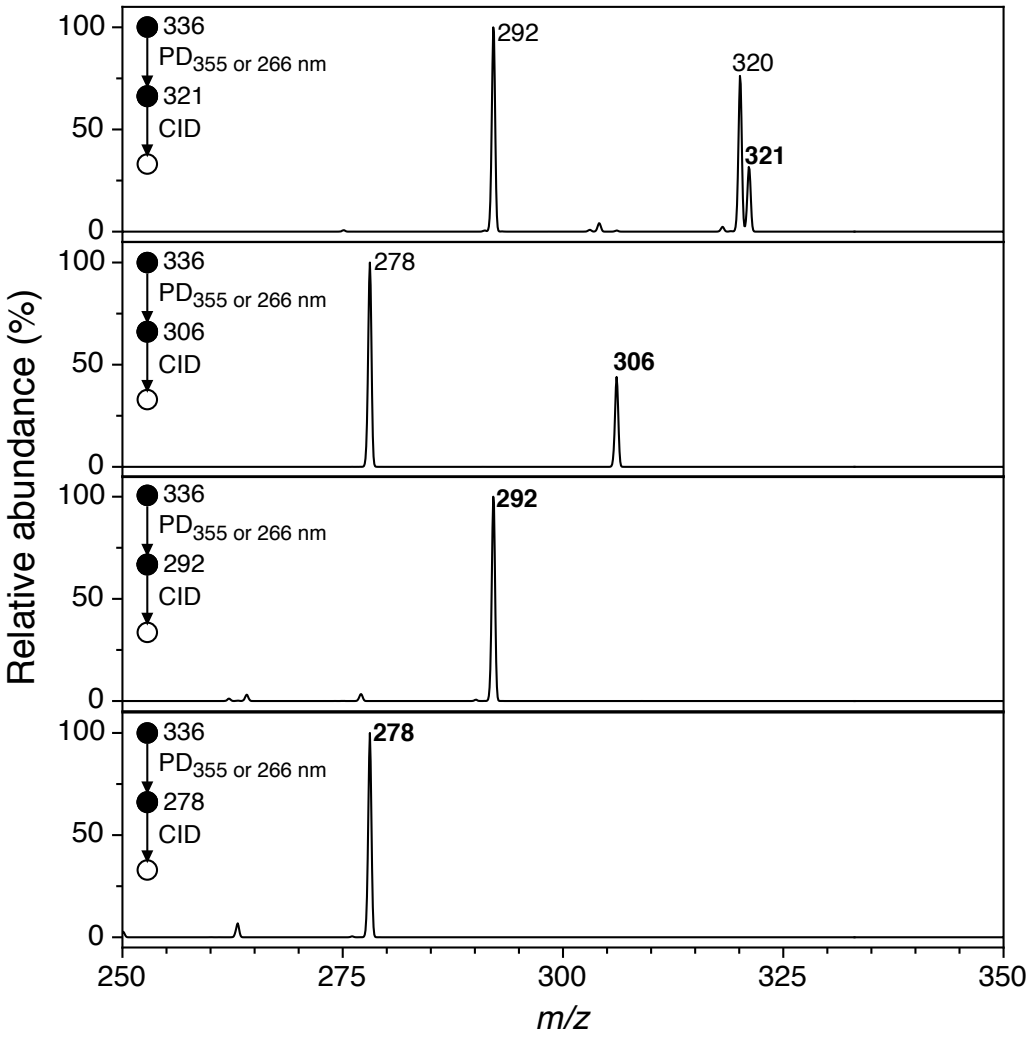

Figure 5.16: Product mass spectra from the observed major gas-phase photoproducts of berberine (m/z 336).

spectra. The first pathway was observed in the photoproduct *m/z* 321 CID product mass spectra, where two major fragmentation products were observed at *m/z* 320 (-1 Da) and 292 (-29 Da), with minor products at *m/z* 304 and 306 (Fig. 5.16). Additionally, the photoproduct at *m/z* 292 was subjected to CID and was found to have no major fragmentation products. This suggests that the photoproducts observed at *m/z* 320 and 292 are generated through the same fragmentation pathway emanating from the *m/z* 321 photoproduct and that the final product of this pathway, *m/z* 292, is quite stable.

A second fragmentation pathway was observed when the photoproduct *m/z* 306 underwent CID. A single fragmentation product was observed at *m/z* 278 (-28 Da), which is the most abundant photoproduct for both photolysis wavelengths. When the photoproduct at *m/z* 278 was subjected to CID a fragmentation product was observed at *m/z* 263. This suggests that the photoproducts at *m/z* 306, 278 and 263 belong to the second fragmentation pathway that starts with product at *m/z* 321. Postulated assignments for the major photoproducts are discussed in the following section.

5.3.4 Discussion

The photoproducts observed in the gas phase photodissociation of berberine follow two key decomposition pathways that are known for dimethoxy and *o*-methoxyphenol aromatic compounds and have been well-studied in the gas phase [28, 29]. This implies that the dominant decomposition pathways of berberine are focused at the methoxy functional groups.

The first pathway, shown in Scheme 5.6, leads to the formation of a stable phenol type structure on the isoquinoline backbone. Following the initial methyl loss ($^{\cdot}CH_3$) from a methoxy group, a hydrogen transfer from the adjacent methoxy group to the oxyl radical leads to formation of an alcohol and a carbon centred radical on the adjacent methoxy group. This radical then follows a 1,3 aryl rearrangement, to generate a methoxyl radical species, shown in Scheme 5.6. This ultimately forms a formyl group after ejecting a hydrogen atom [28]. Additionally, this may be followed by loss of carbon monoxide (CO) from the formyl group, generating a stable phenol species.

As shown in Scheme 5.7, the second pathway leads to the formation of a quinone species followed by decomposition to finally form a cyclopentadienone structure. This pathway is initiated by the methyl loss from a methoxy group to form an oxyl radical, which transfers an electron from the aromatic ring leading to the formation of a ketone and a radical at the adjacent methoxy containing carbon. This new radical site initiates the second methyl loss leading to the formation of the

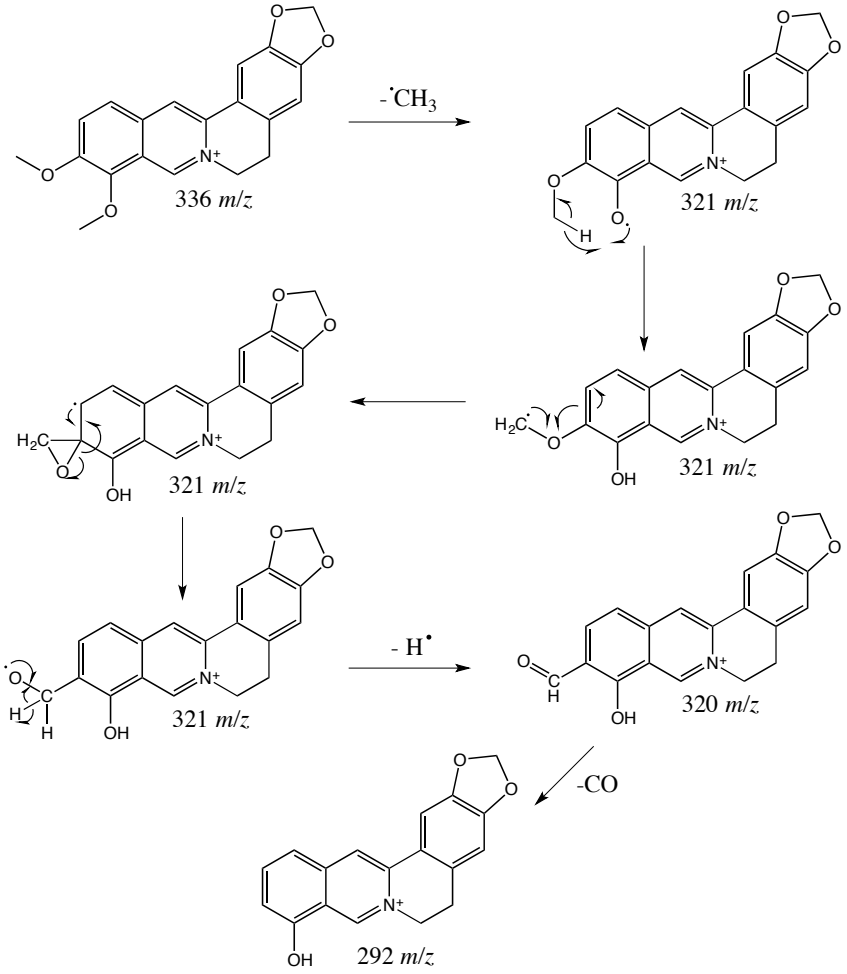

Scheme 5.6

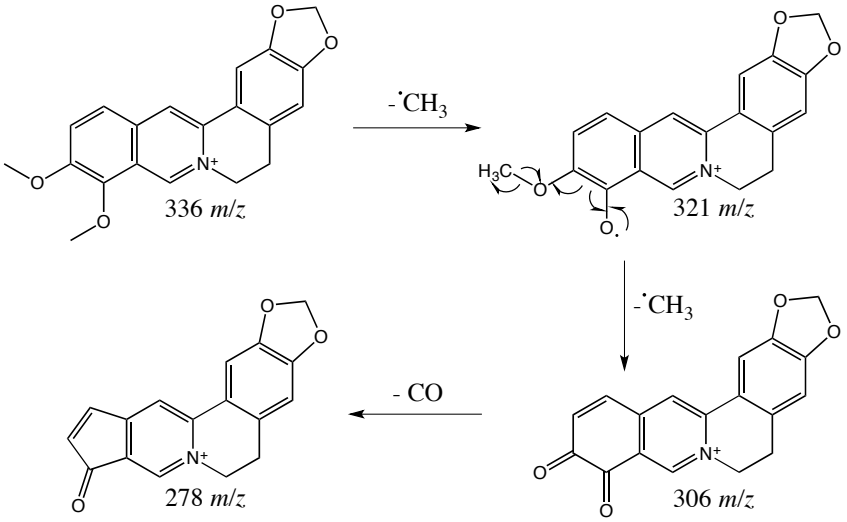

Scheme 5.7

quinone structure [28, 29]. Quinones are known to undergo decomposition at low thermal temperatures, which results in a loss of carbon monoxide to form the final cyclopentadienone structure [30]. When the cyclopentadienone structure (278 m/z) was subjected to CID, a neutral loss of 15 Da was measured, which has not previously been mentioned in literature. As there is no obvious methyl species present within the molecule after all the previous fragmentation, this pathway maybe evidence for more complex ring opening pathways.

5.4 Conclusion

This study has demonstrated that single microdroplet desorption is capable of probing complex condensed-phase photochemistry and photophysics with minimal sample consumption and high throughput. The photoproducts from the single laser pulse irradiation of the berberine cation in single microdroplets of methanol were measured and showed that the observed photoproducts arise from sequential methoxylation reactions. The first methoxylation is initiated by a single electron transfer with the solvent generating the berberine radical, which can further react with the electron donating solvent to generate methoxy berberine and methanol radicals. The higher order methoxylations measured are due to radical driven chemistry mediated by the first methoxylation. Photoproducts were measured using two photolysis wavelengths, 355 and 266 nm, and showed that higher energy irradiation ($\lambda = 266$ nm) generated a greater yield of photoproducts as well as higher orders of methoxylation, due to an additional photodetachment process.

In the case of the lower photon energy irradiation (355 nm), the photoproduct yield followed a linear trend at low laser powers indicative of a single photon process, while the higher photon energy irradiation (266 nm) followed a trend consistent with a multiple photon process. This study also showed that a saturation point was achieved where the yield of photoproducts plateaued for both wavelengths, with the saturation occurring when irradiated with the same photon number density.

Bulk condensed-phase irradiation was performed to compare irradiation techniques in terms of observed photoproducts. This highlights that the bulk irradiation is vastly more complex due to multiple generation photoproducts, compared to the single microdroplet desorption experiment.

Gas phase studies of the berberine cation have shown that the photochemistry is profoundly different to that observed in the single microdroplet and bulk phase studies. While the initial mass spectrum post photodissociation was complex, the major photoproducts followed one of two decomposition pathways characteristic of dimethoxy and *o*-methoxyphenol containing aromatics. This revealed that the photoproducts observed in the gas phase are, perhaps not unexpectedly, profoundly

different from that of single microdroplets and bulk.

These studies have shown that the single microdroplet desorption mass spectrometry technique is suitable for studying the photochemistry and photophysics of condensed phase chemical systems, while conserving sample ($\sim$50 pL at 10^{-4} M per measurement) with high throughput. Compared to bulk condensed-phase irradiation studies, single microdroplet desorption mass spectrometery uses less sample and time, while also providing clearer insight into the fundamental photochemistry and –physics of a system. The gas phase study showed that when independent from a solvent the photochemistry of the berberine cation is vastly different. Also, it showed that gas phase yields are not necessarily indicative of that in the condensed phase and care must be taken when inferring condensed phase photochemical properties from gas phase studies.

5.5 References for Chapter 5

(1) P. J. Tracey, B. S. Vaughn, B. J. Roberts, B. L. Poad and A. J. Trevitt, "Rapid profiling of laser-induced photochemistry in single microdroplets using mass spectrometry", *Analytical Chemistry*, 2014, **86**, 2895–9.

(2) E. Kupeli, M. Kosar, E. Yesilada, K. Husnu and K. H. C. Baser, "A comparative study on the anti-inflammatory, antinociceptive and antipyretic effects of isoquinoline alkaloids from the roots of Turkish Berberis species", *Life Sciences*, 2002, **72**, 645–657.

(3) K. Iwasa, M. Kamigauchi, M. Ueki and M. Taniguchi, "Antibacterial activity and structure-activity relationships of berberine analogs", *European Journal of Medicinal Chemistry*, 1996, **31**, 469–478.

(4) A. Lesnau, J. Hils, G. Pohl, G. Beyer, M. Janka and L. T. T. Hoa, "Antiviral activity of Berberine salts", *Pharmazie*, 1990, **45**, 638–639.

(5) C. L. Kuo, C. C. Chou and B. Y. M. Yung, "Berberine complexes with DNA in the Berberine-induced apoptosis in human leukemic HL-60 cells", *Cancer Letters*, 1995, **93**, 193–200.

(6) S. M. Meeran, S. Katiyar and S. K. Katiyar, "Berberine-induced apoptosis in human prostate cancer cells is initiated by reactive oxygen species generation", *Toxicology and Applied Pharmacology*, 2008, **229**, 33–43.

(7) S. Jantova, S. Letasiova, V. Brezova, L. Cipak and J. Labaj, "Photochemical and phototoxic activity of berberine on murine fibroblast NIH-3T3 and Ehrlich ascites carcinoma cells", *Journal of Photochemistry and Photobiology B-Biology*, 2006, **85**, 163–176.

(8) W. J. Kong, J. Wei, P. Abidi, M. H. Lin, S. Inaba, C. Li, Y. L. Wang, Z. Z. Wang, S. Y. Si, H. N. Pan, S. K. Wang, J. D. Wu, Y. Wang, Z. R. Li, J. W. Liu and J. D. Jiang, "Berberine is a novel cholesterol-lowering drug working through a unique mechanism distinct from statins", *Nature Medicine*, 2004, **10**, 1344–1351.

(9) M. Asai, N. Iwata, A. Yoshikawa, Y. Aizaki, S. Ishiura, T. C. Saido and K. Maruyama, "Berberine alters the processing of Alzheimer's amyloid precursor protein to decrease A beta secretion", *Biochemical and Biophysical Research Communications*, 2007, **352**, 498–502.

(10) L. L. Cheng, M. Wang, M. H. Wu, S. D. Yao, Z. Jiao and S. L. Wang, "Interaction mechanism between berberine and the enzyme lysozyme", *Spectrochimica Acta Part A - Molecular and Biomolecular Spectroscopy*, 2012, **97**, 209–214.

(11) L. L. Cheng, M. Wang, P. Zhao, H. Zhu, R. R. Zhu, X. Y. Sun, S. D. Yao and S. L. Wang, "The examination of berberine excited state by laser flash photolysis", *Spectrochimica Acta Part A - Molecular and Biomolecular Spectroscopy*, 2009, **73**, 268–272.

(12) L. L. Cheng, Y. J. Wang, D. H. Huang, S. D. Yao, G. J. Ding, S. L. Wang and Z. Jiao, "Radiolysis and photolysis studies on active transient species of Berberine", *Spectrochimica Acta Part A - Molecular and Biomolecular Spectroscopy*, 2014, **124**, 670–676.

(13) H. Gorner, Z. Miskolczy, M. Megyesi and L. Biczok, "Photoreduction and Ketone-sensitized Reduction of Alkaloids", *Photochemistry and Photobiology*, 2011, **87**, 284–291.

(14) H. Gorner, Z. Miskolczy, M. Megyesi and L. Biczok, "Photooxidation of alkaloids: Considerable quantum yield enhancement by Rose Bengal-sensitized singlet molecular oxygen generation", *Photochemistry and Photobiology*, 2011, **87**, 1315–1320.

(15) J. J. Inbaraj, B. M. Kukielczak, P. Bilski, S. L. Sandvik and C. F. Chignell, "Photochemistry and photocytotoxicity of alkaloids from Goldenseal (Hydrastis canadensis L.) 1. Berberine", *Chemical Research in Toxicology*, 2001, **14**, 1529–1534.

(16) R. Suau, F. Najera and R. Rico, "Photochemical hydroxymethylation of protoberberine alkaloids. Total synthesis of (+/-)-solidaline", *Tetrahedron Letters*, 1996, **37**, 3575–3578.

(17) U. C. Yoon, S. L. Quillen, P. S. Mariano, R. Swanson, J. L. Stavinoha and E. Bay, "Exploratory and mechanistic aspects of the electron-transfer photochemistry of olefin-N-heteroaromatic cation systems", *Journal of the American Chemical Society*, 1983, **105**, 1204–1218.

(18) P. S. Mariano, "Electron-transfer mechanisms in photochemical-transformations of iminium salts", *Accounts of Chemical Research*, 1983, **16**, 130–137.

(19) K. Ohga, U. C. Yoon and P. S. Mariano, "Exploratory and mechanistic studies of the electron-transfer-initiated photoaddition reactions of allylsilane iminium salt systems", *Journal of Organic Chemistry*, 1984, **49**, 213–219.

(20) M. S. Diaz, M. L. Freile and M. I. Gutierrez, "Solvent effect on the UV/Vis absorption and fluorescence spectroscopic properties of berberine", *Photochemical & Photobiological Science*, 2009, **8**, 970–974.

(21) L. L. Cheng, M. Wang, H. Zhu, K. Li, R. R. Zhu, X. Y. Sun, S. D. Yao, Q. S. Wu and S. L. Wang, "Characterization of the transient species generated by the photoionization of Berberine: A laser flash photolysis study", *Spectrochimica Acta Part A - Molecular and Biomolecular Spectroscopy*, 2009, **73**, 955–959.

(22) L. Grycova, J. Dostal and R. Marek, "Quaternary protoberberine alkaloids", *Phytochemistry*, 2007, **68**, 150–175.

(23) C. S. Hansen, B. B. Kirk, S. J. Blanksby, R. A. J. O'Hair and A. J. Trevitt, "UV Photodissociation Action Spectroscopy of Haloanilinium Ions in a Linear Quadrupole Ion Trap Mass Spectrometer", *Journal of The American Society for Mass Spectrometry*, 2013, **24**, 932–940.

(24) C. S. Hansen, B. B. Kirk, S. J. Blanksby and A. J. Trevitt, "Ultraviolet Photodissociation of the N-Methylpyridinium Ion: Action Spectroscopy and Product Characterization", *The Journal of Physical Chemistry A*, 2013, **117**, 10839–10846.

(25) C. S. Hansen, S. J. Blanksby, N. Chalyavi, E. J. Bieske, J. R. Reimers and A. J. Trevitt, "Ultraviolet photodissociation action spectroscopy of the N-pyridinium cation", *The Journal of Chemical Physics*, 2015, **142**, 014301.

(26) C. S. Hansen, S. J. Blanksby and A. J. Trevitt, "Ultraviolet photodissociation action spectroscopy of gas-phase protonated quinoline and isoquinoline cations", *Physical Chemistry Chemical Physics*, 2015, **17**, 25882–25890.

(27) D. L. Marshall, C. S. Hansen, A. J. Trevitt, H. B. Oh and S. J. Blanksby, "Photodissociation of TEMPO-modified peptides: new approaches to radical-directed dissociation of biomolecules", *Physical Chemistry Chemical Physics*, 2014, **16**, 4871–4879.

(28) D. J. Robichaud, A. M. Scheer, C. Mukarakate, T. K. Ormond, G. T. Buckingham, G. B. Ellison and M. R. Nimlos, "Unimolecular thermal decomposition of dimethoxybenzenes", *The Journal of Chemical Physics*, 2014, **140**, 234302.

(29) A. M. Scheer, C. Mukarakate, D. J. Robichaud, M. R. Nimlos and G. B. Ellison, "Thermal Decomposition Mechanisms of the Methoxyphenols: Formation of Phenol, Cyclopentadienone, Vinylacetylene, and Acetylene", *The Journal of Physical Chemistry A*, 2011, **115**, 13381–13389.

(30) M. B. Prendergast, B. B. Kirk, J. D. Savee, D. L. Osborn, C. A. Taatjes, K.-S. Masters, S. J. Blanksby, G. da Silva and A. J. Trevitt, "Formation and stability of gas-phase o-benzoquinone from oxidation of ortho-hydroxyphenyl:

a combined neutral and distonic radical study", *Physical Chemistry Chemical Physics*, 2016, **18**, 4320–4332.

Chapter 6

Conclusions and future directions

Conclusions

This thesis described the development of new techniques to probe photoinitiated reactions in single free falling microdroplets. Piezoactuated drop-on-demand (DoD) generation was coupled to various pulsed laser and mass spectrometry systems to investigate chemical transformations in single microdroplets. Two broad outcomes result from this work. The first comprises the practicalities of DoD generation as a platform for studying fundamental chemistry and the second relates to promising results to study chemical transformation in microdroplets.

The analytical utility of DoD droplet generators was shown when significant effort was invested into characterisation of the DoD microdroplet generator and the stability of microdroplet generation. Droplet size control and reproducibility was investigated and determined that DoD droplet generators produce highly reproducible microdroplets (<1% size variation) for a range of common solvents with good control over droplet size. These findings demonstrate that DoD microdroplet generators are a suitable experimental platform for studying processes in liquid domains. DoD generator's utility as a liquid delivery platform for analytical measurements was also highlighted when studying photochemistry using the SDDMS. Investigations into the liquid-phase photochemistry of berberine showed that species within single microdroplets could be probed rapidly with highly efficient sample usage.

A new technique focused on the study of fundamental chemistry using optical detection methods to track radical chemistry, and the second based on the detection of photogenerated products using mass spectrometry. Radical chemistry was followed in single microdroplets using a precisely timed two laser setup and optical detection methods. These studies demonstrated microdroplets can be utilised as reaction vessels for monitoring chemical transformations, but highlighted the

importance of the detection method and the complexity of liquid-phase radical chemistry. The second technique, single droplet desorption mass spectrometry (SDDMS), probed the photoproducts of a well-studied SET between the berberine cation and methanol. This study demonstrated products from single liquid-phase photolysis events could be detected and provided unique photochemical insights not available to traditional liquid-phase photochemical techniques.

These studies have demonstrated that DoD droplet generators and single microdroplets are an excellent platform for studying short-timescale photochemical transformations.

Future Direction

The single free-falling microdroplet chemical kinetics technique is capable of measuring rapid chemical transformations, including photoinitiated radical chemistry. As the work here has shown, the profluorescent method provides a promising platform for these measurements as it is relatively easy to detect using laser induced fluorescence, but underlying complexities in the formation of the fluorescent product means that quantitive kinetic details are difficult to elucidate. The ideal profluorescent strategy would employ a suite of specific profluorescent molecules for a number of target radical species that form a fluorescent product in a single step reaction.

An alternative detection method that could be utilised is a fluorescent species that readily reacts with the target radical and results in a non-fluorescent product. By measuring the decay in fluorescence signal the rate of the radical reaction could be determined, as the detected decay would result directly from the first radical reaction step. Investigating the feasibility of this fluorescent strategy would be the next goal to broaden this techniques capabilities and is favourable as it allows the same optical methods to be used.

Single droplet desorption mass spectrometry has shown to be successful at probing the photochemistry of larger molecules. Following on from this success, the next developmental focus for this technique should focus on probing photoinitiated biological processes. This would incorporate biological molecules, like nucleobases and proteins, into droplets containing photoactivated intercalator species. A large number of fundamental photochemical and photobiological could be investigated using the single droplet mass spectroscopy technique.

Appendix A

A.1 Mie Theory

Throughout the experiments presented in Chapter 2, measured single droplet fluorescence spectra are interpreted using Mie theory to determine the microdroplet radius and refractive index terms. Historically, Lorenz originally formalised electromagnetic scattering theory for dielectric spheres in 1890 but was separately rediscovered by Mie in 1909. Despite this, Mie's name is traditionally associated with the theory. The theory comprises solutions to Maxwell's equation for electromagnetic radiation interacting with a dielectric sphere[1–6].

In this thesis, Mie theory is used to determine the size and refractive index of single droplets by comparing the experimentally measured wavelength positions of optical resonances, known as whispering gallery modes (WGMs), with theoretically predicted values within the scattering efficiency (Q_{sca}) spectrum[3, 4]. Mie theory defines the extinction efficiency(Q_{ext}) of a dielectric sphere as the extinction efficiency is the ratio between the extinction cross section, C_{ext}, and the geometrical area of a particle, G, such that[4]:

$$Q_{ext} = \frac{C_{ext}}{G} \tag{A.1}$$

This can be visualised, as shown in Figure A.1, as the projected extinction cross section compared to the geometric area of a spherical particle.

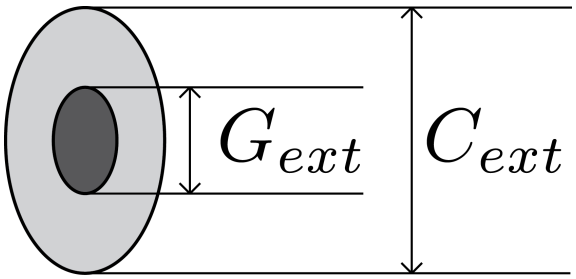

Figure A.1: Visualisation of the projected extinction cross section relative to the geometric area of a spherical particle.

The extinction efficiency is determined by two properties, the scattering efficiency, Q_{sca}, and the absorption efficiency, Q_{abs}. These are dimensionless terms that describe the ratio between their respective cross section, either scattering or absorption, and the geometrical area of a particle. These terms define the extinction efficiency, Q_{ext} such that[1–4, 6]:

$$Q_{ext} = Q_{sca} + Q_{abs} \tag{A.2}$$

Both of these properties depend on the sphere's radius and refractive index[1–4, 6]. The microdroplets studied throughout this thesis are generated from optically transparent liquids, therefore the Q_{abs} term is assumed to be negligible. The size parameter of the droplet, x, is a ratio of the spheres circumference and the wavelength of the scattered light, λ[1–4, 6]:

$$x = \frac{2\pi r}{\lambda} \tag{A.3}$$

For example, a sphere with a radius, r, of 25 μm and scattering wavelength of 500 nm corresponds to a size parameter of $\sim$314.

The scattering efficiency (Q_{sca}) is defined, for a given size parameter (x), by the following equation[3, 4]:

$$Q_{sca} = \frac{2}{x^2}\sum_{l=1}^{\infty}(2l+1)^2(a_l^2 + b_l^2)^2 \tag{A.4}$$

Where l is the mode number, and a_l and b_l are the scattering parameters of the sphere and are defined by[3, 4]:

$$a_l = \frac{\psi_l(x)\psi_l'(m_\lambda x) - m_\lambda\psi_l(m_\lambda x)\psi_l'(x)}{\zeta_l(x)\psi_l'(m_\lambda x) - m_\lambda\psi_l(m_\lambda x)\zeta_l'(x)} \tag{A.5}$$

$$b_l = \frac{m_\lambda\psi_l(x)\psi_l'(m_\lambda x) - \psi_l(m_\lambda x)\psi_l'(x)}{m_\lambda\zeta_l(x)\psi_l'(m_\lambda x) - \psi_l(m_\lambda x)\zeta_l'(x)} \tag{A.6}$$

Where m_λ describes the wavelength dependent refractive index of the droplet medium and $\psi(x)$ and $\zeta(x)$ are Ricatti-Bessel functions, with the primed functions referring the derivatives[3, 4]. Given by:

$$\psi_l(x) = \sqrt{\left(\frac{\pi x}{2}\right)}\cdot J_{l+\frac{1}{2}}(x) \tag{A.7}$$

$$\chi_l(x) = \sqrt{\left(\frac{\pi x}{2}\right)}\cdot N_{l+\frac{1}{2}}(x) \tag{A.8}$$

and

$$\zeta_l(x) = \psi_l(x) + i\chi_l(x) \tag{A.9}$$

Where J and N are Bessel and Neumann functions, respectively. The Ricatti-Bessel functions are used to solve the differential equations that arise throughout the calculation[3].

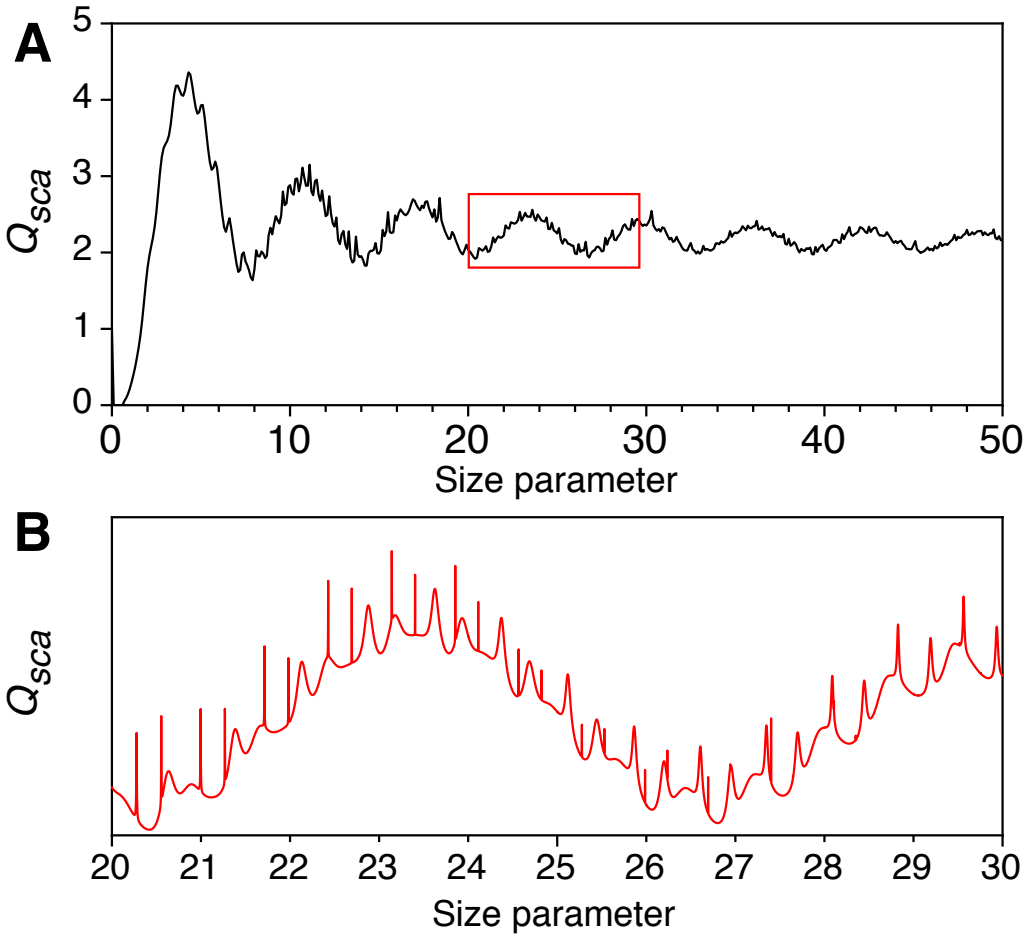

Figure A.2: (A) Calculated scattering efficiency, Q_{sca}, for a droplet with a refractive index of 1.5 over a range of size parameter values, x. Calculated with a resolution of 10^{-1}. (B) Zoom in showing the sharp peaks that arise from optical resonances (WGMs) and is calculated with a resolution of 10^{-3}.

Using these formulas, Q_{sca} can be calculated for a range of size parameters, as shown in Figure A.2 (A). The value of Q_{sca} follows a broad oscillating trend, but at $\gtrsim$10 sharp peaks are present as revealed in Figure A.2 (B). These sharp peaks occur at specific x values and occur when one of the scattering parameters, a_l or b_l, rapidly increases. Considering a sphere with a fixed radius, these sharp peaks occur at discrete wavelengths. When this occurs, scattered light matching these wavelengths form a standing wave, or resonance, greatly increasing the efficiency of scattered light[4, 6]. As this occurs at many wavelength values, this leads to sharp peaks,

known as whispering gallery modes (WGMs) or morphology dependent resonances (MDRs), modulating broad optical emission of single spheres, including Raman scattering and fluorescence. Experimentally measuring the location of WGMs allows the size and refractive index of the droplet to be ascertained using Mie theory[1–3, 6]. The fitting routine is described in Chapter 2.

A.2 References for Appendix A

(1) H. B. Lin, J. D. Eversole and A. J. Campillo, "Identification of morphology dependent resonances in stimulated Raman scattering from microdroplets", *Optics Communications*, 1990, **77**, 407–410.

(2) J. D. Eversole, H. B. Lin, A. L. Huston, A. J. Campillo, P. T. Leung, S. Y. Liu and K. Young, "High-Precision Identification of Morphology-Dependent Resonances in Optical Processes in Microdroplets", *Journal of the Optical Society of America B*, 1993, **10**, 1955–1968.

(3) J. R. Probert-Jones, "Resonance component of backscattering by large dielectric spheres", *Journal of the Optical Society of America A*, 1984, **1**, 822–830.

(4) C. F. Bohren and D. R. Huffman, in *Absorption and Scattering of Light by Small Particles*, Wiley-VCH Verlag GmbH, 2007, pp. 82–129.

(5) C. C. Lam, P. T. Leung and K. Young, "Explicit asymptotic formulas for the positions, widths, and strengths of resonances in Mie scattering", *Journal of the Optical Society of America B*, 1992, **9**, 1585–1592.

(6) R. Symes, R. M. Sayer and J. P. Reid, "Cavity enhanced droplet spectroscopy: Principles, perspectives and prospects", *Physical Chemistry Chemical Physics*, 2004, **6**, 474–487.

Appendix B

B.1 Article

Vaughn, B. S., Tracey, P. J. & Trevitt, A. J. (2016). Drop-on-demand microdroplet generation: a very stable platform for single-droplet experimentation. RSC Advances: an international journal to further the chemical sciences, 6 (65), 60215-60222.

B.2 Supplementary information

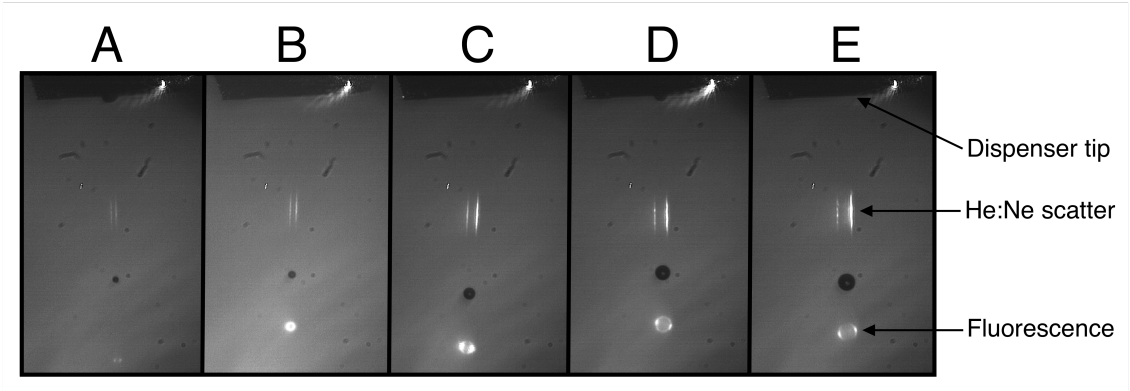

Figure B.1: Bright-field images of the droplet interaction region. Each frame shows the dispenser capillary tip, sync laser scattering, fluorescence emission and the resulting droplet from the corresponding waveforms in Figure 2.2.

Table B.1: Parameters of the waveforms shown in Figure 2.2.

Amplitude (V)	Waveform				
Section number	A	B	C	D	E
1	84	84	80	84	84
2	-42	-42	-	-42	-42
3	84	84	-	84	84
Pulsewidth (μs)	Waveform				
Section number	A	B	C	D	E
1	17	40	37.1	28	40
2	5	5	-	5	5
3	14	10	-	28	20
Total pulsewidth (μs)	36	55	37.1	61	65

Table B.2: Fitted parameters for each droplet shown in Figure 2.2.

Droplet	A	B	C	D	E
Imaged diameter (Pixels)	16	23	36	45	51
Radius (nm)	$10\,700 \pm 5$	$13\,420 \pm 14$	$21\,020 \pm 45$	$28\,100 \pm 150$	$31\,400 \pm 1\,400$
n_{A}	1.33 ± 0.01	1.39 ± 0.02	1.35 ± 0.03	1.30 ± 0.01	1.31 ± 0.6
n_{B} (nm^2)	$2\,465 \pm 23$	$-1\,033 \pm 27$	-637 ± 81	769 ± 83	355 ± 99
Refractive index* (575 nm)	1.34 ± 0.04	1.39 ± 0.05	1.35 ± 0.14	1.30 ± 0.14	1.31 ± 0.18

*refractive index $n(\lambda) = n_A + n_B/\lambda^2$

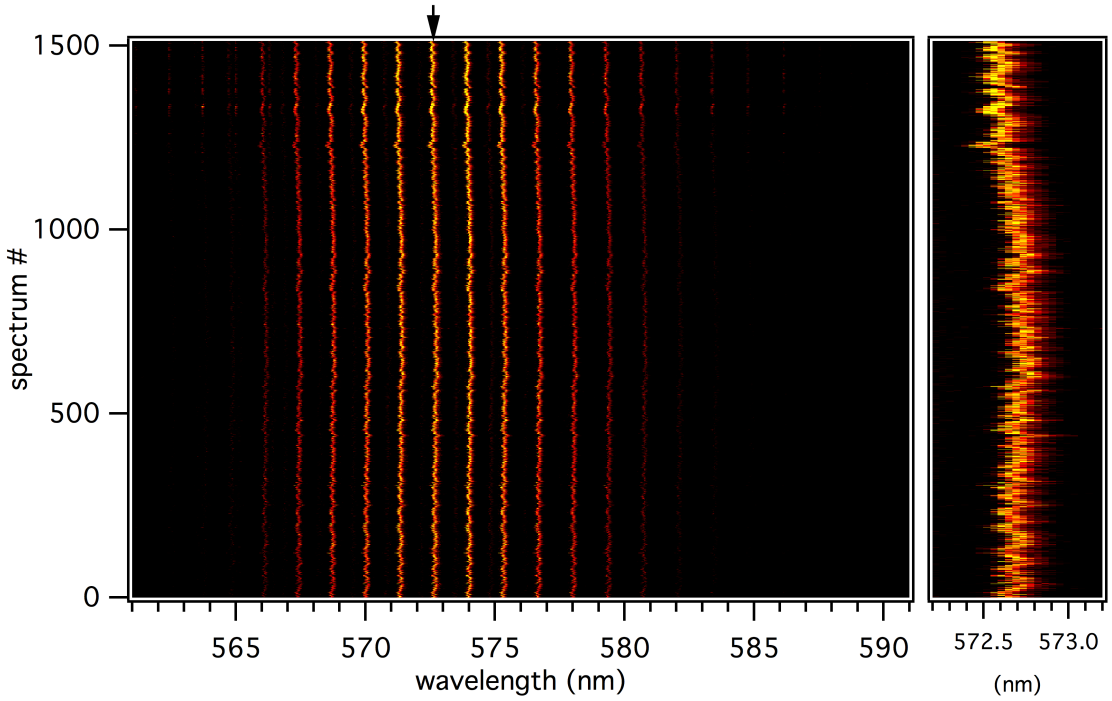

Figure B.2: 1500 consecutive single droplet fluorescence spectra stacked showing WGM positions over time. The dye-doped droplets were generated using the complex square wave pulse labeled E in Figure 2.2. The inset shows an expansion of the single WGM peak marked with an arrow.

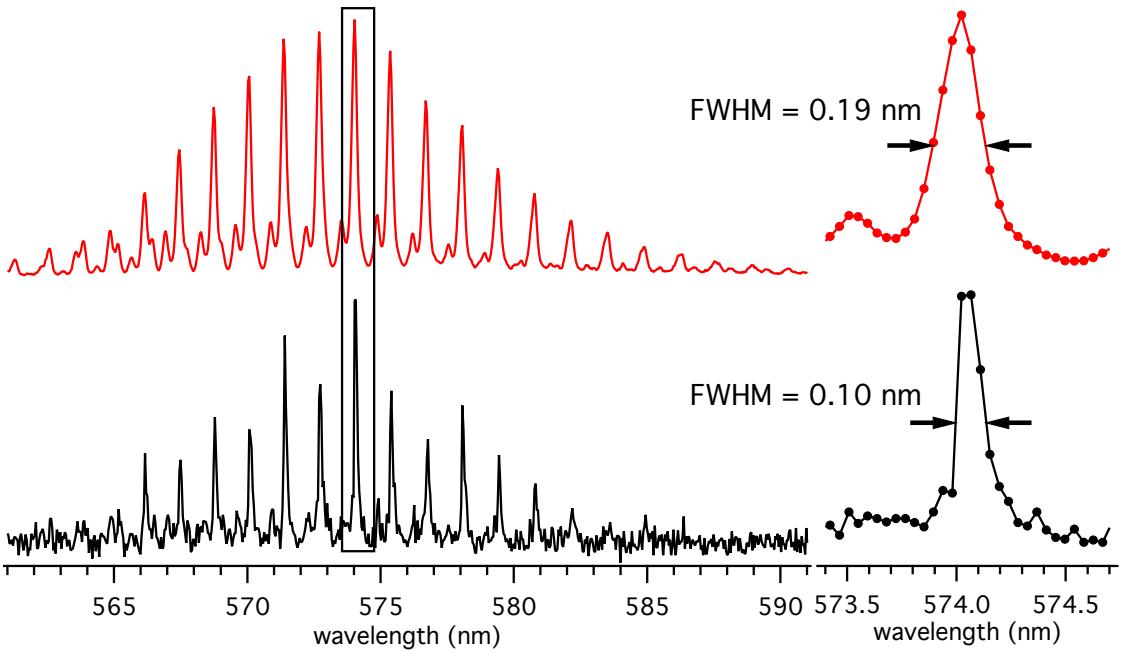

Figure B.3: Comparing a single droplet fluorescence spectrum (black) to an average of 1500 single droplet spectra (red) from Figure B.2.

Table B.3: Experimental and simulated MDR positions used in the fitting of droplet C. In red are predicted positions.

Experimental positions (nm)	Assignment	Simulated position (nm)	Difference (nm)
567.198	TE^5_{273}	567.177	0.021
568.269	TM^4_{278}	568.295	-0.026
569.082	TE^5_{272}	569.079	0.003
570.187	TM^4_{277}	570.191	-0.004
570.996	TE^5_{271}	570.994	0.002
572.106	TM^4_{276}	572.101	0.005
572.921	TE^5_{270}	572.922	-0.001
574.031	TM^4_{275}	574.023	0.008
574.858	TE^5_{269}	574.863	-0.005
576.812	TE^5_{268}	576.817	-0.005
578.787	TE^5_{267}	578.785	0.002
580.812	TE^5_{266}	580.767	0.045
582.851	TE^5_{265}	582.763	0.088
584.887	TE^5_{264}	584.772	0.115
-	TE^5_{274}	565.288	-
-	TM^4_{279}	566.411	-
-	TM^4_{274}	575.958	-
-	TE^4_{280}	565.621	-
-	TE^4_{279}	567.499	-
-	TE^4_{278}	569.390	-
-	TE^4_{277}	571.293	-
-	TE^4_{276}	573.209	-
-	TE^4_{275}	575.139	-
-	TE^4_{274}	577.081	-
-	TE^4_{273}	579.037	-
-	TE^4_{272}	581.006	-
-	TE^4_{271}	582.988	-
-	TE^4_{270}	584.985	-

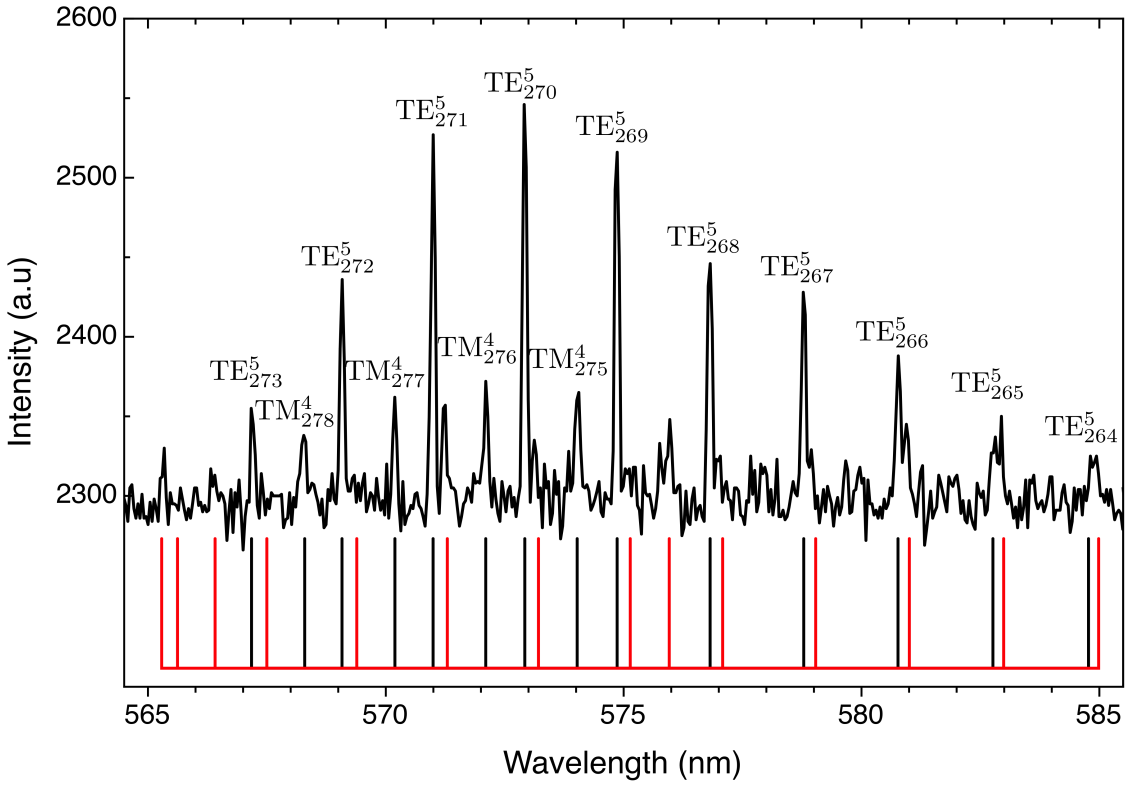

Figure B.4: Single droplet emission spectrum using waveform C with WGM assignments. Black bars represent the fitted WGMs data from Table B.3. The red bars are predicted WGMs (as listed in Table B.3)

Table B.4: Experimental and simulated MDR positions used in the fitting of droplet A.

Experimental positions (nm)	Assignment	Simulated position (nm)	Difference (nm)
563.880	TE^3_{137}	563.859	0.021
565.639	TM^3_{136}	565.625	0.014
567.571	TE^3_{136}	567.567	0.004
569.359	TM^3_{135}	569.362	-0.003
571.326	TE^3_{135}	571.326	0.000
573.151	TM^3_{134}	573.151	0.000
575.134	TE^3_{134}	575.137	-0.003
578.992	TE^3_{133}	579.001	-0.009
582.922	TE^3_{132}	582.919	0.003
586.917	TE^3_{131}	586.893	0.024
590.738	TE^2_{136}	590.763	-0.025
590.986	TE^3_{130}	590.923	0.063
594.797	TE^2_{135}	594.789	0.008
598.887	TE^2_{134}	598.871	0.016
-	TE^2_{137}	586.794	-

Table B.5: Experimental and simulated MDR positions used in the fitting of droplet B.

Experimental positions (nm)	Assignment	Simulated position (nm)	Difference (nm)
566.761	TE^5_{170}	566.744	0.017
569.716	TE^5_{169}	569.706	0.010
570.642	TE^4_{174}	570.644	-0.002
571.99	TM^4_{173}	571.944	0.046
572.702	TE^5_{168}	572.700	0.002
574.958	TM^4_{172}	574.934	0.024
575.726	TE^5_{167}	575.726	0
576.544	TE^4_{172}	576.624	-0.080
577.939	TM^4_{171}	577.957	-0.018
578.779	TE^5_{166}	578.784	-0.005
581.018	TM^4_{170}	581.011	0.007
581.868	TE^5_{165}	581.876	-0.008
585.001	TE^5_{164}	585.002	-0.001
587.224	TM^4_{168}	587.220	0.004
588.172	TE^5_{163}	588.162	0.010
590.368	TM^4_{167}	590.375	-0.007
591.374	TE^5_{162}	591.357	0.017
593.568	TM^4_{166}	593.564	0.004

Table B.6: Experimental and simulated MDR positions used in the fitting of droplet D.

Experimental positions (nm)	Assignment	Simulated positions (nm)	Difference (nm)
568.006	TE^5_{359}	568.001	0.005
568.249	TM^4_{365}	568.248	0.001
569.458	TE^5_{358}	569.461	-0.003
569.699	TM^4_{364}	569.702	-0.003
570.927	TE^5_{357}	570.929	-0.002
572.407	TE^5_{356}	572.405	0.002
573.89	TE^5_{355}	573.889	0.001
575.378	TE^5_{354}	575.380	-0.002
576.878	TE^5_{353}	576.879	-0.001
578.389	TE^5_{352}	578.387	0.002
579.899	TE^5_{351}	579.902	-0.003
581.428	TE^5_{350}	581.426	0.002

Table B.7: Experimental and simulated MDR positions used in the fitting of droplet E.

Experimental Positions (nm)	Assignment	Simulated positions (nm)	Difference (nm)
565.046	TE^4_{416}	565.024	0.022
566.326	TE^4_{415}	566.302	0.024
567.581	TE^4_{414}	567.587	-0.006
568.88	TE^4_{413}	568.877	0.003
569.683	TE^3_{420}	569.721	-0.038
570.171	TE^4_{412}	570.173	-0.002
571.472	TE^4_{411}	571.475	-0.003
572.308	TE^3_{418}	572.312	-0.004
572.779	TE^4_{410}	572.783	-0.004
573.618	TE^3_{417}	573.616	0.002
574.095	TE^4_{409}	574.097	-0.002
574.947	TE^3_{416}	574.926	0.021
575.424	TE^4_{408}	575.418	0.006
576.748	TE^4_{407}	576.744	0.004
577.58	TE^3_{414}	577.565	0.015
578.074	TE^4_{406}	578.077	-0.003
579.413	TE^4_{405}	579.416	-0.003
580.764	TE^4_{404}	580.761	0.003
582.124	TE^4_{403}	582.113	0.011
583.486	TE^4_{402}	583.471	0.015
584.862	TE^4_{401}	584.835	0.027

Appendix C

Vaughn, B. S., Tracey, P. J. & Trevitt, A. J. (2012). Laser-initiated iodine radical chemistry in single microdroplets. Chemical Physics Letters, 551 134-138.